Review

Recent Development in Nanoconfined Hydrides for Energy Storage

Cezar Comanescu [1,2,3] (ORCID)

1 National Institute of Materials Physics, Atomistilor 405A, 077125 Magurele, Romania; cezar.comanescu@infim.ro
2 Department of Inorganic Chemistry, Physical Chemistry and Electrochemistry, Faculty of Chemical Engineering and Biotechnologies, University Politehnica of Bucharest, 1 Polizu St., 011061 Bucharest, Romania
3 Faculty of Physics, University of Bucharest, Atomiștilor 405, 077125 Magurele, Romania

Abstract: Hydrogen is the ultimate vector for a carbon-free, sustainable green-energy. While being the most promising candidate to serve this purpose, hydrogen inherits a series of characteristics making it particularly difficult to handle, store, transport and use in a safe manner. The researchers' attention has thus shifted to storing hydrogen in its more manageable forms: the light metal hydrides and related derivatives (ammonia-borane, tetrahydridoborates/borohydrides, tetrahydridoaluminates/alanates or reactive hydride composites). Even then, the thermodynamic and kinetic behavior faces either too high energy barriers or sluggish kinetics (or both), and an efficient tool to overcome these issues is through nanoconfinement. Nanoconfined energy storage materials are the current state-of-the-art approach regarding hydrogen storage field, and the current review aims to summarize the most recent progress in this intriguing field. The latest reviews concerning H_2 production and storage are discussed, and the shift from bulk to nanomaterials is described in the context of physical and chemical aspects of nanoconfinement effects in the obtained nanocomposites. The types of hosts used for hydrogen materials are divided in classes of substances, the mean of hydride inclusion in said hosts and the classes of hydrogen storage materials are presented with their most recent trends and future prospects.

1. Introduction

The 21st century has been marked by tremendously important technological break-throughs, yet the massive expansion of industrialization has led to a deepening scarcity and skyrocketing prices of fossil fuels and energy raw materials, concomitant with a continual atmospheric pollution [1]. In the context of ever-increasing energy demands and the serious downsides of using fossil fuels, hydrogen has emerged over the past decades as a true and relevant promise of a carbon-free, green energy source for the world. However, hydrogen has a very low boiling point (20.4 K) at 1 atm, which severely restricts its use in the native form, except in some high pressure, cryogenic tanks that pose themselves additional energetic costs and safety risks regarding charging, transport and storing [1]. To circumvent the downfalls of using molecular dihydrogen (H_2), scientists have turned their attention and research focus on hydrogen-containing compounds, in the form of metal hydrides and related materials, which in turn feature higher thermal stability, safer handling, no fuel loss upon storage and overall produce the cleanest energy known today. The fuel of the future should ideally produce no carbon-containing by-products, exhibiting time- and property-related endurance over 1500 dehydrogenation-rehydrogenation cycles, and most importantly, all of this while featuring a gravimetric weight percentage of at least 5.5 wt.% (DOE's target set for 2025) [1–6]. The use of fossil fuels will eventually be phased-out and an

energy-friendly alternative with no carbon emissions must be brought forward. Hydrogen can generate roughly three times more energy than gasoline (33.3 vs. 11.1 kWh/kg), and can be produced by thermochemical, electrolytic, solar splitting of water or by means of biological reactions involving bacteria and algae microorganisms [1]. The near-future (2025) targets for hydrogen storage systems require a system gravimetric capacity of 5.5 wt.%, volumetric capacity 0.04 kg H_2/L, a hydrogen delivery temperature range of $-40 \ldots +85\,°C$, a delivery pressure of five bar, a very fast refill time (3–5 min) and a high purity hydrogen production of 99.97% [4–6]. Broadly speaking, the hydrogen storage methods are divided in physisorption-based (fast kinetics, storage capacity dependent on support surface area and pore volume, weak Van der Waals interatomic forces) and chemisorption-based (somewhat slower kinetics of desorption/absorption, storage depends on chemical composition of the material, strong chemical bonds) [7,8]. The chemisorption method is the preferred one of the two, as it binds hydrogen through chemical bonds rather than weaker interatomic forces therefore ensuring a reliable hydrogen storage capacity and comprise of metal hydrides, tetrahydridoborates, tetrahydridoaluminates and metal amides.

The topic of hydrogen storage materials has been recently reviewed by a series of articles. Lai et al., have summed up the characteristics of potential hydrogen storage materials and established guidelines that new storage materials should obey for viable applicability in storage tanks [9]. An overview of hydrogen economy and appropriate recommendations was discussed by Abe et al. [10]. The state-of-the-art of boron-nitrogen compounds for energy storage was reviewed by Kumar et al. [11] and Hagemann [12]. The solid-state materials used for hydrogen storage have been addressed by Lee et al. [13], Hadjixenophontos et al. [14], Broom and Hirscher [15], Comanescu [16], Kharbachi et al. [17], Zheng et al. [18] and He et al. [19], among others. The role of highly dispersed catalysts on hydrogen storage materials [20] and the topologically engineered materials serving for energy conversion and storage [21] have also been very recently reviewed, while the critical issue of accurately describing hydrogen sorption properties of materials has been highlighted by Broom et al. [15].

Among hydrogen storage materials, metal hydrides have gained increased popularity [5–8,22–26] and channeled many research groups to corroborate hydrogen sorption data to formulate general design principles for these materials [27,28], or to tackle the imminent need to expand current knowledge to production of large-scale hydrogen storage facilities [29]. While many advances have been made in the field of metal hydrides for hydrogen storage applications, the high thermal stability, sluggish kinetics and poor reversibility of hydrogen release/uptake have shifted researchers' attention towards nanoconfined hydrides that seem to alleviate some of these drawbacks, affording reversible, high gravimetric and volumetric hydrogen content at moderate temperatures [8,24,25].

The current review aims to tackle the current trend of employing nanoconfinements as a reliable tool to tune kinetic and thermodynamic behavior of hydride materials used for energy storage applications, and covers roughly the past five years.

2. Characterization Methods: Old, New, and Their Pitfalls

Traditionally, hydrogen storage materials follow a typical characterization protocol involving structural (XRD), elemental (XPS), morphological (SEM, TEM, N_2 sorption isotherms) and recording of hydrogenation data (PCI curves) [8]. Recently, a fundamental issue regarding elucidation of local environment of hydrogen in energy materials has revealed fast sample spinning ^{1}H NMR high-resolution spectroscopy as an appropriate tool to quantitatively characterize hydrogenated TiZrNi quasicrystals [30]. Kweon et al., showed by employing fast-spinning NMR spectroscopy that neutral hydrogen is surrounded by metal atoms shifting gradually from Zr to Ti and then Ni with increasing hydrogen content [30]. [1]H magic-angle spinning (MAS) NMR spectra has shown real promise for tuning electronic characteristics in a Ba-Ti oxyhydride, and could become a tool to investigate hydrogen occupation in the vicinity of the nuclei (negative Knight shift, indicative of interaction of conduction band electrons and probe nucleus) [31]. A potential downside

of using this technique is the high sensitivity to sample temperature, which was shown to increase due to fast rotor spinning (10–35 Hz), with a direct effect on main peak width change. Thus, additional precautions need to be undertaken to account for the effect of sample temperature increase when using fast spinning NMR spectroscopy [31].

Correct understanding of interfacial phenomena occurring during hydrogen storage is now termed as hydrogen spillover effect (HSPE). First discovered in 1964, it describes the migration of hydrogen atoms produced by H_2 decomposition on an active site, and it allows for a more insightful view on the dynamic behavior of hydrogen in energy storage materials [7]. While molecular orbital energy computations showed unfavorable energy for H atom spillover on non-reducible supports, recent studies have shown that HSPE is indeed possible on inert supports such as siloxanic materials (SiO_2) [7]. This bears a direct effect on hydrogen storage materials such as metal hydrides confined in mesoporous silica supports, where the spillover distance is limited to very short distances of ~10 nm [7].

Interestingly, developing tools to characterize metal hydrides during hydrogenation cycles has led to a summary of soft (X-ray absorption, XAS; X-ray emission spectroscopy, XES; resonant inelastic soft X-ray scattering, RIXS, X-ray photoelectron spectroscopy, XPS) and hard (X-ray diffraction, XRD) X-ray techniques used to this end (Figure 1) [32]. Soft X-rat techniques (100–5000 eV) are particularly appealing for tracking mechanistic behavior and intermediate product formation during hydrogenation studies, with direct influence over hydrogen storage capacity. XAS measurements for instance are bulk or surface-sensitive, and show 3d transition metal (TM) L-edges corresponding to transition of a 2p electron to an unoccupied 3d orbital, hence enabling monitoring of oxidation state changes during hydrogen release (+n...0) and uptake (0 ... +n) [32]. Similarly, TM-catalyzed alanates (2 mol%-catalyzed $NaAlH_4$) showed in XAS measurements the Al and Na K-edge and Ti L-edge consistent with a Ti-like state throughout the hydrogen release/uptake cycles, but with clear differences in Al state, which may undergo various intermediate states ($Al/NaAlH_4/Na_3AlH_6$) [32]. Quasi-elastic neutron scattering (QENS) studies have been undertaken to establish hydrogen dynamics in nanoscale sodium alanate $NaAlH_4$ and showed that fitting QENS to a Lorentzian function can yield two dynamic states of hydrogen and concluded that even at 77 °C there is a high percentage (18%) of mobile hydrogen atoms in the nano-$NaAlH_4$ [33].
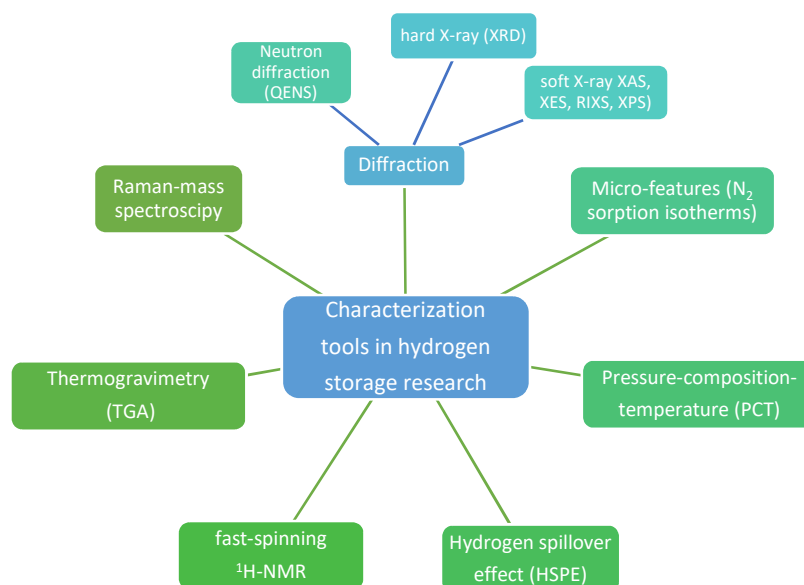

Figure 1. Main investigation methods used for characterization of hydrogen storage materials.

As an alternative method to the conventional pressure-composition-temperature (PCT) method typically used to characterize thermodynamic parameters for hydride-based sys-

tems, a less complex investigation method has been described for MgH$_2$-based materials: thermogravimetric analysis (TGA) [34]. This method relies on cycling the hydride under a flowing gas of constant hydrogen partial pressure, and the TGA curves are further analyzed using the van't Hoff equation to obtain the absorption/desorption enthalpies, which in the case of VTiCr-catalyzed Mg/MgH$_2$ materials, showed good agreement with traditional PCT results [34]. Other recent research established a nano-Pd patched surface of Pd$_{80}$Co$_{20}$ to afford one of the most sensitive optical hydrogen sensors (fast response of <3 s, high accuracy of <5%, and very low limit of detection of 2.5 ppm) [35]. Employing interpretable machine learning could also help formulate general design principles for intermetallic hydride-based systems being used to validate limited data from the HydPARK experimental metal hydride database and stressing the recommendation for experimental groups to report ΔH, ΔS, P_{eq}, T and V_{cell} [27].

Valero-Pedraza et al., have characterized the hydrogen release form ammonia borane nanoconfined in mesoporous silica by means of Raman-mass spectroscopy, which confirmed hydrogen release from AB at lower temperatures, fewer BNHx gaseous fragments in nanoconfined samples and a lack of polyiminoborane formation during thermolysis [36]. The study also pointed out to silica-hydride interactions, which were identifiable based on modifications in the Raman spectra [36].

However, analysis of the literature data also points out to several weaknesses in applying traditional characterization methods that have not yet been tuned for current nanosized materials [15,34,37,38]. For instance, AB (ammonia borane) hydrogenation studies showed many inconsistencies [38]. By assessing TGA data in the literature, Petit and Demirci urge caution when evaluating ammonia borane weight loss (and consequently hydrogen release), as this was found to be highly dependent on the operation conditions (semi-closed/open reactor) and were shown to erroneously indicate a different hydrogen release temperature onset and hydrogen wt.% [38].

Surrey et al., conducted a critical review of a paper discussing electron microscopy observation of elementary steps in MgH$_2$ release mechanisms [37]. In this work, they debunked the general assumption that TEM microscopy can be used, as such, without further testing methodology adjustment in the case of hydrogen storage materials such as MgH$_2$. The issue was serious, as it led initial authors to misinterpret TEM observations, by disregarding the key aspect of electron beam induced dehydrogenation of MgH$_2$ [37]. In a cascade chain of errors, the beam-induced heat producing dehydrogenation also led to a false interpretation of SAD (selected area diffraction) data, which only showed hollow MgO shells deprived of Mg-core, an effect actually ascribed to the nanoscale Kirkendall effect. As a result, it was apparent that the sample actually measured did not even contain MgH$_2$ any longer [37].

In line with the issues raised above, Broom and Hirscher discussed the necessary steps for reproducible results in hydrogen storage research [15].

3. Bulk vs. Nanomaterials

After its first inclusion on the research outlook of scientists worldwide in 1996, nano-sized hydrides have known a wide expansion, mainly due to several important kinetic and thermodynamic improvements of nanoconfinement over their bulk counterparts [4,8,14,16,18,21–23,27,28,39–64]. Over time, nanoconfinement has emerged as a reliable tool for tuning not only thermodynamic and kinetic behavior at nanoscale, but also for altering reaction pathways, lowering or even suppressing side-reactions and side-products, while also affording better size control of the particles over several hydrogen release/uptake cycles (Figure 2).
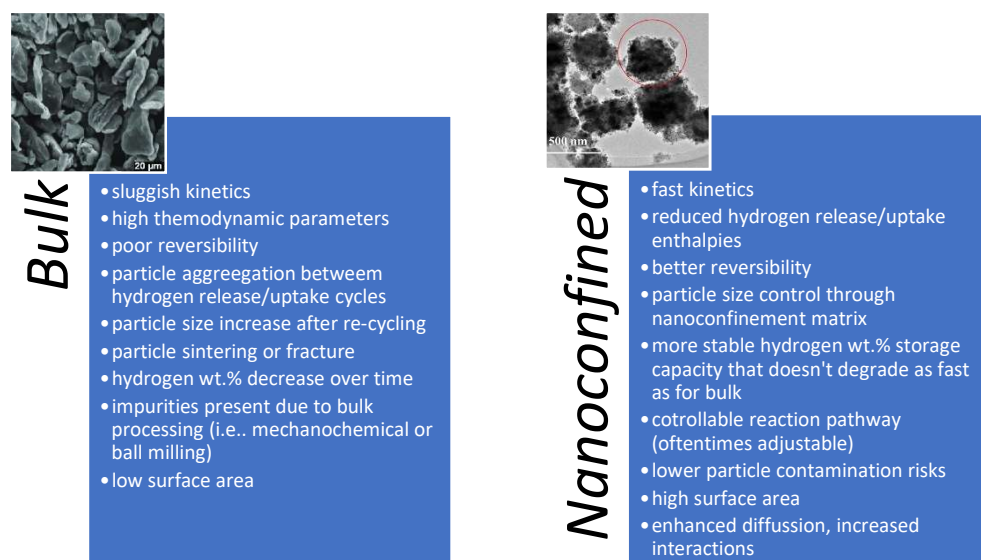
Bulk
- sluggish kinetics
- high themodynamic parameters
- poor reversibility
- particle aggreegation betweem hydrogen release/uptake cycles
- particle size increase after re-cycling
- particle sintering or fracture
- hydrogen wt.% decrease over time
- impurities present due to bulk processing (i.e.. mechanochemical or ball milling)
- low surface area

Nanoconfined
- fast kinetics
- reduced hydrogen release/uptake enthalpies
- better reversibility
- particle size control through nanoconfinement matrix
- more stable hydrogen wt.% storage capacity that doesn't degrade as fast as for bulk
- cotrollable reaction pathway (oftentimes adjustable)
- lower particle contamination risks
- high surface area
- enhanced diffussion, increased interactions

Figure 2. Main features of bulk and nanoconfined materials for hydrogen storage; exemplified for the case of an overly-studied hydride, MgH_2. (inset reprinted/adapted with permission from Ref. [65]. 2022, Elsevier).

3.1. Physical and Chemical Aspects of Nanoconfinement Effects

Nanoconfinement of active hydride species inside a porous host bears a number of physical and chemical implications [1,7,8,22,25,27,41,52–56,59–62,66–86].

3.2. Nanocomposites

The proper term for describing the materials resulting from the nanoconfinement of active hydride source into a nanoporous matrix is nanocomposite [4,41,52,54,60,66,68–70,77,78].

4. Types of Hosts Used as Hydride Matrix

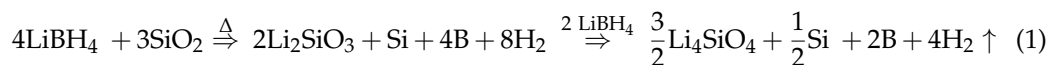### 4.1. Siloxanic Materials (MCM-41, SBA-15, SBA-48, etc.)

Although some complex hydride materials (e.g., complex metal borohydrides) are plagued by an undesirable reaction with the porous host above the hydride melting temperature with formation of silicates [16], mesoporous silica is still used in several studies concerning nanoconfinement effects in hydrogen storage materials [74,87–90] (Table 1).

Table 1. Recent progress in silica-based supports for nanoconfined hydrogen storage.
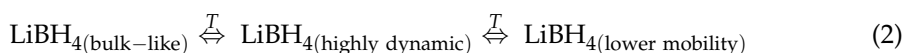
Silica Type	Hydrogen Storage Material	Nanoconfinement Method	Ref.
MSU-H	$LiBH_4$	solvent infiltration	[16]
MCM-41	$NaBH_4$	melt impregnation	[74]
MCM-41, SBA-15	$LiBH_4$	melt impregnation	[87]
poly(acryalamide)-grafted mesoporous silica nanoparticles (PAM-MSN)	NH_3BH_3 (AB)	melt impregnation	[88]
SBA-15	$Li_2(BH_4)(NH_2)$.	melt impregnation	[89]
silica aerogel	NH_3BH_3 (AB)	aerogel drying and AB gas antisolvent precipitation	[90]
MCM-41, SBA-15	$LiBH_4$-$LiNH_2$	melt infiltration	[91]

When $LiBH_4$ was used as borohydride source in a mesoporous silica host, the reaction occurring during borohydride melting is a two-step process yielding lithium metasilicate, Li_2SiO_3, and ultimately lithium orthosilicate, Li_4SiO_4 (Equation (1)) [16]. This reaction is a

downside of using nanoporous siloxanic supports for borohydride nanoconfinement, as it consumes the hydride material in an irreversible side-reaction (Equation (1)).

$$4LiBH_4 + 3SiO_2 \overset{\Delta}{\Rightarrow} 2Li_2SiO_3 + Si + 4B + 8H_2 \overset{2\ LiBH_4}{\Rightarrow} \frac{3}{2}Li_4SiO_4 + \frac{1}{2}Si + 2B + 4H_2 \uparrow \quad (1)$$

Confining LiBH$_4$ by a melt impregnation technique in nanoporous silica MCM-41 (1D, d_{pore} < 2 nm) or SBA-15 (2D-ordered pore structure, d_{pore} = 5, 7 and 8 nm) of different pore sizes reveals an interesting interfacial effect governing Li$^+$ and BH$_4^-$ ion mobility [87]. Using solid-state NMR (^{1}H, ^{6}Li, ^{7}Li and ^{11}B), Lambregts et al., showed that, as a result of nanoconfinement, two distinct fractions of LiBH$_4$ coexist and this is a temperature-dependent equilibrium (Equation (2)):

$$LiBH_{4(bulk-like)} \overset{T}{\Leftrightarrow} LiBH_{4(highly\ dynamic)} \overset{T}{\Leftrightarrow} LiBH_{4(lower\ mobility)} \quad (2)$$

The high mobility LiBH$_4$ is located near silica pore walls, whereas LiBH$_4$ of lower mobility is located towards the pore's core; the theoretical wall thickness was estimated based on a core-shell model LiBH$_4$@SBA-15, as $t = r_p(1 - \sqrt{f_{lower\ mobility}}$. The dynamic layer thickness is temperature-dependent, and increases from 0.5 nm (30 °C) to 1.2 nm (110 °C). Here again the results of calorimetric data were found to overestimate the highly-mobile LiBH$_4$ layer thickness (1.9 nm), pointing out the need for care when deriving the same parameter from different techniques [87]. While ^{6,7}Li NMR spectra was too complex for unequivocal deconvolution, ^{1}H and ^{11}B NMR spectra clearly show two components throughout the investigated temperature range (30–130 °C), consistent with the two LiBH$_4$ fractions of different ion mobility [87].

Melt impregnation of NaBH$_4$ in MCM-41 at 560 °C led to a drastic surface area decrease from 1110.9 m^2 g^{-1} (pristine MCM-41) to 3.5 m^2 g^{-1} (nanocomposite NaBH$_4$@MCM-41), and to a 78% pore filling attested by pore volume decrease (1.02 cm^3 g^{-1} to 0.02 cm^3 g^{-1}) [74]. Interestingly, some amount of sodium perborate NaBO$_4$ resulting from unavoidable oxidation of the borohydride with silanol (Si-OH) groups is the main additional phase detected by XRD, confirming no significant additional phases due to melt impregnation at >500 °C. The dehydrogenation onset peak for NaBH$_4$ was reduced by nanoconfinement from 550 °C (bulk) to 520 °C (nanocomposite) [74]. Due to the insulating nature of boron oxide phase (NaBO$_4$), the ionic conductivity did not improve the same way it does for LiBH$_4$, and remained largely the same (7.4 × 10^{-10} S cm^{-1}). This 10-fold increase in ionic conductivity that only lasts up to 70 °C for the nanocomposite is attributed to the presence of larger dodecaborate ions B$_{12}$H$_{12}^{2-}$ whose distinct presence was signaled in ^{11}B NMR spectra by an additional sharp peak at −15.58 ppm (NaBH$_4$@MCM-41) vs. −41.95 ppm (for pristine BH$_4^-$) (Figure 3) [74].
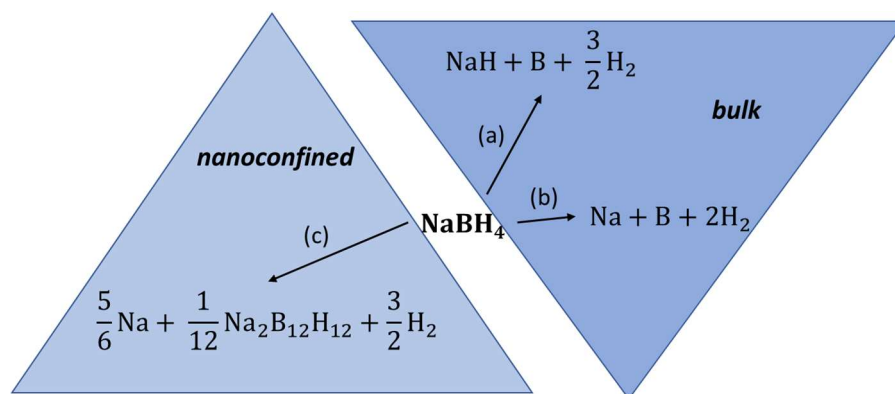

Figure 3. Possible decomposition pathways for bulk NaBH$_4$ (a,b) and for melt-impregnated, nanoconfined NaBH$_4$ (c).

The organic–inorganic hybrid poly(acryalamide)-grafted mesoporous silica nanoparticles (PAM-MSN) have been evaluated as functionalized nanoporous hosts for tuning hydrogen release/uptake behavior in ammonia borane (AB), which started to desorb hydrogen in the said nanocomposite at a lower temperature with respect to pristine AB, which was further enhanced by functionalization of the mesoporous silica shell with carboxylic -COOH groups [88].

2D-ordered mesoporous silica of cylindrical pores (SBA-15) was successfully used by Yang et al., for enhancing the ionic conductivity of a mixed-anion borohydride, $Li_2(BH_4)(NH_2)$. By following a melt infiltration procedure, the Li-ion conductivity was increased in $Li_2(BH_4)(NH_2)$@SBA-15 to 5×10^{-3} S cm^{-1} at 55 °C [89]. A marked kinetic improvement of hydrogen release ($\Delta T = 70$ °C) was recently reported by Rueda et al., by confinement of ammonia borane (AB) in silica aerogel by simultaneous aerogel drying and AB gas antisolvent precipitation using compressed CO_2, and achieving a weight AB loading of up to 60 wt.% [90].

4.2. Carbonaceous Materials (C-Replica of Mesoporous Silica, C-NTs, C-Foam, C-Spheres, Graphene, Graphene Oxide GO, Reduced Graphene Oxide r-GO)

Given the chemically-sensitive interaction between silanol (Si-OH) and borohydride (BH_4^-) groups and the subsequent oxidation reaction, the election of mesoporous silica as a host for loading borohydride materials seems less feasible. Therefore, many research studies have shifted their focus towards carbon-based materials, which do not exhibit such a drawback. Many forms of carbonaceous matrix have been employed: C-replica of mesoporous silica, C-NTs, C-foam, C-spheres, graphene, graphene oxide GO, reduced graphene oxide r-GO etc. (Table 2) [40,42,53,65,69,70,92–146].

Table 2. Recent progress in carbonaceous-based supports for nanoconfined hydrogen storage.

Carbon Type	Hydrogen Storage Material	Nanoconfinement Method	Ref.
MOFs incorporating activated carbon (AC) and aluminum doping	AlH_3	solution impregnation method	[40]
Hollow carbon spheres (HCNs)	$M(BH_4)_x$ (M = Li, Na, Mg, Ca)	solvent impregnation (best results, lower T_d), melt infiltration	[42]
Carbon aerogels with different porosities	Mg/MgH_2	direct solvent-based synthesis of MgH_2 from $MgBu_2$	[53]
Core-shell CoNi@C	MgH_2 obtained by hydriding combustion synthesis (HCS)	high energy ball milling under Ar atmosphere	[65]
Graphene	$NaAlH_4$	solvent infiltration (THF; bottom-up strategy (90% loading)	[69]
Porous hollow carbon nanospheres	$LiBH_4$-$Mg(BH_4)_2$ eutectic (LMBH)	melt-infiltration	[70]
xNi-CMK-3; N-CMK-3 (x = 1 and 5 wt.%)	MgH_2	in situ generated from $MgBu_2$ soln. in heptane	[92]
Double-Layered Carbon Nanobowl	$LiBH_4$	melt infiltration	[93]
Carbon shell (2–3 nm thick)	Mg/MgH_2	reactive gas evaporation	[94]
TiO_2-decorated amorphous carbon (AC)	MgH_2	ball milling	[95]
High Surface Area Graphite (HSAG)	$LiAlH_4$	solvent infiltration/incipient wetness method	[96]
Porous carbon, High Surface Area Graphite (HSAG-500)	Mg_2CoH_5	bottom-up approach (Co^{2+} salt reduction, $MgBu_2$ hydrogenation and solid-gas reaction $Co + 2MgH_2 + 0.5H_2$)	[97]

Table 2. *Cont.*

Carbon Type	Hydrogen Storage Material	Nanoconfinement Method	Ref.
Graphene	MgH_2	solvent-free, $MgBu_2$ thermal decomposition	[98]
Resorcinol-formaldehyde carbon aerogel (RFC)	$2LiBH_4$-$LiAlH_4$	two-step melt-infiltration	[99]
Activated charcoal (AC)	$LiBH_4$	melt-infiltration	[100]
$NiCo_2O_4$-anchored reduced graphene oxide ($NiCo_2O_4$@rGO)	$LiAlH_4$	low-temperature solution method coupled with annealing treatment; to yield $NiCo_2O_4$@rGO nanocomposites	[101]
Nickel@nitrogen-doped carbon spheres (Ni@NCS)	MgH_2	hydriding combustion and subsequent high-energy ball milling	[102]
Ultrathin, flexible Graphene (GR)	MgH_2	bottom-up self-assembly strategy (from $MgBu_2$ in C_6H_{12})	[103]
Porous Hollow Carbon Nanospheres (PHCNSs)	$LiBH_4$	mortar grounded, then melt infiltration (300 °C, 30 min, 100 bar H_2)	[104]
Electrochemically synthesized reduced graphene oxide (erGO)	Mg-B	ball milling	[105]
Fe_3O_4@C, Multifunctional porous scaffold of carbon wrapped ultrafine Fe_3O_4	$LiBH_4$	melting infiltration (300 °C, 30 min, 100 bar H_2)	[106]
Activated carbon nanofibers (ACNF) impregnated with TiO_2	$LiBH_4$	mortar grinding (1:1, wt.), melt infiltration (310 °C at 5 °C/min rate under 60 bar H_2, dwelling at 310 °C for 45 min, cooling to rt)	[108]
Carbon nanotube (CNT)	$xMgH_2$/AlH_3 (x = 1–4)	ball milling (200 rpm, 1 h, under H_2 atmosphere) for $xMgH_2$/AlH_3; ball milling in steel container (1 h, under H_2 atmosphere) for MgH_2/AlH_3@CNTs	[109]
Carbon nanoscaffolds (Graphite, CMK-3, Graphene, CNT)	MgH_2	solvent, melt infiltration	[110]
N-doped CMK-3 carbon (NCMK-3)	$LiAlH_4$	solution infiltration of $LiAlH_4$ freshly recrystallized from diethyl ether	[111]
N-doped graphene hydrogels (resorcinol-formaldehyde)	$LiBH_4$	ball milling (300 min, 400 rpm), melt impregnation (30 min, 300 °C, 60 bar H_2)	[112]
N-Doped Graphene-Rich Aerogels Decorated with Ni and Co Nanoparticles	$LiBH_4$	pre-mixing (mortar, pestle; 30 min), then melt impregnation (30 min, 300 °C, 60 bar H_2).	[113]
Graphene sheets (G)	LiH ($LiBH_4$, $LiNH_2BH_3$)	one-step solvothermal reaction of butyllithium supported by graphene in cyclohexane under a H_2 pressure of 50 atm.	[114]
Graphene Nanosheet (G)	MgH_2	solid-state reaction (metathesis $MgCl_2$, LiH), ball milling (30 h, 0.5 MPa H_2, 500 rpm)	[115]
Activated mesoporous carbon (MC-a)	$Ca(BH_4)_2$	incipient wetness method (0.1 M $Ca(BH_4)_2$.MTBE methyl tert-butyl ether, anhydrous)	[116]
Edge-Functionalized Graphene Nanoribbon (GNRs): unfunctionalized cGNR, nitrogen edge-doped N_2-cGNR and N_4-cGNR, and fluorenone GNR (f-cGNR)	Mg(/MgH_2)	Rieke-like reaction (up to 98% Mg wt.%)	[117]

Table 2. *Cont.*

Carbon Type	Hydrogen Storage Material	Nanoconfinement Method	Ref.
Ultrafine Ni nanoparticles dispersed on porous hollow carbon nanospheres (PHCNSs)	MgH_2 (Mg_2Ni/Mg_2NiH_4)	ball-milling (50 bar H_2, 24 h, planetary ball mill QM-3SP4, Nanjing, 500 rpm, ball-to-sample weight ratio of 120:1)	[118]
Hydrogenated graphene (HG)	N/A	Li-reduction in graphene(G), then CH_3OH hydrogenation	[119]
Graphene decorated with Ni nanocrystals	$LiBH_4$	solvothermal reaction (50 bar H_2 at 100 °C, 24 h, continuous stirring); ^nBuLi hydrogenation (to LiH) and $C_6H_{15}NBH_3$ reaction (to $LiBH_4$-$C_6H_{15}N$); Cp_2Ni (for Ni)	[120]
Defected graphene oxide (GO) or reduced graphene oxide (rGO)	Mg/MgH_2	in situ generation of Mg from a THF soln. of Cp_2Mg	[121]
Reduced graphene oxide (rGO)/Li foil	Mg/MgH_2	direct solvent-based synthesis of MgH_2 from $MgCp_2$	[122]
Carbon Matrix	$LiBH_4$	melt-impregnation	[123]
1D Carbon Matrix (Fishbone Shaped): CNF, GNF	Mg/MgH_2	direct solvent-based synthesis of MgH_2 from sonicated, solvent(THF)-impregnated $MgCp_2$-CNF/GNF	[124]
Nickel-Containing Porous Carbon Sheets (Ni-PCSs)	$LiAlH_4$, $NaAlH_4$, and $Mg(AlH_4)_2$	pre-mixing in mortar (15 min.), high energy ball-milling (SPEX M8000 mixer/mill, 15 min.) w/ball-to-powder weight ratio 40:1.	[125]
Reduced graphene oxide (rGO)	$Mg(BH_4)_2$	in situ generation of $rGO/Mg(BH_4)_2$: rGO slurry with 1 M $MgBu_2$ in heptane, added over $BH_3·S(CH_3)_2$.	[126]
MWCNT (w/TiO_2 2 mol% relative to $NaAlH_4$)	$NaAlH_4$	physical mixture; PEIS/MWCNT/$NaAlH_4$; polyaniline (Pani) or sulfonated polyetherimide (PEIS) as polymer matrices	[127]
Nitrogen-Doped Nanoporous Carbon Frameworks (N-doped NPC)	$NaAlH_4$	pre-mixing (mortar/pestle, 10 min), melt infiltration (Sievert apparatus, 190 bar H_2, 45 min, 200 °C)	[128]
Graphene oxide (GO) framework	$NaAlH_4$	incipient wetness impregnation	[129]
Activated carbon (AC)	$2LiBH_4$-MgH_2	milling $2LiBH_4$:Mg in stainless-steel vial planetary ball mill; 20:1 ball-to-powder weight ratio (BPR), 10 h milling time, 580 rpm	[130]
Ordered mesoporous carbon structures (CMK)	N/A (Ni NP)	Ni NPs inserting by wetting the CMK structures	[131]
ultrafine Ni nanoparticles in a mesoporous carbon matrix (MC-$N_{iinsitu}$)	$Mg(BH_4)_2$	$Mg(BH_4)_2$ (45 wt.%) solution (THF, Et2O) slowly impregnated into the MC variant	[132]
High surface area graphite (HSAG)	LiH	catalytic hydrogenation of lithium naphthalenide (for LiH), stirring at 400 rpm, 0.35 MPa H_2, 40 °C, aged overnight.	[133]
Fe-benzenetricarboxylate (Fe-BTC)	$NaAlH_4$	solution infiltration using tetrahydrofuran (THF)	[134]
Activated carbon nanofibers (ACNF)	$LiBH_4$-$LiAlH_4$	solution impregnation of $LiAlH_4$ (Et2O) then melt infiltration of $LiBH_4$ (310 °C, 110 bar H_2, 45 min.)	[135]
Carbon aerogel (CA) by resorcinol (R) and formaldehyde (F) process	N/A	triethylamine (as catalyst)	[136]
3-D activated carbon (M-3D C)	MgH_2	solvent-reduction (NH_2NH_2) of a slurry $MgBu_2$ (1 M, heptane) in M-3D C	[137]

Carbon Type	Hydrogen Storage Material	Nanoconfinement Method	Ref.
Reduced graphene oxide (rGO)/metal nanocrystal multilaminates	Mg/MgH$_2$	solution-based co-reduction method of MgCp$_2$/GO with lithium naphthalenide solution (2 h stirring, then 20 min centrifuged @10,000 rpm)	[138]
ZIF-67-Derived Co@Porous Carbon	NH$_3$BH$_3$ (AB, Ammonia Borane)	infiltration	[139]
Carbon nanotube arrays (CMK-5)	AlH$_3$ and NH$_3$BH$_3$	pre-mixed (mortar, hand-milling); solvent (THF) infiltration into CMK-5.	[140]
carbon nanomaterials MDC (based on calcined MOF-5)	NH$_3$BH$_3$	solvent infiltration	[141]
Ice templating sheets of graphene oxide (GO) or partially reduced graphene oxide (rGO)	NH$_3$BH$_3$	solvent infiltration (AB infiltrated to a solvent suspension of GO)	[142]
Bio-derived micro/mesoporous carbon with well-organized pores (TiO$_2$/B co-catalysts)	NH$_3$BH$_3$	solvent immersion (AB methanol solution into C-TiO$_2$(B)), then vaporization	[143]
Microporous carbon (ECMC, narrow PSD, obtained by CVD from ethylene-filled Zeolite EMC-2)	NH$_3$BH$_3$	solvent infiltration (of AB methanol solution to ECMC)	[144]
V$_2$O$_3$-supported cubic C-nanoboxes	MgH$_2$	ball milling (500 rpm, 24 h, BPR:120:1, 50 bar H$_2$).	[146]

4.3. Metal-Organic Frameworks (MOFs) and Functionalized-MOFs

Metal-organic frameworks (MOFs) have recently been utilized as hosts for metal hydrides, due to their tunable porosity, stability and enhancement of kinetic and thermodynamic properties of hydrogen storage materials (Table 3). Their functionalization with appropriate groups/molecules opens new doors in energy storage field, being able to bypass side-reactions, alter significantly the reaction pathway, and afford a better reversible material in hydrogen release/uptake studies [39,40,68,86,147–157].

Table 3. Recent progress in MOF-based nanoconfined hydrogen storage systems.

MOF Type	Hydrogen Storage Material	Nanoconfinement Method	Ref.
Cu-BDC(DMF) (BDC = benzenedicarboxylate; DMF-dimethylformamide, used as removal/capping solvent)	AB (NH$_3$BH$_3$)	hand grinding (5 min, under Ar); AB: Cu-BDC(DMF) weight ration: 1:20, based on pore filling estimation	[39]
MIL-101-NORIT-RB3 decorated (an activated carbon AC added in situ during synthesis of MOF)	AlH$_3$	solvent impregnation (THF, under Ar)	[40]
Various MOFs (of type MOF-5, MIL, UiO, ZIF, IRMOF etc.)	Pg/PdH$_2$	Various: Liquid impregnation, Metal-Organic Chemical Vapour Deposition; Sol-Gel; Double Solvent Method	[68]
HKUST-1, IRMOF-1, IRMOF-10, UiO-66, UiO-67, and MIL-53(Al), MIL-101, MOF-74(Mg)	AB (NH$_3$BH$_3$), NaAlH$_4$, MH$_x$ (M = Li, Na, Mg, Ca, Al)	solvent- and melt infiltration	[86]
Nb$_2$O$_5$@MOF (Zn-based MOF, ZIF-8 (Zn(2-methylimidazole)$_2$))	MgH$_2$	ball milling (400 rpm, 4 h, ball to powder ratio 40:1) yielding MgH$_2$@7 wt.% Nb$_2$O$_5$@MOF	[147]

MOF Type	Hydrogen Storage Material	Nanoconfinement Method	Ref.
MOF-5, MOF-177, HKUST-1, NOTT-100, Mg-IRMOF-74-I, NiIRMOF-74-I, Mg-IRMOF-74-II and Ni_2(mdobdc)	Mg/MgH_2; Ni/NiH_2	Hydrogen release/uptake in Ni-based MOFs	[148]
Ni-MOF scaffold (Ni_2(TMA), TMA-trimasic acid)	MgH_2	in-situ synthesis; infiltration of $MgBu_2$ (1 M in heptane) in Ni-MOF porosity, hydrogenation (453 K, 4.8 MPa H_2, 20 h) to yield MgH_2@Ni-MOF	[149]
UiO-66 ($Zr_6O_4(BDC)_6$, BDC = 1,4-benzenedicarboxylate)	$Ti(BH_4)_3$	gas adsorption of $Ti(BH_4)_3$ at dry-ice conditions (N_2-carrier gas) into UiO-66	[150]
UiO-67bpy ($Zr_6O_4(OH)_4(bpydc)_6$ with $bpydc^{2-}$ = 2,2′-bipyridine-5,5′-dicarboxylate)	$Mg(BH_4)_2$	solvent impregnation	[151]
Various (High-throughput molecular simulations)	N/A	theoretical study (machine learning)	[152]
IRMOF-1, IRMOF-10, UiO-66, UiO-67, and MIL-53(Al)	AB (NH_3BH_3)	solvent infiltration (CH_3OH)	[153]
MIL-53	AB (NH_3BH_3)	incipient wetness impregnation method (CH_3OH saturated solution)	[154]
MIL-101-NH_2 (Al)	Al/AlH_3	solvothermal treatment involving N,N-dimethylformamide (DMF) as solvent	[155]
MOF-5	M/MH_x	post-confinement, in-situ confinement, double-solvent method (better efficiency)	[156]
MOF = ZIF-8, ZIF-67, MOF-74	Mg/MgH_2	in situ reduction in Mg^{2+}-decorated MOFs by NpLi solution in THF	[157]

4.4. Main Group and TM (Transition Metal)-Oxides, Sulfides and Nitrides

Various metal oxides and nitrides of metals (main group and TM) have been employed as hosts for hydrogen storage materials [91,95,101,106,147,158–172]. Embedding active hydrogen-storage systems into inert nanoscaffolds has been used in the past, but reports on shells of the sulfide type are rare in the scientific literature [80]. In fact, the only recent report is that of MgH_2 nanoconfined in chemically-inert shells of CoS nano-boxes [80] (Table 4).

Table 4. Recent progress in oxides, sulfides and nitrides-based hosts for nanoconfined hydrogen storage systems.

Metal Oxide/Sulfide/Nitride	Hydrogen Storage Material	Nanoconfinement Method	Ref.
CoS nano-boxes (ZIF-67-derived)	MgH_2	infiltration $MgBu_2$ (1 M in heptane; 1000 rpm, 48 h), followed by hydrogenation (453 K, 4.8 MPa H_2, 24 h)	[80]
Al-SBA-15, γ-Al_2O_3	$LiBH_4$-$LiNH_2$	melt infiltration	[91]
Metal oxide nanoparticles (TiO_2) anchored on amorphous carbon (SCNPs/AC)	MgH_2	in-situ pyrolysis assisted with quickly cooling	[95]
$NiCo_2O_4$-anchored reduced graphene oxide (rGO)	$LiAlH_4$	low-temperature solution method coupled with annealing treatment; to yield $NiCo_2O_4$@rGO nanocomposites	[101]

Table 4. *Cont.*

Metal Oxide/Sulfide/Nitride	Hydrogen Storage Material	Nanoconfinement Method	Ref.
Fe_3O_4@C, Multifunctional porous scaffold of carbon wrapped ultrafine Fe_3O_4	$LiBH_4$	melting infiltration (300 °C, 30 min, 100 bar H_2)	[106]
Nb_2O_5@MOF (Zn-based MOF, ZIF-8 (Zn(2-methylimidazole)$_2$))	MgH_2	ball milling (400 rpm, 4 h, ball to powder ratio BPR 40:1) yielding MgH_2@7 wt.% Nb_2O_5@MOF	[147]
Ni/CoMoO$_4$ nanorods	MgH_2	ball milling (400 rpm, BPR: 60:1, 6 h); MgH_2 is the *host* for NiCoO$_4$/NiMoO$_4$ nanorods to yield MgH_2-10 wt.% Ni/CoMoO$_4$	[158]
Al_2O_3	γ-Mg(BH$_4$)$_2$	Atomic Layer Deposition (ALD)	[159]
B_2O (Metal-Decorated Honeycomb Borophene Oxide)	Li/LiH; Na/NaH and K/KH.	Theoretical study: dispersion corrected density functional theory (DFT-D2)	[160]
Al_2O_3	$LiBH_4$-LiI	melt infiltration (50 bar H_2, 295 °C, 3 °C min^{-1}, 30 min); 4LiBH$_4$:LiI–manual grinding in mortar, added to Al_2O_3 (130% pore filling)	[161]
(3D) boron nitride (BN)	AB (NH$_3$BH$_3$)	solvent impregnation of AB (6.92 M in THF) into mBN1000 and mBN1450	[162]
TiO_2 (anatase)	MgH_2	crystal-facet-dependent catalysis ({001} and {101})	[172]

4.5. Metal Component/Host

Several reports have been published where the host is an actual metal matrix, usually one that is highly active in hydrogenation studies (Table 5) [40,68,94,112,121,122,138,163–171].

Table 5. Recent progress in oxides, sulfides and nitrides-based hosts for nanoconfined hydrogen storage systems.

Metal as Host or Component	Hydrogen Storage Material	Nanoconfinement Method/Obs.	Ref.
Al	Al/AlH$_3$@MIL-101-NORIT-RB3 decorated	solvent impregnation	[40]
Pd	Pd@MOF	Various: Liquid impregnation, Metal-Organic Chemical Vapour Deposition; Sol-Gel; Double Solvent Method	[68]
TiC$_x$/Mg	Mg/MgH$_2$	reactive gas evaporation	[94]
N-doped graphene	$LiBH_4$	ball milling	[112]
Mg nanocrystals	Mg/MgH$_2$@GO; Mg/MgH$_2$@rGO	LiNp reduction in Cp$_2$Mg/(r)GO slurry in THF. Various degrees of GO reduction (to rGO) to fine tune H_2 storage properties by morphology modification of Mg confined in xGO/(1-x)rGO matrix.	[121]
Mg	Mg/rGO	One-step growth of Mg particles; chemical reduction in Cp$_2$Mg by Li-methyl-naphtalenide (LiNp^{Me}) in THF, followed by addition of the reactive mixture over single layer GO (30 min sonication). Mg w/high-index {2$\bar{1}\bar{1}$6} crystal surface exhibits increased hydrogen absorption up to 6.2 wt %.	[122]

Table 5. *Cont.*

Metal as Host or Component	Hydrogen Storage Material	Nanoconfinement Method/Obs.	Ref.
Mg	GO/Mg/MgH multilaminates	solution-based co-reduction method of $MgCp_2$/GO with NpLi	[138]
Mg@(rGO/Ni)	Mg/MgH_2	in situ reduction in (Cp_2Mg and Cp_2Ni)@GO,THF-sonicated slurry, with a THF sol. of LiN; 6.5 H_2 wt.% of total composite; H_2 uptake under 1 bar H_2.	[163]
Pd	Pd-Based Alloy Nanoparticles *RhPd-H NPs); $PdH_{0.43}$ NPs (when np Pd used, control experiment)	one-pot solvothermal method-reduction of acetylacetonates $Pd(acac)_2$ and $Rh(acac)_3$ in mixed benzyl alcohol /acetaldehyde solvents with polyvinylpyrrolidone (PVP), at 180 °C in 30 min. RhPd confirmed by EDX. (111) diffraction peak outside that of either Rh/Pd, implying an expanded structure due to interstitial H atoms.	[164]
Mg (as matrix)	Mg/MgH_2	(review) of solid-state processing: physical vapor deposition, powder blending and consolidation, and additive manufacturing.	[165]
Raney Ni (3 nm pore size) as host	$NaAlH_4$ to form $NaAlH_4$/Raney Ni	wet impregnation	[166]
Al/Ti (Ti-based doped porous Al scaffold)	$NaAlH_4$/Al	melt-infiltrated	[167]
Co	$2MgH_2$-Co (Mg_2CoH_5 and $Mg_6Co_2H_{11}$)	compression to pellets (4.43 wt.% hydrogen storage) vs. powder (2.32 wt.% capacity)	[168]
Mg	MgH_2 and ETM hydrides (ScH_2, YH_3, TiH_2, ZrH_2, VH and NbH)	mechanochemistry under hydrogen gas; 5 mol% of Early Transition Metals (ETM = Sc, Y, Ti, Zr, V, and Nb) as hydrogenation catalysts	[169]
Mg–Ti	Mg–Ti–H nanoparticle.(MgH_2 andTiH_2 crystalline phases)	gas-phase condensation of Mg and Ti vapors under He/H_2 atmosphere	[170]
Ni	AB/Ni matrix	$NiCl_2$ reduction to Ni(0) on the surface of AB nanoparticles (1–7 nm)	[171]

4.6. Gas Selective-Permeable Polymers

Attempts to restrict oxygen and moisture exposure of active hydrogenation sites in hydride materials have been made through the engineered approach of covering the hydride materials with a layer of H_2-permeable polymer [88,127,156,173–175]. This approach proved to be very successful, provided that the hydride coverage was indeed complete (Table 6).

Table 6. Examples of gas-selective H_2-permeable polymers used as covering shells for hydrogen storage systems.

H_2-Permeable Polymers	Hydrogen Storage Material	Nanoconfinement Details	Ref.
poly(acrylamide) (PAM)-grafted mesoporous silica nanoparticles (MSNs)	ammonia borane (AB)	solution infiltration (stirring of THF solution of AB and polymer for 2 h), to produce AB-PAM-COOH-MSNs and AB-PAM-COOHMSNs	[88]
polyaniline (Pani) or sulfonated polyetherimide (PEIS) as polymer matrices	$NaAlH_4$	PEIS/$NaAlH_4$ (70/30 wt.%): solution infiltration of $NaAlH_4$ added over dispersed MWCNTs in NMP-solubilized PEIS (30 min, 40 °C). Pani/$NaAlH_4$: dispersion of components (50 wt.%), w/2 mol.% TiO_2 as catalyst	[127]

Table 6. *Cont.*

H$_2$-Permeable Polymers	Hydrogen Storage Material	Nanoconfinement Details	Ref.
mesoporous polystyrene	various metal hosts	post-confinement strategy	[156]
Adaptive TPX™ Polymer Scaffold	Li-RHC (2LiH + MgB$_2$ + 7.5(3TiCl$_3$·AlCl$_3$))	ball milling of 2LiH + MgB$_2$ + 7.5 (3TiCl$_3$·AlCl$_3$) and a solution of TPX™ in cyclohexane	[173]
PTFE polytetrafluoroethylene; PMMA poly(methyl-methacrylate)	Pd or Pd$_{70}$Au$_{30}$ alloy	Pd@PTFe, Pd$_{70}$Au$_{30}$@PTFe, (Pd@PTFE@PMMA) acting as (tandem) sensors	[174]
short-chain polyethylene oxide (PEO or PEG)	AB (NH$_3$BH$_3$)	slow interaction of AB and PEO powders (microscope slide, 10 months. rt) forms ammonia borane–polyethylene oxide cocrystal (5 PEO monomers per AB molecule)	[175]

4.7. MXene

Ongoing recent trends in developing novel systems for energy storage have incorporated MXene materials with a 2D structure, as promising hydride hosts [94,156,176–194]. While only few examples are currently available, it is foreseeable that MXenes will grow to become a mainstream storage matrix for nanoconfined hydride-based materials (Table 7).

Table 7. Examples of MXenes used as hosts for hydrogen storage systems.

MXene Type	Hydrogen Storage Material	Nanoconfinement Method	Ref.
TiC$_X$	Mg/MgH$_2$	reactive gas evaporation method	[94]
Ti$_3$C$_2$T$_x$ (T = surface termination: OH, O or F)	Ni@C spheres	in situ confinement strategy	[156]
Ti$_3$C$_2$T$_x$ (T = F)	N/A	hydrogen trapping (physisorption, chemisorption, and Kubas type particle interaction)	[176]
Multilayer Ti$_3$C$_2$ (ML-Ti$_3$C$_2$)	MgH$_2$	ball milling MgH$_2$ + ML − Ti$_3$C$_2$	[177]
Ti$_3$C$_2$	LiAlH$_4$	ball milling LiBH$_4$-Ti$_3$C$_2$ (1 wt.%, 3 wt.%, 5 wt.%, 10 wt.%, and 15 wt.%); (planetary ball mill Retsch PM 400, under Ar, 250 rpm, 10 h, BPR 250:1); doping strategy to LiAlH$_4$, yielding LiAlH$_4$ + 5 wt.% Ti$_3$C$_2$	[178]
Ti$_3$C$_2$	4MgH$_2$-LiAlH$_4$	mechanical milling 4MgH$_2$-LiAlH$_4$ with additive Ti$_3$C$_2$ (10 wt.%) in planetary ball mill (24 h, 450 rpm, BPR 40:1, under Ar), forming 4MgH$_2$-LiAlH$_4$-Ti$_3$C$_2$ nanocomposites	[179]
Ti$_3$C$_2$	LiH + MgB$_2$	ball milling	[180]
Nb$_4$C$_3$T$_x$	MgH$_2$	ball milling MgH$_2$-5 wt.%Nb$_4$C$_3$T$_x$; chemical exfoliation of Nb$_4$C$_3$T$_x$	[181]
Cr$_2$C	N/A	First-principles studies (7.6 wt.% H$_2$)	[182]
Ti$_3$C$_2$	NaAlH$_4$	NaAlH$_4$-7 wt.% Ti$_3$C$_2$	[183]
(Ti$_{0.5}$V$_{0.5}$)$_3$C$_2$	MgH$_2$	MgH$_2$-10 wt.% (Ti$_{0.5}$V$_{0.5}$)$_3$C$_2$	[184]
Ti$_3$C$_2$	LiBH$_4$	40% Ti$_3$C$_2$ composite	[185]
Ti$_3$C$_2$	NaH/Al (Ti-doped NaAlH$_4$)	NaH/Al–Ti$_3$C$_2$	[186]
Ti$_3$C$_2$	Mg(BH$_4$)$_2$	Mg(BH$_4$)$_2$-40 wt.% Ti$_3$C$_2$ composite	[187]
C@TiO$_2$/Ti$_3$C$_2$	NaAlH$_4$	annealing Ti$_3$C$_2$ MXene under C$_2$H$_2$ atmosphere; 10 wt.% C@TiO$_2$/Ti$_3$C$_2$ catalyzing NaAlH$_4$	[188]
Ti$_3$C$_2$	Mg(BH$_4$)$_2$	ball-milling method; Mg(BH$_4$)$_2$–40Ti$_3$C$_2$	[189]
NbTiC solid-solution MXene	MgH$_2$	MgH$_2$-9 wt.% NbTiC	[190]

Table 7. *Cont.*

MXene Type	Hydrogen Storage Material	Nanoconfinement Method	Ref.
Ti_3C_2	$2LiH + MgB_2/2LiBH_4 + MgH_2$ (RHC-system)	ball milling	[191]
Ti_3C_2/TiO_2(A)-C	MgH_2	ball milling; sandwich-like Ti_3C_2/TiO_2(A)-C prepared by gas–solid method	[192]
Ti_3C_2	Mg/MgH_2	ball milling (50 bar H_2, 24 h) producing MgH_2-x wt.% Ti_3C_2 nanocomposites ($x = 0, 1, 3, 5$ and 7)	[193]
Ti_2N	N/A	first-principles calculations; 2.656–3.422 wt.% hydrogen storage capacity, ambient conditions	[194]

4.8. Catalytic Effects of Doping the Host and/or Substitution of the Hydride Species

Improvements on hydrogen release/uptake cycles have often been explored in conjunction with utilization of catalysts used to either dope the host, or the hydride material. This strategy is based on formation of active sites for hydrogenation reaction to occur, or is sometimes ascribed to the formation of a reactive intermediate species [19,68,92,102,111–113,117,125,128,151,160,161,163,195–197]. In addition, cation substitution or anion substitution in complex hydrides has been employed to reduce energy barriers and improve overall recyclability of the hydride materials (Table 8).

Table 8. Examples of host decoration/doping and hydride substitution in nanosized systems.

Host Doping/Hydride Substitution	Hydrogen Storage Material	Nanoconfinement Method	Ref.
Alkali/Alkaline Earth Metals (AM)	hydrides of lightweight elements (HLEs)	development of AM amide-hydride composites	[19]
Pd	Pd/PdH_x@MOF	complex interaction Pd . . . H	[68]
metal (Ni) or non-metal (N)-doping of carbon scaffold	MgH_2	xNi-CMK-3; N-CMK-3 (x = 1 and 5 wt.%)	[92]
Ni@N-doped carbon spheres	MgH_2	hydriding combustion and subsequent high-energy ball milling	[102]
Nitrogen-Doped Carbon Host	$LiAlH_4$	solution infiltration	[111]
N-doped graphene in resorcinol-formaldehyde	$LiBH_4$	ball milling, melt impregnation	[112]
N-Doped Graphene-Rich Aerogels Decorated with Nickel and Cobalt Nanoparticles	$LiBH_4$	melt impregnation	[113]
Edge-Functionalized Graphene Nanoribbon N_2-cGNR, N_4-cGNR, and fluorenone GNR (f-cGNR)	$Mg(/MgH_2)$	Rieke-like reaction (up to 98% Mg wt.%)	[117]
Ni-Containing Porous Carbon Sheets	$LiAlH_4$, $NaAlH_4$, and $Mg(AlH_4)_2$	high energy ball-milling	[125]
Nitrogen-Doped Nanoporous Carbon Frameworks	$NaAlH_4$	melt infiltration	[128]
Bipyridine-Functionalized MOF (UiO-67bpy)	$Mg(BH_4)_2$	solution infiltration, stirring (DMS dimethyl sulfide solution of $Mg(BH_4)_2$, RT, 2 h)	[151]
Li, Na, and K decorations on 2D honeycomb B_2O	N/A	theoretical study: dispersion corrected density functional theory (DFT-D2)	[160]
Al_2O_3	$LiBH_4$-LiI	partial anion substitution in the complex borohydride	[161]

Table 8. *Cont.*

Host Doping/Hydride Substitution	Hydrogen Storage Material	Nanoconfinement Method	Ref.
Ni, Cr and Mn/GO	Mg	in-situ reduction Cp_2Mg, and each transition metal precursor (Cp_2Ni) dissolved in THF (22.5 mL) added into GO solution, stirred for 30 min. Hydrogen absorption (125 °C, 15 bar H_2)/desorption (300 °C, 0 bar) Ni-doped rGO–Mg	[163]
Nitrogen doping	Nb	Suppression of nano-hydride growth on Nb(100)	[195]
Pd	Mg NPs; Pd@Mg NPs	Rieke method–co-reduction/precipitation of a Pd^{2+}:Mg^{2+} = 1:9 wt. ration (chloride source) in THF, using LiNp as reductant to form Pd@Mg NPs	[196]
Pd/Halloysite Nanotubes (HNTs)	AB (NH_3BH_3)	AB encapsulation and thin layer coating of the scaffold Pd/HNTs by solvent infiltration and solvent evaporation (THF) to yield AB@Pd/HNTs. Strong electrostatic adsorption (SEA) of ($[Pd(NH_3)_4]^{2+}$) is onto the external surface of HNTs, precursor reduction (H_2, 250 °C) to form (Pd/HNTs).	[197]

4.9. (Nano)Catalyst Addition

The overall enhancement of kinetic and thermodynamic parameters can be tuned by utilization of catalysts. This is usually implemented to improve behavior of systems that already show promising results including recyclability (Table 9) [19,20,34,43,57,65,68,77,82,92,102,108, 113,118,120,125,131,132,134,136,139,143,147,158,160,166–168,172,183–192,194,196–212]. Due to the greater applicability of this approach in the past few years, the Table 9 summarizes them based on classes of substances and their corresponding characteristics.

Table 9. Examples of recent advances using nanocatalysts to improve kinetic and thermodynamic properties of hydride-based systems in hydrogenation studies.

Hydrogen Storage Class	Hydrogen Storage Material	(Nano)Catalyst Utilized	Ref.
Li-based	$LiBH_4$	TiO_2 (activated carbon nanofibers); N-Doped Graphene-Rich Aerogels Decorated with Ni and Co NPs; Nano-synergy catalyst; Ti_3C_2	[108,113,120,185]
	$LiAlH_4$	Nickel-Containing Porous Carbon Sheets	[125]
Na-based	$NaAlH_4$	Ti; Nickel-Containing Porous Carbon Sheets; Raney Ni; Al; 2D titanium carbide; Ti-based 2D MXene; Two-dimensional $C@TiO_2/Ti_3C_2$	[82,125,166,167,183, 186,188]
Mg-based	Mg NPs, films	Pd; Ti	[196,211,212]
	MgH_2	VTiCr; catalysts (review); nanocatalysts; anatase TiO_2; core-shell CoNi@C; $TiMn_2$; Carbon scaffold modified by metal (Ni) or non-metal (N); nickel@nitrogen-doped carbon spheres; ultrafine Ni nanoparticles dispersed on porous hollow carbon nanospheres; Nb_2O_5 NPs @MOF; $Ni/CoMoO_4$ nanorods; Co; $(Ti_{0.5}V_{0.5})_3C_2$; ultrafine NbTi nanocrystals, from NbTiC solid-solution MXene; sandwich-like Ti_3C_2/TiO_2(A)-C; FeCo nanosheets; flake Ni nano-catalyst composite; Transition metal (Co, Ni) nanoparticles wrapped with carbon; TiH_2 thin layer; $MgCCo_{1.5}Ni_{1.5}$; $MgCNi_3$; supported Co–Ni Nanocatalysts	[34,43,57,60,65,77,92, 102,118,147,158,168, 184,190,192,201,202, 204,205,208–210]

**Table 9.** *Cont.*

Hydrogen Storage Class	Hydrogen Storage Material	(Nano)Catalyst Utilized	Ref.
Mg-based	MgB_2	$LiH + TiH_2$	[198]
	$Mg(BH_4)_2$	ultrafine Ni NPs; Ti_3C_2; various additives	[132,187,189,207]
	$Mg(AlH_4)_2$	Ni-Containing Porous Carbon Sheets	[125]
Al-based	α-AlH_3	TiF_3; Li_3N	[203,206]
RCH	$2LiH + MgB_2$	Ti_3C_2	[191]
	$2LiBH_4 - MgH_2$	$ZrCl_4$	[134,191]
AB	NH_3BH_3	ZIF-67-Derived Co@Porous Carbon; TiO_2(B) NPs; Pd/Halloysite Nanotubes;	[139,143,197]
Misc.	Pd	Pd@MOF	[68,200]
	B_2O	Li, Na, and K-Decorated	[160]
	Various hydrides	Alkali/Alkaline Earth Metals; Highly Dispersed Supported Transition Metal; metallic NPs supported on carbon substrates; Heterostructures	[19,20,131,199]
	Carbon aerogel	N-Doped Graphene-Rich Aerogels Decorated with Ni and Co NPs; $ZrCl_4$; NEt_3	[113,134,136]
	Ti_2N MXene	Pristine (DFT)	[194]

5. Inclusion Methods of Hydride Materials into Appropriate Host—State-of-the-Art and Limitations

5.1. Direct Synthesis

Starting from a commercially-available borohydride (such as $LiBH_4$, $NaBH_4$ etc.) and the corresponding salt of the metal (MCl_x), various novel borohydrides have been synthesized via the metathesis reaction (double exchange) (Equation (3)) [8,16].

$$MCl_x + x\, LiBH_4 \Rightarrow M(BH_4)_x + x\, LiCl \qquad (3)$$
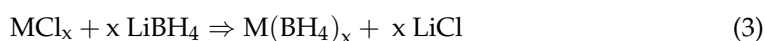
Other approaches start from the organometallic precursor of the metal, which undergoes reduction (with H_2 or another reductant, such as LiNp) typically after impregnation into the porous host. (Equation (4))

$$Mg(C_4H_9)_2 + 2\, H_2 \overset{\Delta}{\Rightarrow} MgH_2 + 2\, C_4H_{10} \qquad (4)$$
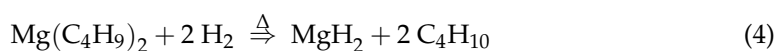
5.2. Infiltration Methods

5.2.1. Melt Infiltration

Melt infiltration of complex hydrides has widely been used to introduce the active hydride material into nanoporous hosts. This technique has the advantage of requiring no solvent (so it consists of less steps), but the hydride material must have a lower melting temperature, and the infiltration is carried out under H_2 pressure in order to avoid the onset of dehydrogenation reaction.

5.2.2. Solvent Infiltration

Solvent infiltration has become the method of choice as it achieves pore filling of the porous scaffold at temperatures that are near ambient, provided that a suitable solvent for the material has been identified. This is typically an issue, as solubility data on complex hydrides are rather scarce, and usually their solubility in ether-like solvents is limited [16].

5.2.3. Solvent-Assisted Ball-Milling

Nanoconfinement of hydride-based materials in nanoporous hosts has the potential advantage of bypassing the slow kinetics of their bulk counterparts, thus enabling a shorter refueling time, in pursuit of the DOE's current targets [5,6]. Very high surface area supports (MOFs, activated carbons) afford good hydrogen sorption capacities, but since the adsorption is mainly governed by physisorption, it is only relevant at 77 K. At this low temperature, a rough estimation (Chahine's rule) is that for pressures that would occupy all adsorption sites (exceeding 20 bar), the expected storage capacity is ~1 wt.%/500 m^2g^{-1} and scales proportional to the specific surface area [8]. Ball milling (with or without a solvent) can introduce the hydride material into the porosity of the employed scaffold. The process is energy-intensive and can proceed with an important increase in the local sample temperature, and therefore the process is carried out in steps (for instance, 20 min milling followed by a 10 min pause allowing controlled cooling).

6. Metal Hydrides and Their Recent Nanoconfinement Studies

Pristine metal hydrides have recently been comprehensively reviewed, and the results show promising trends upon nanoconfinement [213].

6.1. LiH

Alkali metal hydrides have been used for catalytic reactions, but have attracted attention due to their lightweight characteristics, as well as the high hydrogen gravimetric content. However, their high thermal stability makes them less attractive in their pure form; LiH, for instance, melts at 689 °C and decomposes at 720 °C into Li and H_2 (Equation (5)). Alkali metal hydrides have unusually high decomposition temperatures due to their salt-like nature (LiH, mp = 698 °C; NaH, mp = 638 °C; KH, mp ~ 400 °C with K vaporizing in H_2 current). Given their high decomposition temperature, alkali metal hydrides require kinetic and thermodynamic destabilization (Table 10).

$$LiH \overset{720\,°C}{\Rightarrow} Li + \frac{1}{2}H_2 \qquad (5)$$

Table 10. Hydrogen storage features of nanosized LiH materials.

Additive Used	Other H-Storing Source	H-Storing Composite	wt.% H$_2$	Obs.	Ref.
G(graphene)	(LiBH$_4$ and LiNH$_2$BH$_3$ after B$_2$H$_6$ and BH$_3$NH$_3$ reaction)	LiH@G (LiH nanospheres, 2 nm thick	6.8 wt.% (50 wt.% LiH in LiH@G); 12.8 wt.% (69.1 wt.% LiBH$_4$@G)	LiH@G T_{onset} = 445 °C, Td ≈ 500 °C (6.8 wt.%). LiNH$_2$BH$_3$@G T_{onset} = 53 °C, 15 °C lower than for bulk LiNH$_2$BH$_3$; Td ≈ 79 °C. LiBH$_4$@G T_{onset} = 346 °C (124 °C lower than that for bulk), 12.8 wt.%. Li$_2$B$_{12}$H$_{12}$ apparent in XRD after 4 cycles (LiBH$_4$@G).	[114]
TiCl$_4$.2THF	HSAG	LiH@HSAG	1.9 wt.% (340 °C, one step)	Hydrogenation of LiNp(THF) under 0.35 MPa H$_2$, 400 rpm, 40 °C, 12 h (cat.:TiCl$_4$.2THF)	[133]
N/A (TiH$_2$)	MgB$_2$	LiH/MgB$_2$	not investigated	different "top" and "bottom" fractions present in vial. At 700 bar H$_2$, 280 °C, 24 h, borohydride formation.	[198]
Activator: hν (light) to Au NPs	N/A (Au)	Au/LiH	11.1 wt.% (as-synthesized); 8.2 wt.% (heat desorption); 3.4 wt.% (light desorption)	plasmonic heating effect of Au NPs (100 °C), under Xe lamp radiation	[214]
LiNH$_2$	(Li$_3$N)	LiNH$_2$ + 2LiH	10.5 wt.%	Li$_3$N + 2H$_2$ = Li$_2$NH + LiH + H$_2$ = LiNH$_2$ + 2LiH. 2LiNH$_2$ = Li$_2$NH + NH$_3$	[215]
-	-	LiH	12.6 wt.%	LiH = Li + 1/2 H$_2$ T$_m$ = 689 °C; T$_d$ = 720 °C	[216]
Si	-	LiH	5 wt.%	Li:Si = 2.35:1; T$_d$ = 490 °C	[216]
Co(OH)$_2$	-	Li@SiO$_2$@Co(OH)$_2$	N/A	αLiOH + 2αLi$^+$ + 2αe$^-$ = α Li$_2$O + αLiH (0 < α < 1); High Li$^+$ storage in anode	[217]

Recently, a series of strategies have been utilized to produce nanosized LiH, but not all attempts dealt with hydrogen storage applications [114,133,198,214–216], and some utilizing LiH-containing nanocomposites for their Li-storage capacity in a Co(OH)$_2$-LiH novel anode material [217]. Even when dealing with potential hydrogen storage materials

like LiH + MgB$_2$, studies have focused on the phase-evolution process and XPS tracking thereof, rather than collection of hydrogen storage data [198]. Still, XPS data pointed to presence of LiBH$_4$, Mg$_{(3-x)/2}$Li$_x$(BH$_4$)$_x$ or Li-borate species present on account of multiple LiH-containing peaks identified [198]. At near-surface regions, LiBH$_4$ or mixed Li-Mg borohydrides can form at 100 °C below the threshold for hydrogenation of MgB$_2$; expectedly, LiBH$_4$ production scales with the LiH in the starting composite (Equation (6)) [198].

$$LiH + \frac{1}{2}MgB_2 + 2H_2 \overset{\Delta}{\Rightarrow} LiBH_4 + MgH_2 \tag{6}$$
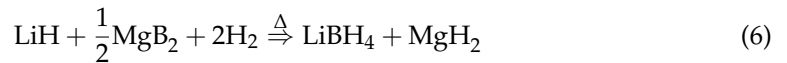
Sun et al., have shown that harnessing the plasmonic thermal heating effect of Au nanoparticles could lead to light-induced dehydrogenation of nanocomposites Au@LiH, which showed a 3.4 wt.% loss ascribed to dehydrogenation content [214]. The Au NPs dispersed on the surface of LiH, Mg or NaAlH$_4$ all showed marked improvements in hydrogenation studies. The preparation of Au/LiH composites involved LiH suspension in THF under sonication and overnight stirring at 500 rpm, after which a THF solution of HAuCl$_4$ was added and stirring continued for an additional 24 h, leading to the Au/LiH material after centrifugation and overnight drying by Schlenk line technique. Hydrogen absorption was carried out under 14.8 atm H$_2$, while desorption was conducted under 0.2 atm pressure, utilizing Xe lamp illumination affording 100 °C local temperature [214].

Overcoming kinetic and thermodynamic barriers in the complex Li-N-H system (Equation (7)) led White et al., to study the Li$_3$N effect on the LiNH$_2$ + 2LiH composite behavior [215]. On this occasion, a kinetic analysis showed the rate-limiting step is the formation of H$_2$ (g) at the surface of the core-shell structure Li$_2$NH@Li$_3$N [215]. Again, the use of TEM measurements was shown to be inappropriate for LiNH$_2$ materials, due to decomposition upon prolonged electron beam exposure. The equilibria shown in Equation (7) already occur upon the exposure of Li$_3$N to 10 bar H$_2$ (200 °C, 2 h), but not at one bar H$_2$, which only altered the α-to-β ration of Li$_3$N [215].

$$Li_3N + 2H_2 \overset{\Delta}{\Leftrightarrow} Li_2NH + LiH + H_2 \overset{\Delta}{\Leftrightarrow} LiNH_2 + 2LiH \overset{\Delta}{\Rightarrow} \frac{1}{2}Li_2NH + \frac{1}{2}NH_3 \uparrow \tag{7}$$

Considering the gravimetric hydrogen densities required by DOE standards, LiH, MgH$_2$ and AlH$_3$ are the main binary systems proposed to date [216]. Silicon doping of LiH has shown a drastic reduction in decomposition temperature (ΔT = 230 K), and could store up to 5 wt.% H$_2$ with release at 490 °C [216]. A nanostructured electrode of Co(OH)$_2$ and silica was recently employed in Li-conductivity studies and showed the formation of active LiH species, although the material was not investigated for its hydrogen storage properties [217].

A series of Li-based materials was investigated by Xia et al., who grafted on graphene LiH by in situ reduction in nBuLi with H$_2$ (110 °C, 50 atm), producing LiH@G. This nanocomposite LiH@G was further treated with B$_2$H$_6$ or AB/THF, and novel LiBH$_4$@G and LiNH$_2$BH$_3$@G nanocomposites were thus obtained (Equation (8)) [114].

$$G \overset{BuLi}{\Rightarrow} LiH@G \overset{B_2H_6}{\Rightarrow} LiBH_4@G \; ; \; G \overset{BuLi}{\Rightarrow} LiH@G \overset{BH_3NH_3}{\Rightarrow} LiNH_2BH_3@G \tag{8}$$

The 2D LiH nanosheets were about 2 nm thick and afforded a 6.8 wt.% H$_2$ storage when loaded at 50 wt.% in the said graphene-based nanocomposite, which withstood structural integrity upon further hydride-to-borohydride transformation (Figure 4) [114].
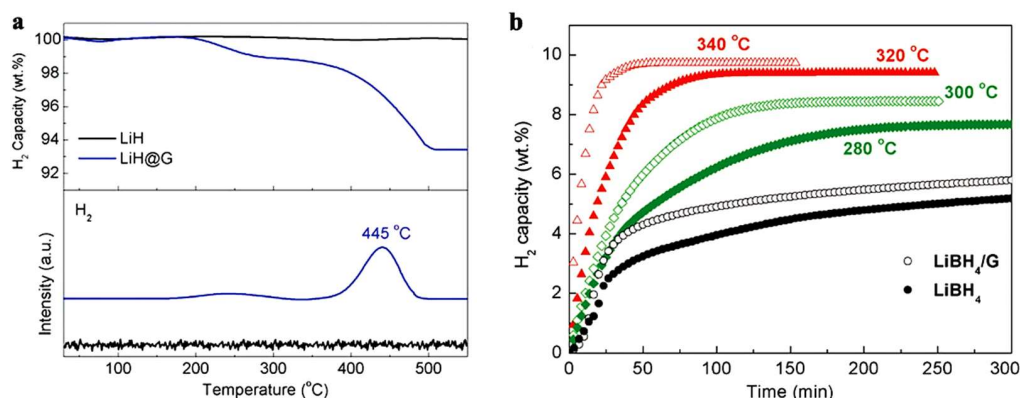
Figure 4. TG of as-prepared LiH@G (**a**), and dehydrogenation isotherm of LiBH$_4$@G (**b**). Reprinted/adapted with permission from Ref. [114]. 2017, Wiley, under CC BY 4.0 license.

Using HSAG (high surface area graphite) as scaffold, Wang et al., showed a 1.9 wt.% hydrogen storage at 200 °C for the composite LiH@HSAG, with reversible behavior at 300 °C and 60 bar H$_2$ (Equation (9)) [133].

$$\text{HSAG} \overset{\text{LiNp, TiCl}_4\text{THF}_2}{\Rightarrow} \text{LiH@HSAG} \qquad (9)$$

The morphology was tracked by SEM analysis and XRD diffraction, while hydrogenation data confirmed the modest 1.9 wt.% hydrogen storage by TGA (Figure 5).
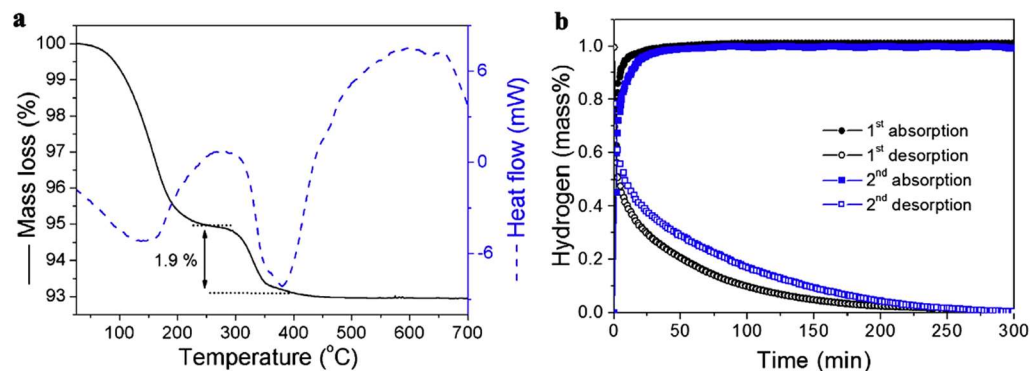
Figure 5. TGA/DSC for LiH@HSAG (**a**) and hydrogen desorption/absorption kinetics for LiH@HSAG at 350 °C (**b**). Reprinted/adapted with permission from Ref. [133]. 2016, Elsevier.

This nanoconfinement approach in high surface area carbon (HSAG) of pore size 2–20 nm showed a high thermodynamic improvement, allowing for hydrogen release at 340 °C in LiH@HSAG rather than at the high 680 °C for pristine LiH [133].

6.2. MgH$_2$

Due to its wide availability in nature, low cost, high gravimetric (7.6 wt.%) and volumetric (110 g/L) hydrogen storage capacities, the binary hydride, MgH$_2$, is arguably the most studied metal hydride and Mg-based materials have been investigated exhaustively by a variety of research groups (Table 11) [34,43,47,53,55,57,61,65,77,78,80,92,94,95,98,102,103,109,110,115,118,121,122,124, 130,134,137,146,147,149,158,168–170,172,177,196,198,201,202,204,205,208–212,214,216,218–225]. Synergistic effects of additives have been reviewed in the recent past: effect of nano-sized TMs (Ni, Cu, Fe, Co); salt addition in composites like MgH$_2$ + 10 wt.% LaCl$_3$; alloy formation Mg-La, Mg-Ni; incorporation in FeS$_2$ nanospheres; dispersion effect of Nb$_2$O$_5$ catalysis; TiF$_3$/TiO$_2$/TiN/TiMn$_2$ or Ti$_3$C$_2$ superior catalytic effects; Ni-based materials Mg@Ni binary nanocomposite; Mg$_2$Ni alloy; Mg$_2$NiH$_4$; Ni@MgH$_2$; NiB$_2$/NiS/Ni$_3$C/NiO/Ni$_3$N/Ni$_2$P; or carbon-based support influence (1D, 2D, 3D, graphene G, graphene oxide GO, MWCNT, etc.) (Table 11) [43,57,61,198,218–220,224].

The supporting role of a variety of carbonaceous hosts for MgH_2 storage properties has been reviewed by Han et al., who underlined the added structural stability, catalytic effect and nanosizing structuring on metal hydrides, and magnesium hydride in particular [110]. Le et al., have recently viewed (2021) the nanoconfinement effects on H_2-storage characteristics of MgH_2 (and $LiBH_4$) [47]. While conventional pressure-composition-temperature (PCT) data is time-consuming, an easier thermogravimetric analysis (TGA) was introduced by Zhou et al., to reliably determine abs./des. equilibrium temperature, and by using van't Hoff equation to deduce reaction enthalpies and entropies: $\Delta H_{abs} = 79.8$ kJ mol^{-1}, $\Delta S_{abs} = 141.1$ J mol^{-1}K^{-1}, and $\Delta H_{des} = 76.5$ kJ mol^{-1}, $\Delta S_{des} = 142.2$ J mol^{-1}K^{-1} for 5 at% VTiCr-catalyzed MgH_2 [34]. Some research produced nano-assemblies MgH_2@G (G = graphene) that was investigated as a material for high-performance Li-ion batteries (GMH composite with 50% MgH_2 has reversible 946 mAhg^{-1} at 100 mAh^{-1} after 100 cycles) [103]. The necessity to better predict the behavior of Mg-containing clusters (Mg_nH_m) that emerge as the Mg/MgH_x (m < 2n) system matures, has led to a machine-learning (M-L) interatomic potential evaluation for Mg-H systems [223]. Wang and Huang have shown that the ML approach is able to accurately describe the diffusion coefficients and the Arrhenius type temperature dependence for 128 < t < 427 °C, a temperature range relevant for the Mg/MgH_2 system in both pristine and nanoconfined conditions [223]. The diffusivity of H_2 through Pd NPs deposited on Mg film has revealed that unlike the H_2-impermeable MgO protective native film, the Pd-Mg interface can act as portals for hydrogenation of the Mg film [212].

Table 11. Hydrogen storage features of nanosized MgH_2 -based materials.

Additive/Host Used	Other H-Storing Source	H-Storing Nanocomposite	wt.% H$_2$	Obs.	Ref.
4 carbon aerogels, 15 < D_{avg} < 26 nm, surface area 800 < S_{BET} < 2100 m^2/g, and total pore volume, 1.3 < V_{tot} < 2.5 cm^3/g	Mg/MgH$_2$	MgH$_2$@C (MgH$_2$ loading: 17–20 vol%, 24–40 wt.%)	3.06 (Mg_CX1); degrades to 1.9 (Mg_CX1, 4th cycle, stable);	Mg(C$_4$H$_9$)$_2$(s) + 2H$_2$(g) ! MgH$_2$(s) + 2C$_4$H$_{10}$(g) 5 cycles des./abs. at 355 °C, 15 h (vacuup/des., 50 bar H$_2$/abs.) Mg_CX1, Mg_CX2 – 0.046 wt.%H$_2$/min (best result in this study). Highlights the importance of conducting des/abs cycles (different results obtained for "conditions 1 and 2").	[53]
Mg-B	Mg-B/MgH$_2$/ MgB$_{12}$H$_{12}$/Mg(BH$_4$)$_2$	Mg-B (MgB$_{0.75}$)	N/A (abs., 280 °C, 700 bar H$_2$, MgB$_{0.75}$), N/A (abs., 380 °C, 700 bar H$_2$, MgB$_2$),	nanoscale Mg–B material (MgB$_{0.75}$) made by surfactant ball milling MgB$_2$ in a mixture of heptane, oleic acid, and oleylamine	[55]
core-shell CoNi@C	CoNi: 2 coupled H-pumps: Mg$_2$Co/Mg$_2$CoH$_5$ and Mg$_2$Ni/Mg$_2$NiH$_4$,	MgH$_2$-8 wt.% CoNi@C	5.83 (275 °C, 1800 s); 6.17 (300 °C, 1800 s); 6 (150 °C, 200 s)	173 °C dehydrogenation onset for MgH$_2$-8 wt.% CoNi@C. Excellent thermal conductivity of the nanocomposite due to C-shell. $E_{a, des}$ = 78.5kJ mol^{-1}.	[65]
TiMn$_2$	Mg/MgH$_2$	MgH$_2$/10 wt.% TiMn$_2$	5.1 (reversible, 225 °C, 100 s, 10 barH$_2$/abs; 400 s, 0.2 bar H$_2$/des.)	cold pressing technique; potential for PEM fuel cell applications. $E_{a,des}$ = 82.9 kJ mol^{-1}; $E_{a,abs}$ = 19.3 kJ mol^{-1}. 414 cycles within 600 h continuously without degradations (hydrogen flow at an average rate of 150 mL/min)	[77]
Ni	Ni$_4$B$_3$ intermediate confirmed by XRNES	Ni-doped-2LiBH$_4$– MgH$_2$ in graphene	0.47 (0.48 theoretical)	ball milling 2LiBH$_4$-MgH$_2$-Ni/C (x = 0, 5, 10, 15). Heterogeneous nucleation of MgNi$_3$B$_2$. X-ray absorption near-edge structure (XRNES) used to probe intermediate Ni$_4$B$_3$ 3LiBH$_4$ + 4Ni = 3LiH + Ni$_4$B$_3$ + 4.5H$_2$	[78]
CoS nano-boxes scaffold	Mg/MgH$_2$; MgS-catalytic effect	MgH$_2$@CoS-NBs	3.17 (300 °C); 3.37 (400 °C)	hydriding and dehydriding enthalpies (−65.6 ± 1.1 and 68.1 ± 1.4 kJ mol^{-1} H$_2$. hydriding and dehydriding (57.4 ± 2.2 and 120.8 ± 3.2 kJ mol^{-1} H$_2$)	[80]

Table 11. *Cont.*

Additive/Host Used	Other H-Storing Source	H-Storing Nanocomposite	wt.% H_2	Obs.	Ref.
Ni- or N-doped C scaffold: xNi-CMK-3 (x = 1 and 5 wt.%) and N-CMK-3	Ni	MgH$_2$@xNi-CMK-3; MgH$_2$@ N-CMK-3	7.5 (MgH$_2$@5Ni-CMK-3); 6.5 (MgH$_2$@1Ni-CMK-3 and MgH$_2$@N-CMK-3) at 200 °C, 2 h	Hydrogenation is faster at 300 °C, MgH$_2$@5Ni-CMK-3, MgH$_2$@1Ni-CMK-3 and MgH$_2$@N-CMK-3 absorb 6 wt.% H$_2$ in 10 min (6.5 wt.%, 2 h). Enhanced kinetics, Ea: MgH$_2$@CMK-3 (125.3 ± 2.1 kJ mol^{-1}); MgH$_2$@N-CMK-3 (116.2 ± 1.8 kJ mol^{-1}), MgH$_2$@1Ni-CMK-3 (109.2 ± 1.3 kJ mol^{-1}), MgH$_2$@5Ni-CMK-3 (107.6 ± 1.2 kJ mol^{-1})	[92]
Mg-TiC$_X$@C	TiC$_x$	Mg-TiC$_X$@C	4.5 (des., 60 min, 300 °C); 5.5 (abs., 25 min, 250 °C)	TiC$_X$-decorated Mg nanoparticles (NPs) in 2–3 nm carbon shells through a reactive gas evaporation method. Mg$_{88}$(TiC$_{0.6}$)$_{12}$@C best results. Stable after 10 hydrogenation/dehydrogenation cycles at 250/300 °C.	[94]
Monodispersed single-crystal-like TiO$_2$ with amorphous carbon	-	Mg@C-TiO$_2$	6.5 (des. 275 °C, 10 min.); 6.5 (abs., 200 °C, 5 min)	reductions in hydrogen desorption temperature (163.5 °C) and E$_a$ (69.2 kJ mol^{-1}). The sample can be fully rehydrogenated with a reversible capacity of 6.5 wt.% at 200 °C within 5 min.	[95]
Graphene nanosheet (GN)	-	MgH$_2$@GN-40wt.%	4.5 (reversible, 6 cycles, 300 °C)	E$_a$ = 80.8 kJ mol^{-1} (des., 0.01 atm H$_2$) MgH$_2$ size tunable by adjusting MgBu$_2$/G wt. ratio before hydrogenation	[98]
nickel@nitrogen-doped carbon spheres	Ni/Mg$_2$NiH$_4$	MgH$_2$–Ni@NCS	4.3 (des.), 5.7 (abs.) in 8 min, 350 °C; 4.2 (abs., 60 min, 100 °C)	high-energy ball milling process; negligible degradation after 10 cycles. In situ formed Mg$_2$NiH$_4$ induced dehydrogenation of MgH$_2$ and prevented Mg agglomeration.	[102]
AlH$_3$@CNT	AlH$_3$	MgH$_2$/AlH$_3$@CNT	8.20 (des., 1 h, 200 °C); 5.61 (abs., 0.16 h, 250 °C)	CNTs: high specific surface area (550 m^2 g^{-1}), small diameter (6–8 nm), afford 60–80 nm crystal size nanocomposite MgH$_2$/AlH$_3$@CNT nanoparticles, releases H$_2$ at ~71 °C.	[109]
Graphene Nanosheet GNS	-	MgH$_2$ –10 wt.% GNS	5.1 (des., 20 min, 325 °C); 5.2 (abs., 10 min, 250 °C)	well-dispersed MgH$_2$ nanoparticles (~3 nm); confinement effect of graphene	[115]
ultrafine Ni nanoparticles dispersed on porous hollow carbon nanospheres	Mg$_2$Ni/Mg$_2$NiH$_4$	Ni loading up to 90 wt.% in composite catalyst; MgH$_2$-5 wt.% (90 wt.%Ni-10 wt.%CNS)	6.4 (reversible). 6.2 (des. 30 min, 250 °C; abs., 250 s, 150 °C)	Des. onset (190 °C) and des. peak (242 °C). Reversible capacity of 6.4 wt.% achieves after 50 cycles at a moderate cyclic regime.	[118]
Graphene oxide (GO), reduced graphene oxide (rGO)	-	MgH$_2$@GO, MgH$_2$@rGO (rGO50, rGO100, and rGO200)	6.25 (200 °C, 15 bar H$_2$, MgH$_2$@GO)	role of graphene defects; rGO is detrimental, as Ea is lower on defected GO. MgH$_2$@rGO: disturbed diffusion pathway of hydrogen atoms caused by the coalesced morphology	[121]
Reduced graphene oxide (rGO)	Mg/MgH$_2$	Mg/rGO	6.2 (des., 2 h, Mg{2$\bar{1}\bar{1}$6}) 5.1 (des, 2 h, (random)Mg/rGO)	preferential orientation of Mg/rGA nanocomposites was investigated: Mg growth on {0001} and {2$\bar{1}\bar{1}$6} planes of rGO Mg 2$\bar{1}\bar{1}$6) stabilizes hydrogen absorption thermodynamics	[122]
1D Carbon Matrix, fishbone shaped (CNF)	-	Ultrathin Mg Nanosheet @ 1D-C	6 (abs., 1 h, no catalyst, 200–250 °C); 6 (des, 1.5 h, 200–325 °C)	90% of the total capacity is absorbed within 1 h at all temperatures and desorbed within 1.5 h	[124]
AC activated carbon	LiBH$_4$	2LiBH$_4$-MgH$_2$ @AC (LB-MH-AC)	5.7 (theoretical); 2.56–4.55 (350 °C, abs. under 30–40 bar H$_2$)	melt infiltration of hydride in AC (400 °C, 40–50 bar H$_2$, 10 h) improvement of thermal conductivity of materials and temperature control system could alleviate wt.% decrease	[130]
ZrCl$_4$- doped carbon aerogel scaffold (CAS)	2LiBH$_4$–MgH$_2$	2LiBH$_4$–MgH$_2$@ ZrCl$_4$-CAS x wt.% (x = 50, 67, 75)	5.4 (5.7, theoretical, x = 50); 3.4 (3.8 th., x = 67); 2.5 (2.9 th., x = 75) at 301–337 °C	melt infiltration technique. Up to 97 and 93% of theoretical H$_2$ capacity released and reproduced, respectively. 2LiBH$_4$ + MgH$_2$ = 2LiH + MgB$_2$ + 4H$_2$ (350–500 °C)	[134]

Table 11. *Cont*.

Additive/Host Used	Other H-Storing Source	H-Storing Nanocomposite	wt.% H$_2$	Obs.	Ref.
3-D activated carbon with TM dispersion (Co, Fe, and Ni)	TM/(TM)H$_x$	MgH$_2$@3D-AC (MHCH)	6.63 (abs., 5 min, 180 °C, for Ni-MHCH-5); 6.55 (des., 75 min, 180 °C)	TEA ((HOCH$_2$CH$_2$)$_3$N)/NH$_2$NH$_2$ reduction in ^{n}Bu$_2$Mg-infiltrated 3D-C. MgH$_2$ embedded in 3D-AC with periodic synchronization of transition metals (MHCH). Excellent long-term cycling stability over ~435 h for MHCH-5. Ni more efficient than Co or Fe.	[137]
nano-TiO$_2$@C	Mg/MgH$_2$	MgH$_2$-10 wt.% TiO$_2$@C	6.5 (7 min, 300 °C, des.); 6.6 (10 min, 140 °C, abs.)	10 wt.% nanocrystalline TiO$_2$@C weakens the Mg-H bond, thus lowering desorption temperature	[146]
Nb$_2$O$_5$@MOF	Nb$_2$O$_5$@MOF	7 wt.% Nb$_2$O$_5$@ MOF doped MgH$_2$	6.2 (6.3 min, 250 °C; 2.6 min, 275 °C)	Desorption onset: 181.9 °C. E$_a$ = 75.57 ± 4.16 kJ mol^{-1} Absorption: 4.9 wt.% (6 min, 175 °C); 6.5 wt.% (6 min, 150 °C); E$_a$ = 51.38 ± 1.09 kJ mol^{-1} Capacity loss: 0.5 wt.% after 30 cycles	[147]
Ni-MOF (7.58 nm, 0.46 cm^{3}g^{-1})	Mg$_2$Ni/Mg$_2$NiH$_4$	MgH$_2$@Ni-MOF	4.03 abs-3.94 des (325 °C); 4.02 abs-3.91 des (350 °C); 3.95 abs = 3.87 des (375 °C). The Ni-MOF contribution (physisorption): 0.91 (325 °C); 0.85 (350 °C), 0.97 (375 °C), 0.88 (300 °C).	The abs/des plateau pressure: 4.63 atm/3.45 atm (325 °C). thermodynamics (−65.7 ± 2.1 and 69.7 ± 2.7 kJ mol^{-1} H$_2$ for ab-/desorption, respectively) and kinetics (41.5 ± 3.7 and 144.7 ± 7.8 kJ mol^{-1} H$_2$ for ab-/desorption, respectively) of Mg/MgH$_2$ in the MgH$_2$@Ni-MOF composite. The Ni-MOF scaffold acts as "aggregation blocker". shortened H diffusion distance results in the ultrafast H diffusion rate in the nanosized Mg/MgH$_2$. (C$_4$H$_9$)$_2$Mg + 2H$_2$ → MgH$_2$ + 2C$_4$H$_{10}$ (g) 2(C$_4$H$_9$)$_2$Mg + Ni(Ni-MOF) + 4H$_2$ → Mg$_2$NiH$_4$ + 4C$_4$H$_{10}$ (g) Mg$_2$NiH$_4$ = Mg$_2$Ni + 2H$_2$ (g)	[149]
(Ni/Co)MoO$_4$ nanorods	Mo/Mg$_2$Ni/Mg$_2$NiH$_4$	MgH$_2$-10 wt.% NiMoO$_4$ MgH$_2$-10 wt.% CoMoO$_4$	7.41 (319.4 °C, MgH$_2$) 6.51 (243.3 °C, MgH$_2$-10 wt.% NiMoO$_4$) 6.49 (277.6 °C, MgH$_2$-10 wt.% Co-MoO$_4$) from TPD up to 400 °C, 3°/min. 6 (des., MgH$_2$-NiMoO$_4$, 10min, 300 °C) 5.5 (abs., MgH$_2$-NiMoO$_4$, 10 min, 300 °C, 31.6 atm H$_2$)	Ni/CoMoO$_4$ were doped into MgH$_2$ ball milling method at 400 rpm with a ball-to-powder ratio of 60:1 for 6 h. superior promoting effect of NiMoO$_4$ over CoMoO$_4$; NiMoO$_4$ reacts with MgH$_2$ during the first dehydrogenation to in situ form Mg$_2$Ni and Mo^0, Mg$_2$Ni/Mg$_2$NiH$_{4'}$ mutual transformation upon hydrogen release/uptake is the well-known 'hydrogen pump'. Mo^0 played for the hydrogen storage in MgH$_2$: (i) it accelerates the hydrogen de/absorption of MgH$_2$ through weakening the Mg–H bonding; (ii) it facilitates the mutual 'Mg$_2$Ni/Mg$_2$NiH$_{4'}$. No tdn effect: ΔHabs./ΔHdes of −71.14/78.25 close to that of pure MgH$_2$: −72.42/74.08 kJ mol^{-1}	[158]
Co	Mg$_2$CoH$_5$ and Mg$_6$Co$_2$H$_{11}$	2MgH$_2$-Co	4.43 (pellet); 2.32 (powder)	high pressure compacting in pellet doubles H$_2$ storage	[168]
ScH$_2$, YH$_3$, TiH$_2$, ZrH$_2$, VH and NbH	Mg/MgH$_2$	0.95 MgH$_2$–0.05 (TM)H$_x$	≥5 wt.%	(TM)H$_x$ crystallite size of ~10 nm, obtained by mechanochemistry (RMB, reactive ball milling) MgH$_2$ + TM (Sc, Y, Ti, Zr, V, Nb) under H$_2$ pressure. Early Transition Metals (ETM) chosen by the known stability of their respective hydrides under normal conditions.	[169]
BiphasicMgH$_2$/TiH$_2$ within Mg–Ti–H NP	Mg/MgH$_2$	Mg–x at.%Ti–H NPs Mg-14Ti-H and Mg-63Ti-H (26–10 nm)	4 (x = 7); 2.2 (x = 35); 0.8 (x = 63) abs, full at 150 °C.	Equilibrium data for H$_2$ ab-/de-sorption by Mg/MgH$_2$ at low 100–150 °C range. Fast H$_2$ release from MgH$_2$ at 100–150 °C (no Pd catalyst). The free energy change at the TiH$_2$/Mg interface induces MgH$_2$ destabilization. Hydrogen uptake (100 s) and release (1000 s, 0.1 . . . 0.2 wt.%/min) for Mg–x at.%Ti–H NPs.	[170]

Table 11. *Cont.*

Additive/Host Used	Other H-Storing Source	H-Storing Nanocomposite	wt.% H$_2$	Obs.	Ref.
TiO$_2$ (anatase)	TiO$_2$/Mg	MgH$_2$-TiO$_2$	2.70 (abs, 500 s, 100 °C.); 4.5 (abs, 100 °C. 120 min); 5.3 (abs., 44 s, 200 °C) for MgH$_2$-5 wt.% TF70:	Influence of TiO$_2$ facets {001} and {101}: MgH$_2$-TiO$_2${001} superior properties. E$_{a,des}$ = 76.1± 1.6 kJ mol^{-1} for MgH$_2$-TF70	[172]
Multilayer Ti$_3$C$_2$ (ML-Ti$_3$C$_2$)	Ti$_3$C$_2$	MgH$_2$ + x wt.% ML-Ti$_3$C$_2$, x = 4, 6, 8, 10	6.45 (des.; 240 °C, 10 min.) 1.95–3.63 (des.; 140 °C, in 10–60 min). 6.47 (abs. 150 °C); 4.20 (abs., 75 °C)	Ti$_3$C$_2$ was introduced into MgH$_2$ by ball milling. ML-Ti$_3$C$_2$ prepared in-house, by chemical exfoliation.	[177]
Ti$_3$C$_2$	Mg/MgH$_2$	MgH$_2$-x wt.% Ti$_3$C$_2$ (x = 0, 1, 3, 5 and 7)	6.2 (x = 5; 1 min, 300 °C, des.); 6.1 (x = 5; 30 s, 150 °C)	MgH$_2$-5 wt.% Ti$_3$C$_2$ shows excellent dehydrogenation/hydrogenation kinetics (chargind/discharging in <1 min)	[193]
Pd	Pd/PdH$_x$; Mg-Mg$_6$Pd	Mg@Pd: γ-MgH$_2$, PdH$_{0.706}$	3 (abs, 50 °C, 2 h)	Mg NPs (40–70 nm). E$_{a,des}$ = 93.8 kJ/mol at 216.8 °C; E$_{a,des}$ = 44.3 kJ/mol at 50 °C. ΔH$_{des}$ = 72.7 kJ/mol; ΔH$_{abs}$ = −71.5 kJ/mol. Pd-Mg alloy important role.	[196]
FeCo nanosheets	FeCo (50nm)	FeCo-catalyzed MgH$_2$	6 (des., 9.5 min, 300 °C), 6.7 (abs, 1 min, 300 °C); 3.5 (abs, 10 min, 150 °C)	E$_{a,des}$ = 65.3 ± 4.7 kJ mol^{-1} (60 kJ mol^{-1} reduction from pristine MgH$_2$) E$_{a,abs}$ = 53.4 ± 1.0 kJ mol^{-1}	[201]
flake Ni nano-catalyst composite	Mg$_2$Ni/Mg$_2$NiH$_4$	MgH$_2$ + 5 wt.% Ni	6.7 (des., 3 min, 300 °C). 4.6 (125 °C, 20 min, 29.6 atm H$_2$)	E$_{a, des}$ = 71 kJ mol^{-1}; E$_{a,abs}$ = 28.03 kJ mol^{-1}.	[202]
TM (Co, Ni) nanoparticles wrapped with carbon	Mg$_2$Ni/Mg$_2$NiH$_4$	MgH$_2$-6%Ni/C	6.1 des. at 250 °C; 5.0 (abs., 100 °C, 20 s)	dehydrogenation temperature 275.7 °C. Absorption/desorption stability with respect to both capacity (up to 6.5 wt.%) and kinetics (within 8 min at 275 °C for dehydrogenation and within 10 s at 200 °C for rehydrogenation	[204]
TiH$_2$	-	MgH$_2$-TiH$_2$	6.45 (DFT)	MgH$_2$/TiH$_2$ interface is thermodynamically stable, and promotes the generation and diffusion of hydrogen.	[205]
MgCCo$_{1.5}$Ni$_{1.5}$	Mg$_2$NiH$_4$, MgC$_{0.5}$Co$_3$ and C catalysts (from MgCCo$_{1.5}$Ni$_{1.5}$)	Mg/MgH$_2$-MgCCo$_{1.5}$Ni$_{1.5}$	6.1–6 (abs, 5 min, 350 °C, 1st cycle-10th cycle); 5.9-5.8 (des, 1st cycle-10th cycle)	ball-milling and hydriding combustion method. Desorbs H$_2$ at 216 °C (onset). E$_{a,des}$ = 39.6 kJ mol^{-1}	[208]
MgCNi$_3$	MgCNi$_3$	MgH$_2$-MgCNi$_3$	4.42 (abs, 150 °C, 1200s)	Mg-MgCNi$_3$ composite shows excellent cyclic stability with a 98% retention rate.	[209]
Co–Ni Nanocatalysts	Mg/MgH$_2$	0.95MgH$_2$–0.5(CoNi(OH)$_x$); Ni@G-doped MgH$_2$; CoNi@G-doped MgH$_2$	6.5 (des, Ni@G-doped MgH$_2$, 45 min, 260 °C; or 25 min, 280 °C)	ball milling MgH$_2$ and Co-Ni, 5 bar H$_2$, 2 h, 400 rpm, 20:1 BPR. Co-subst. of Ni changes shape of catalyst (sphere-to-plate) and decreases catalytic efficiency.	[210]
Mg-Ti-H nanoparticles	Mg/MgH$_2$	Mg-x Ti-H NPs (x = 14 … 63 at.%)	4.2 (22 at.%Ti, at 100 … 150 °C)	gas phase condensation of mixed Mg-Ti vapors under H$_2$. E$_{a,abs.}$ 43 … 52 kJ/mol, the rate constant (150 °C) increases from 2.7×10^{-2} s^{-1} to 9.2×10^{-2} s^{-1} with increasing [Ti]. Hydrogen desorption: sequence of surface-limited (E$_a$ = 32 kJ/mol) and contracting-volume kinetics, except at the highest Ti content where nucleation and growth is observed. k$_{des}$ (at 150 °C) increases from 0.5–10^{-3} s^{-1} to 1.2×10^{-3} s^{-1} with [Ti]. The activation energy for H$_2$ recombination is remarkably small (~32 kJ/mol)	[211]

Table 11. *Cont.*

Additive/Host Used	Other H-Storing Source	H-Storing Nanocomposite	wt.% H$_2$	Obs.	Ref.
light activation, Au(HAuCl$_4$)	-	Mg@Au, hν	5.2 (350 °C, 3 h, Mg$_{bulk}$); 4.9 (350 °C, 3 h, MgH$_2$-Au 5 wt.%)	Rehydrogenation at 12 h illumination, 14.8 atm H$_2$. No H$_2$ release at 100 °C, limited at 200 °C (0.7 wt.%) and at 300 °C (1wt.%) for Mg@Au 5 wt.%.	[214]
-	-	ultrafine MgH$_2$	6.7 (reversible; abs: 360 min, 30 °C; or 60 min, 85 °C, 30 bar H$_2$); vol capacity: 65.6 gH$_2$/L	novel metathesis process of liquid–solid phase driven by ultrasonication (2 h) was proposed from THF. Pressed into pellet under 200 MPa.Stable and rapid hydrogen cycling behavior in 50 cycles at 150 °C. Equilibrium pressure: 0.0304 (120 °C), 0.151 (160 °C), 1.014 (215 °C), 30-20-10 times higher than that of pristine MgH$_2$.	[222]
Mg(B$_3$H$_8$)$_2$	Mg(B$_3$H$_8$)$_2$	Mg(B$_3$H$_8$)$_2$-MgH$_2$	2.16 (93.6 . . . 138 °C)	Synergistic role in Mg(B$_3$H$_8$)$_2$-MgH$_2$ composite. No H$_2$ release below 150° for the pristine components.	[224]

Jia et al., have utilized a Ni- or N-doped carbon scaffold for MgH$_2$ nanoconfinement [92]. The carbonaceous support features high surface area, pore volume and narrow PSD (pore size distribution) and constitutes a C-replica of the mesoporous 2D-silica, SBA-15. Two Ni-loadings have been investigated: MgH$_2$@xNi-CMK-3 (x = 1 and 5). Expectedly, the higher Ni-containing sample MgH$_2$@5wt.%Ni-CMK-3 showed 7.5 wt.% storing capacity, whereas the MgH$_2$@1wt.%Ni-CMK-3 and MgH$_2$@ N-CMK-3 showed 6.5 wt.% hydrogen (Figure 6). The behavior of the nanocomposites has been investigated at 200, 250, 280 and 300 °C, and showed marked improvement scaling with temperature; at 300 °C, all three nanocomposites absorb 6 wt.% in 10 min (6.5 wt.% in 2h). The samples were degassed for 2 h at 350 °C prior to conducting absorption measurements (Figure 6) [92].
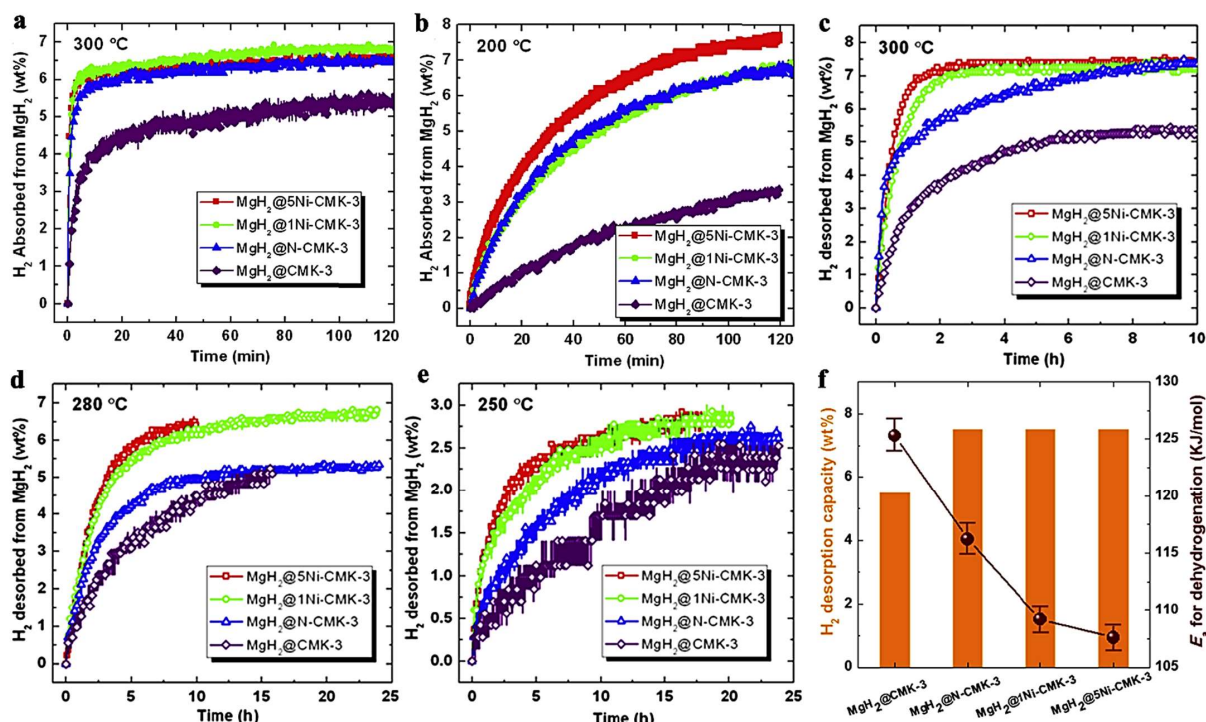
Figure 6. Hydrogenation kinetics of MgH$_2$@CMK-3, MgH$_2$@N-CMK-3 and MgH$_2$@xNi-CMK-3 (x = 1 and 5) at 300 °C (**a**) and 200 °C (**b**) and under 19.74 atm. H$_2$ backpressure. Hydrogen desorption profiles of the four investigated samples at 300 °C (**c**), 280 °C (**d**), 250 °C (vacuum, *p* < 0.01 atm) (**e**). Dehydrogenation of nanocomposites within two hours at 300 °C and corresponding desorption activation energies. E$_{a,des}$ (**f**). Reprinted/adapted with permission from Ref. [92]. 2017, Elsevier.

The enhancement in kinetics was obvious; van't Hoff plot analysis revealed systematic decrease of the activation energy barrier in the order: MgH$_2$@CMK-3 (125.3 $\pm$ 2.1 kJ mol^{-1}) > MgH$_2$@N-CMK-3 (116.2 $\pm$ 1.8 kJ mol^{-1}) > MgH$_2$@1Ni-CMK-3 (109.2 $\pm$ 1.3 kJ mol^{-1}) > MgH$_2$@5Ni-CMK-3 (107.6 $\pm$ 1.2 kJ mol^{-1}) [92].

Zhang et al., have dispersed TM-oxides (TiO$_2$ in particular) on amorphous carbon to achieve excellent, reversible hydrogen storage capacity, releasing in 10 min. at 275 °C, 6.5 wt.% hydrogen (85.5% that of pristine MgH$_2$) (Figure 7) [95]. Notably, the activation energies for desorption (E$_{a,des}$) and absorption (E$_{a,abs}$) have been considerably reduced compared to bulk magnesium hydride (Figure 7a). In a multi-fold enhancement strategy, the MgH$_2$ was first dispersed on carbon (MgH$_2$ + C), which showed modest improvements (<1 wt.% H$_2$) over MgH$_2$ bulk with no dehydrogenation in the same timespan (Figure 7c), TiO$_2$ was used as additive for MgH$_2$ to yield composites of MgH$_2$ + TiO$_2$ NPs, which surprisingly released ~6 wt.% H$_2$ in 10 min [95]. Driven by these enhancements, nanocomposites of the type MgH$_2$ + TiO$_2$ SCNPs/AC were synthesized, which further improved hydrogen release/uptake: even at 50 °C, over the course of 20 min, ~1.5 wt.% H$_2$ is released, whereas at 125 °C (~4.8 wt.%) and at 200 °C (6.5 wt.%) the kinetics is sped up considerably (Figure 7c–e). The rehydrogenation occurs within 5 min at 200 °C, and full recovery of the hydrogen storage capacity is achieved (6.5 wt.%). In addition, no appreciable hydrogen storage loss was recorded up to the 10th cycle (Figure 7f) [95].
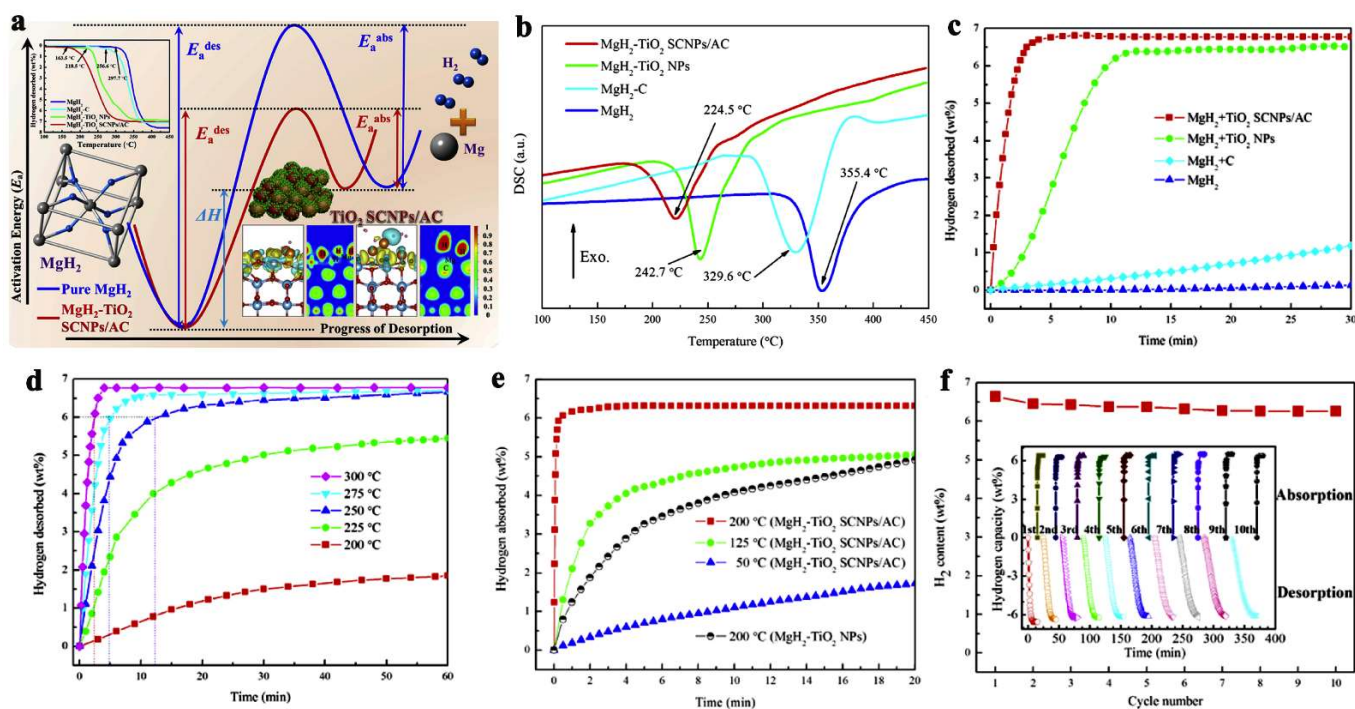
Figure 7. Schematic mechanistic approach in catalytic behavior of MgH$_2$-TiO$_2$ SCNPs/AC (**a**). DSC (**b**) of the investigated samples: ball-milled MgH$_2$, MgH$_2$-C, MgH$_2$-TiO$_2$ NPs and MgH$_2$-TiO$_2$ SCNPs/AC. Isothermal desorption curves of the four investigated samples at 300 °C (**c**); Isothermal desorption curves of MgH$_2$-TiO$_2$ SCNPs/AC and MgH$_2$-TiO$_2$ NPs at various temperatures in the range 50 . . . 300 °C (**d,e**); confirmation of reversible hydrogen storage capacity of MgH$_2$-TiO$_2$ SCNPs/AC at 300 °C recharging pressure of 50 bar H$_2$ (**f**). Reprinted/adapted with permission from Ref. [95]. 2019, Elsevier.

Using an FeCo nanocatalyst (mean size of 50 nm), Yang et al., synthesized composites MgH$_2$ + nano-FeCo able to recharge to 6.7 wt.% hydrogen in one minute at 300 °C, and could desorb 6 wt.% (9.5 min, 300 °C) (Figure 8) [201]. In fact, even treatment under H$_2$ backpressure at 150 °C produced 3.5 wt.% absorption in 10 min (Figure 8b). This highlights the importance of catalyst chosen, but also its morphology (nanosheets in the

case of FeCo-nano). Plotting the Arrhenius equation also yielded the apparent activation energies: $E_{a,des}$ = 65.3 ± 4.7 kJ mol^{-1} (60 kJ mol^{-1} reduction from pristine MgH$_2$), and the absorption energy $E_{a,abs}$ = 53.4 ± 1.0 kJ mol^{-1} (Figure 8d). Gratifyingly, the FeCo-catalyzed magnesium hydride composite was able to rehydrogenate fully and was tracked over the course of 10 hydrogen release/uptake cycles (Figure 8h) [201].
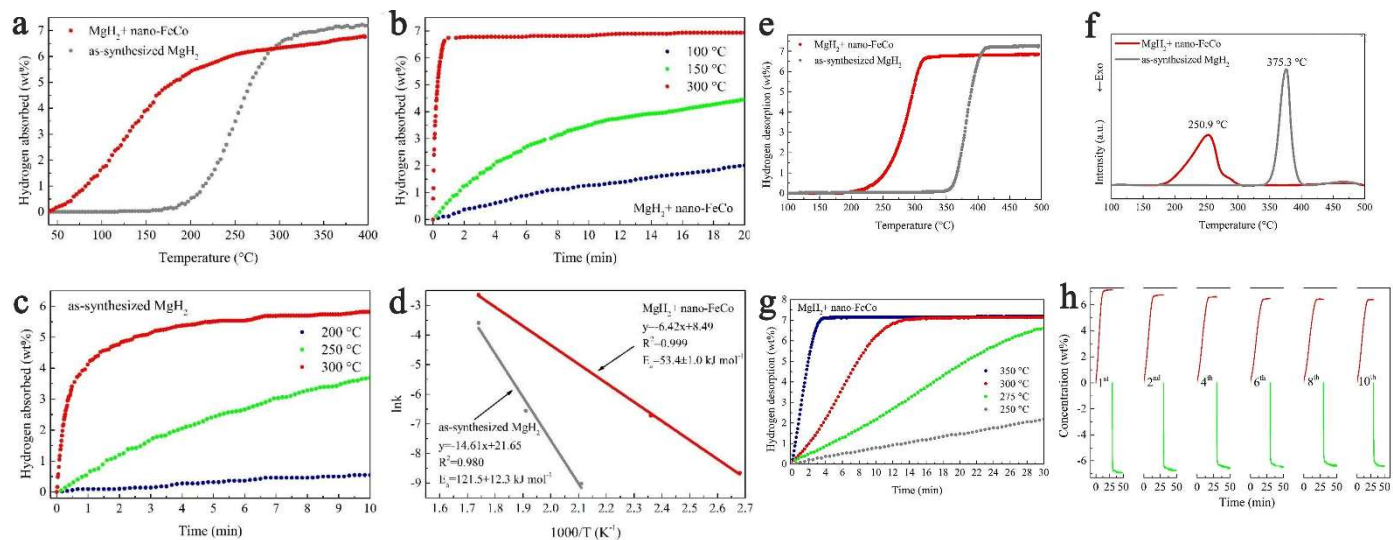

Figure 8. Non-isothermal hydrogenation curves (**a**); isothermal hydrogenation curves at different temperatures (**b**,**c**) and the corresponding Arrhenius plot of MgH$_2$ with and without nano-FeCo (**d**); non-isothermal dehydrogenation curves (**e**); DSC curves with a heating rate of 5 °C min^{-1} of MgH$_2$ with and without nano-FeCo (**f**); isothermal dehydrogenation curves of MgH$_2$ + nano-FeCo composite at 250, 275, 300, 350 °C (**g**); dehydrogenation (in red) and rehydrogenation (in green) curves of MgH$_2$ + nano-FeCo composite in the 1st, 2nd, 4th, 6th, 8th and 10th cycle (**h**). Reprinted/adapted with permission from Ref. [201]. 2019, Royal Society of Chemistry.

The thermodynamic predictions that smaller size NPs will show the most important destabilization, Zhang et al., have produced ultrafine MgH$_2$ that was able to release and recharge hydrogen under ambient temperature, with a very high hydrogen storage capacity of 6.7 wt.% (Figure 9) [222]. This capacity was checked over 50 cycles, and showed virtually the same high-capacity behavior (Figure 9). The conditions employed for reversible behavior were 360 min at rt (6.7 wt.%), or 60 min at 85 °C (6.7 wt.%), under 30 bar H$_2$. This unexpectedly high storage capacity (65.6 g H$_2$/L) surpasses even DOE's requirement (50 gH$_2$/L), and was possible solely on account of well-designed, size-restriction of MgH$_2$ to nanoscale [222].

Using a nanoflake Ni catalyst, Yang et al., have synthesized MgH$_2$ + 5 wt.% Ni, composites able to store 6.7 wt.% hydrogen (des., 300 °C, in 3 min) (Figure 10). The absorption was also very fast, achieving 4.6 wt.% at 125 °C in 20 min, under 29.6 atm H$_2$ [202]. The results also translate into much lowered activation energies (Arrhenius plot): $E_{a,des}$ = 71 kJ mol^{-1}; $E_{a,abs}$ = 28.03 kJ mol^{-1}.
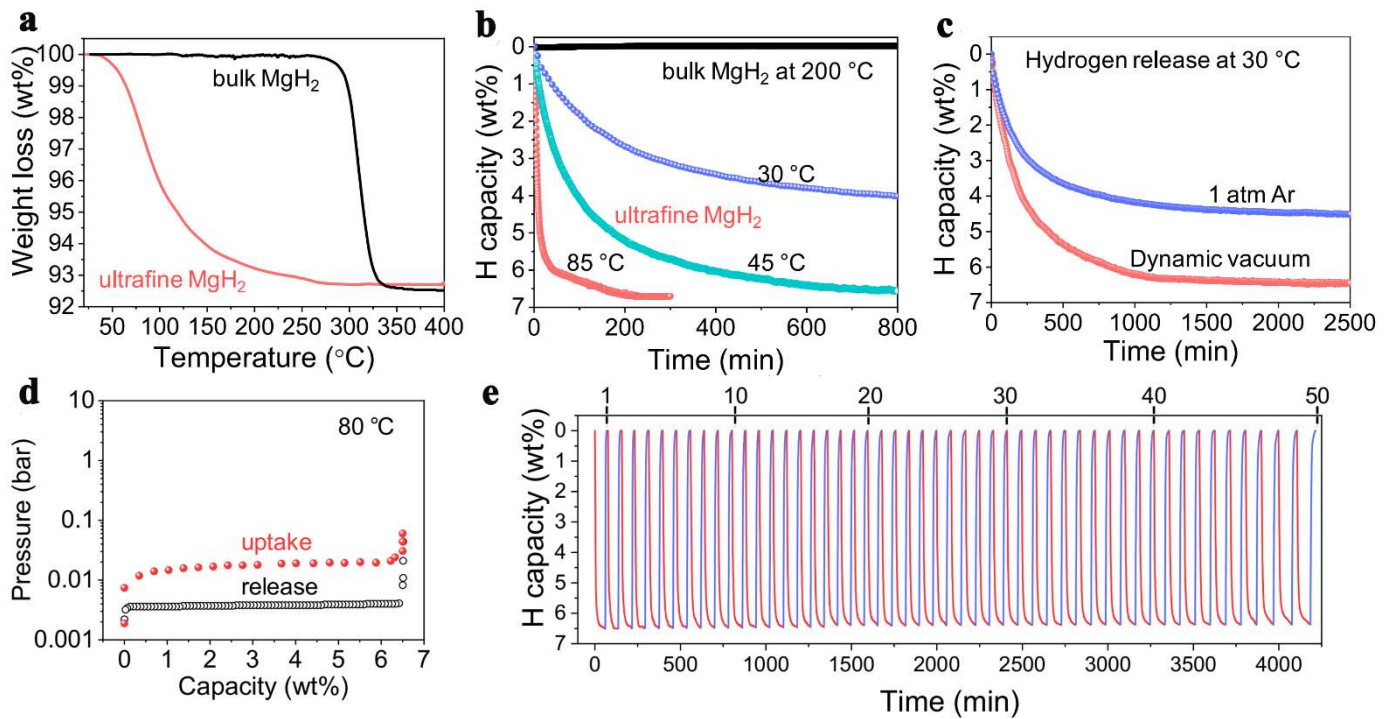
Figure 9. TGA (**a**), isothermal TGA dehydrogenation (**b**), isothermal TGA dehydrogenation under different conditions (**c**), PCI curves measured at 80 °C (**d**); cycling stability of non-confined ultrafine MgH$_2$ (**e**). Reprinted/adapted with permission from Ref. [220]. 2018, Elsevier B.V.
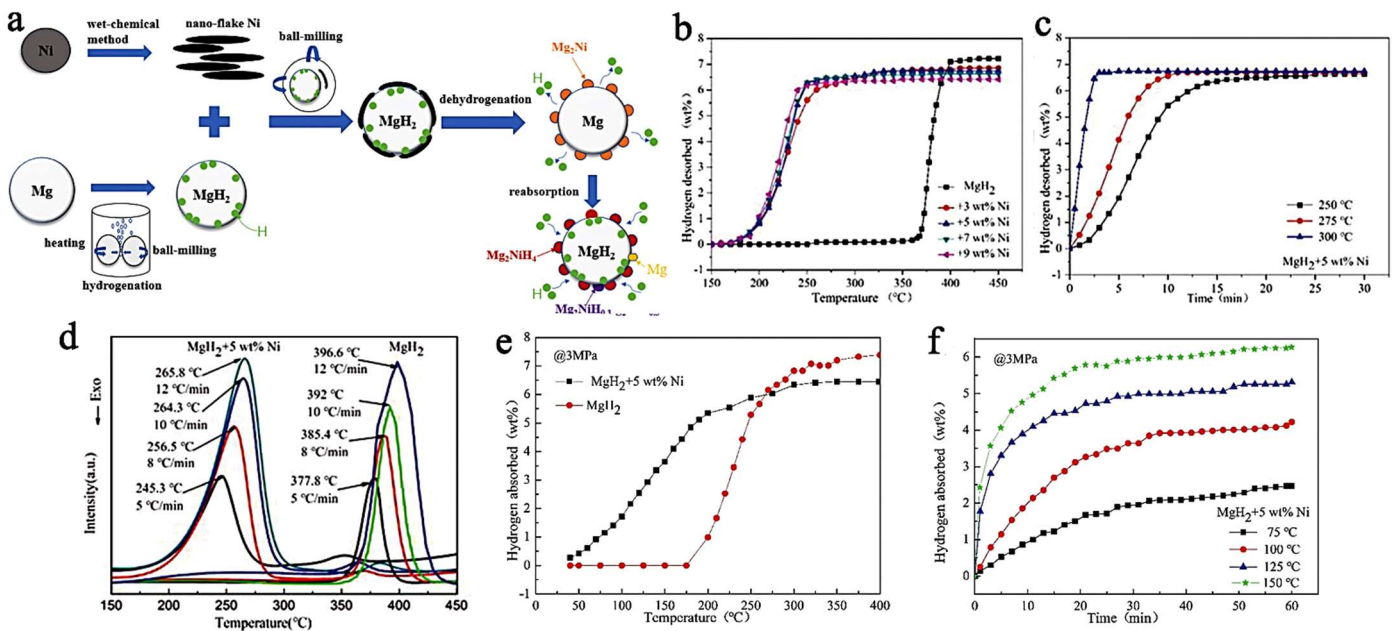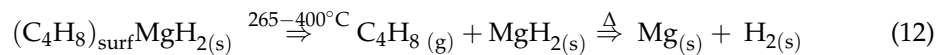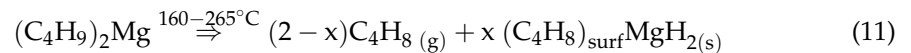

Figure 10. Preparation and reaction evolution in the MgH$_2$+Ni composite (**a**); the rising temperature dehydrogenation curve (**b**); Isothermal dehydrogenation curves of MgH$_2$ + 5 wt.% Ni at different temperatures (**c**); DSC curves of MgH$_2$ + 5 wt.% Ni at different rates of increasing temperature (**d**); Non-isothermal hydrogenation curves of MgH$_2$ with and without 5 wt.% Ni (**e**); Isothermal hydrogen absorption curves at different temperatures of MgH$_2$ + 5 wt.% Ni (**f**). Reprinted/adapted with permission from Ref. [202]. 2021, Royal Society of Chemistry.

These results have been explained by means of the intermediate Mg$_2$Ni intermediate, which is an intermetallic well-known in the Mg-Ni systems, and which absorbs

rapidly H_2 to form Mg_2NiH_4. This functions as an effective "hydrogen pump" (Figure 10a) (Equation (10)) [202].

$$Mg_2Ni + 2H_2 \overset{\Delta, p}{\Leftrightarrow} Mg_2NiH_4 \tag{10}$$
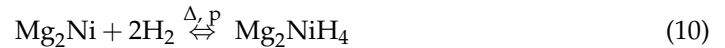
Decomposition of $^nBu_2Mg$ typically used as an organometallic precursor to Mg/MgH_2 NPs can follow two different steps, depending on the reaction temperature (Equations (11) and (12)).

$$(C_4H_9)_2Mg \overset{160-265°C}{\Rightarrow} (2-x)C_4H_{8\,(g)} + x\,(C_4H_8)_{surf}MgH_{2(s)} \tag{11}$$

$$(C_4H_8)_{surf}MgH_{2(s)} \overset{265-400°C}{\Rightarrow} C_4H_{8\,(g)} + MgH_{2(s)} \overset{\Delta}{\Rightarrow} Mg_{(s)} + H_{2(s)} \tag{12}$$

However small it might be, nanosized matter in general is also more reactive towards various gases and substrates, and Mg/MgH_2 coupled system is no exception. Previous examples have overcome this downside by either pressing the nano-powders into pellets, or capping them with other reagents. There are however many reports where MgH_2 has been introduced in the porosity of a carbonaceous host, such as the 3D activated carbon utilized by Shinde et al., to achieve a reversible hydrogen storage of 6.63 wt.% (Figure 11) [137]. Not only was the nanocomposite $MgH_2@3D$-C storing hydrogen under relatively mild conditions 6.63 wt.% (five minutes, 180 °C), but the desorption was likewise fast (6.55 wt.%, 75 min, 180 °C), and perhaps more importantly, the nanoconfined MgH_2 was air-stable thanks to the protective carbon shell [137]. To the observed enhanced kinetics and improved thermodynamic behavior contribute decisively the transition metal dispersed into the 3D carbon: NI>Co >Fe. Running in a continuous regime, the nanocomposite was able to cycle for about 435 h (more than 18 days), without a palpable decrease in the hydrogenation storage capacity (Figure 11) [137].

While typically reduction in $^nBu_2Mg$ infiltrated into a nanoporous host to afford MgH_2 NPs is carried out in heterogeneous conditions (under H_2 pressure), Shinde used a mixed reductant system: TEA $((HOCH_2CH_2)_3N)/NH_2NH_2$ hydrazine to reduce Mg(II) to Mg(0) [137]. The synthetic procedure is nicely followed in Figure 11, and in this case, both scanning electron microscopy (SEM) and transmission electron microscopy (TEM) could be used for characterization, since the electron beam no longer hits directly the MgH_2 NPs; thus, the risk of in-situ decomposition during data acquisition is minimized (Figure 11). The hydrogen storage capacity exceeds 6 wt.% in case of Ni-NPs deposited in the 3D-AC (MHCH-5), confirming the beneficial and synergistic role of Ni when used in conjunction with MgH_2. The plausible intermediate Mg_2Ni forms the coupled system Mg_2Ni/Mg_2NiH_4 during hydrogenation, and this can be held responsible for the superior cycling behavior in case of $MgH_2@3D$-AC (MHCH)-5(Ni), whereas this type of intermetallic is not common for Co or Fe [137].

The self-assembled MgH2 NPs are well embedded into the carbonaceous host, which plays a critical role in the overall performance of MHCH-5. It is implied, based on the thermal conductivity data (Figure 11h), that the carbon shell is important. The high thermal conductivity (70 W/mK), many times higher than that of MgH_2 NPs themselves, induces a lower temperature gradient in the sample and a high heat transfer coefficient, thus contributing to the exemplary behavior of the sample during hydrogenation cycling [137].
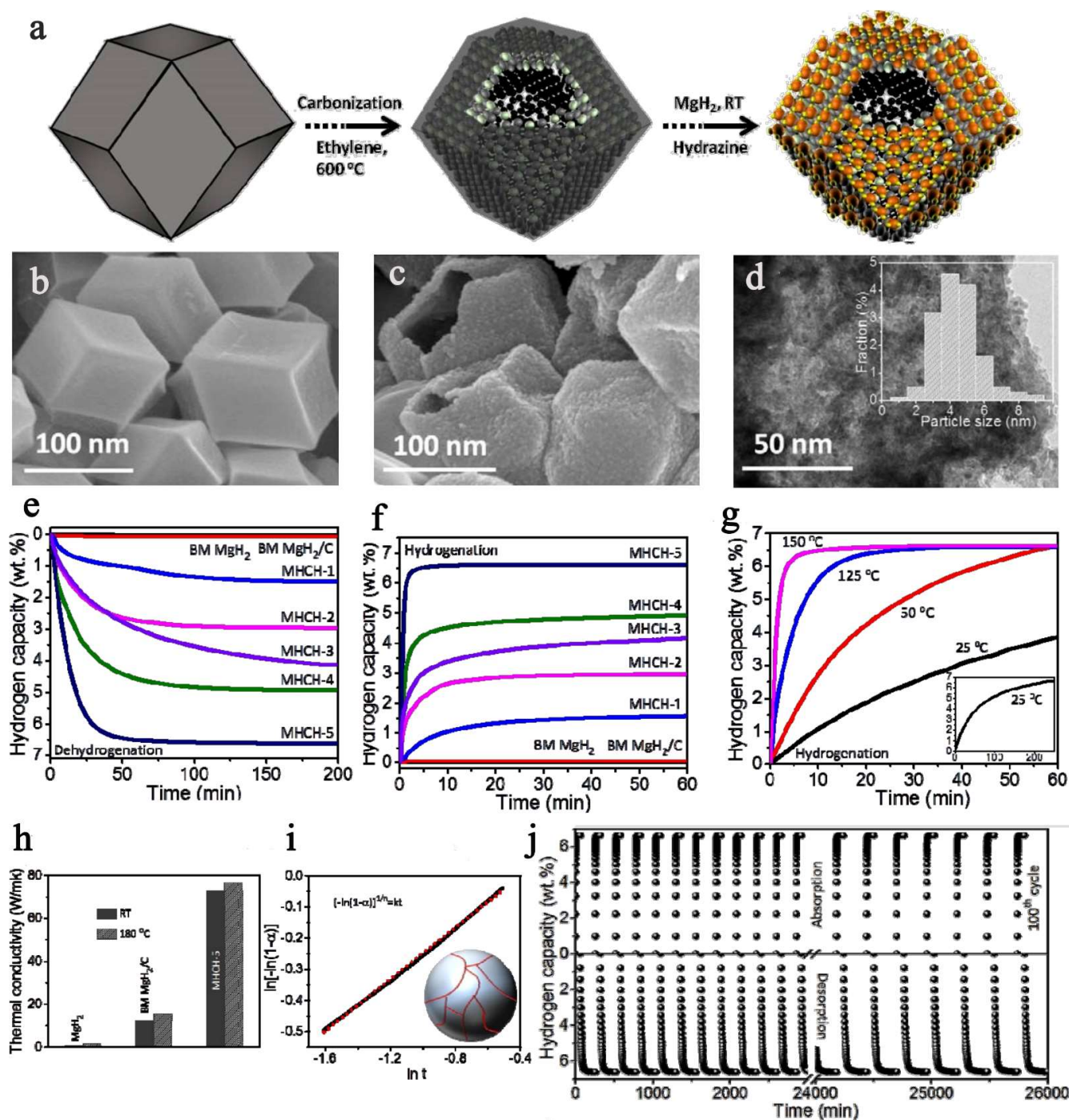
Figure 11. (**a**) Schematics displaying the self-assembled MgH_2 on three-dimensional metal interacted carbon. (**b**) SEM image of prepared metal-interacted 3-D carbon; (**c**) SEM, (**d**) TEM images of the MHCH-5; (**e**) dehydrogenation of the as-synthesized MHCH samples at 180 °C in comparison to ball-milled MgH_2 and MgH_2/C; (**f**) Isothermal hydrogenation; (**g**) Hydrogen absorption of the MHCH-5 for different temperatures—the inset (**g**) shows the hydrogen absorption property of the MHCH-5 at 25 °C, over a long time period; hydrogenation and dehydrogenation were performed under hydrogen pressures of 10 bar and 0.01 bar, respectively; (**h**) Thermal conductivity variation in MHCH-5, MgH_2, and ball-milled MgH_2/C for ambient temperature and 180 °C; (**i**) The growth mechanism of MgH_2 in MHCH samples correlating with a Johnson–Mehl–Avrami model. (**j**) Reversible hydrogen (under 10 bar H_2 pressure) and dehydrogenation (under 0.01 bar H_2 pressure) performance of the MHCH-5 at 180 °C. Reprinted/adapted with permission from Ref. [137]. 2017, The Royal Society of Chemistry; RSC Pub.

6.3. AlH$_3$

Alane (AlH$_3$) is a metastable hydride, stabilized by the Al proneness to combine with oxygen and form a μm layer of Al$_2$O$_3$ ensuring chemical passivation. In bulk, AlH$_3$ decomposes at 100–150 °C and the kinetics are reasonably fast, but the high H$_2$ pressure required to achieve reversibility (10 GPa, 600 °C, 24 h; 10 GPa at 25 °C or 6 GPa at 300–380 °C by other accounts are all very high pressures) remains a hard obstacle to overcome (Table 12). Even so, mitigation of this drawback has been attempted by means of nanoconfinement [40,44,51,109,125,203,206,216,226–233]. Some results are pure theoretical results concerning the catalytic activity of nano-AlH$_3$ [229] in the decomposition of 1,3,5,7-Tetranitro-1,3,5,7-tetrazocane, with simulated evolution of Al-clusters during the reaction [228], or decomposition of CH$_3$NO$_2$/nano-AlH$_3$ composite [232].

Table 12. Hydrogen storage features of nanosized AlH$_3$ materials.

Additive Used	Other H-Storing Source	H-Storing Composite	wt.% H$_2$	Obs.	Ref.
Al-doping (925 ppm), AC	AC@MOF (activated carbon@MOF)	Al@AC-MIL-101	0.55 (MIL-101) . . . 1.74 (Al@AC-MIL-101)	Al/α-AlH$_3$ hydrogenation release/uptake cycles ran at 298 K, and pressure < 100 bar H$_2$	[40]
HSAG (high surface area graphite)	-	AlH$_3$@HSAG	0.25 (14.4 wt.%AlH$_3$ by ICP-OES data, and only 15% of Al behaves reversibly)	H$_2$ uptake commences at 60 . . . 270 °C (mean 150 °C, peak 165 °C) and 60 bar H$_2$ pressure	[44]
CTF-bipyridine (CTF-bipy) AlH3@CTF-	-	AlH$_3$@CTF-bipyridine; AlH$_3$@CTF-biph—no reversibility (bipyridyl group was compulsory)	0.65, 0.58, 0.57 (2nd, 3rd, 4th cycles)	H$_2$ desorption between 95 . . . 154 °C rapidly (completes at 250 °C) from AlH$_3$@CTF-bipyridine composite. Reversible at 700 bar H$_2$ and 60 °C (incomplete, 24 h).	[51]
CNT	MgH$_2$	MgH$_2$/AlH$_3$@CNT	8.2 (1 h, 200 °C, dehydrogenation); 5.61 (0.16 h, 250 °C)	CNT prevent aggregation and enhance MgH$_2$-ALH$_3$ interaction	[109]
TiF$_3$	-	α-AlH$_3$/LiCl-TiF$_3$ (3:1:0.1 molar ratio)	9.92 (80–160 °C, 750 s)	α-AlH$_3$ obtained by milling of LiH and AlCl$_3$.	[203]
Li$_3$N	Li$_3$N	Li$_3$N@AlH$_3$	8.24 (100 °C); 6.18 (90 °C) and 5.75 (80 °C)	10 wt.% doping of AlH$_3$ with Li$_3$N leads to ~8.0 wt.% H$_2$ release at 100 °C. Nanoscale dispersion of the two hexagonal phases (AlH$_3$, Li$_3$N) by ball milling. E$_a$ = 100.4 kL mol^{-1} (0.9 AlH$_3$-0.1 Li$_3$N)	[206]
-	-	AlH$_3$	10.0 (140 °C, 3600 s)	neat AlH$_3$ (commercial)	[227]
Al(OH)$_3$	-	core-shell α-AlH$_3$@Al(OH)$_3$	10.0 (140 °C, 1000 s)	α-AlH$_3$@Al(OH)$_3$ nanocomposite can be stored in air (7 days)	[227]

The energetic bottleneck in hydrogenation of Al is the high activation barrier of H$_2$ dissociation over the Al surface, therefore catalysts have been employed to lower this barrier by using TM dopants like Sc, V, Ti or Nb [229].

The reaction of LiH and AlCl$_3$ was shown to be greatly sped up by using a 0.1 molar TiF$_3$, when the final product obtained after five hours milling under Ar pressure was a nanocomposite of composition α-AlH$_3$/LiCl-TiF$_3$ [203]. Duan et al., have shown the critical role of TiF3 that acted as a seed crystal for α-AlH$_3$. The pressure was also a crucial factor, as running the reaction under lower gas pressure only led to Al metal formation, without the envisioned hydridic phase (Equation (13)) [203].

$$3\,\text{LiH} + \text{AlCl}_3 \overset{\Delta}{\Rightarrow} 3\,\text{LiCl} + \text{Al} + \frac{3}{2}\text{H}_2 \uparrow \tag{13}$$
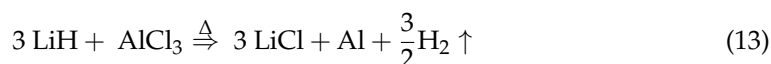
However, thermodynamic data showed a Gibbs free energy for the expected α-AlH$_3$ formation of $\Delta G = -269$ kJ mol^{-1}, therefore thermodynamically possible at 298 K [203]. Furthermore, tracking the reaction by solid-state ^{27}Al NMR spectra has shown the complex behavior of the reactive mixture (Figure 12) (Equation (14)).
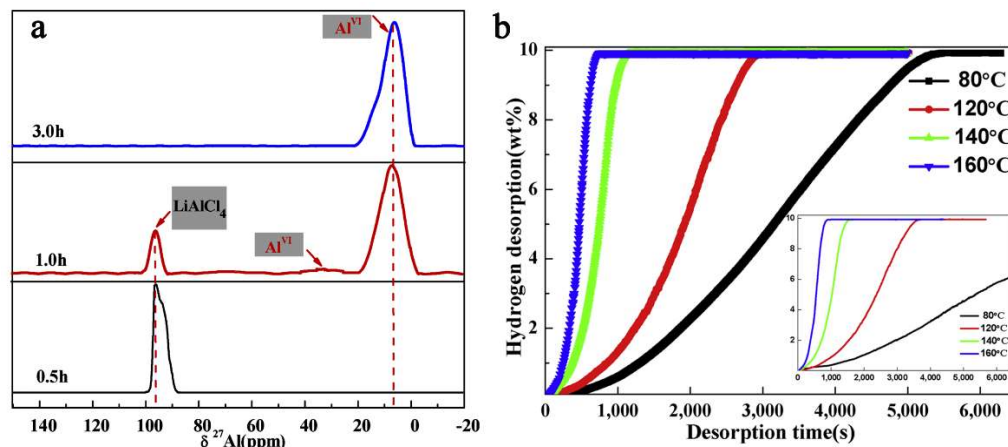
$$3LiH + AlCl_3 \Rightarrow LiAlCl_4 + AlH_x + 2LiCl \Rightarrow LiAlCl_{4-x}H_x + 2LiCl \Rightarrow 3LiCl + \alpha - AlH_3 \tag{14}$$

Figure 12. Solid state ^{27}Al NMR for reactive mixture LiH/AlCl$_3$/TiF$_3$ (3:1:0.1) after ball milling for 0.5 h, one hour and three hours (**a**); hydrogen desorption curve for final composite α-AlH$_3$/LiCl-TiF$_3$ at temperatures 80 °C, 120 °C, 140 °C and 160 °C (inset shown for α-AlH$_3$/LiCl without TiF$_3$ addition) (**b**). Reprinted/adapted with permission from Ref. [203]. 2019, Elsevier B.V.

The kinetics are vastly improved, and raising the temperature above 120 °C allows for complete dehydrogenation in roughly 10 min (Figure 12).

After five hours of ball milling under Ar pressure and dehydrogenation at 160 °C for 600 s, the final composite (Figure 13) shows nanosized AlH$_3$ (mean size of α-AlH$_3$ was 45 nm, without traces of agglomerates).
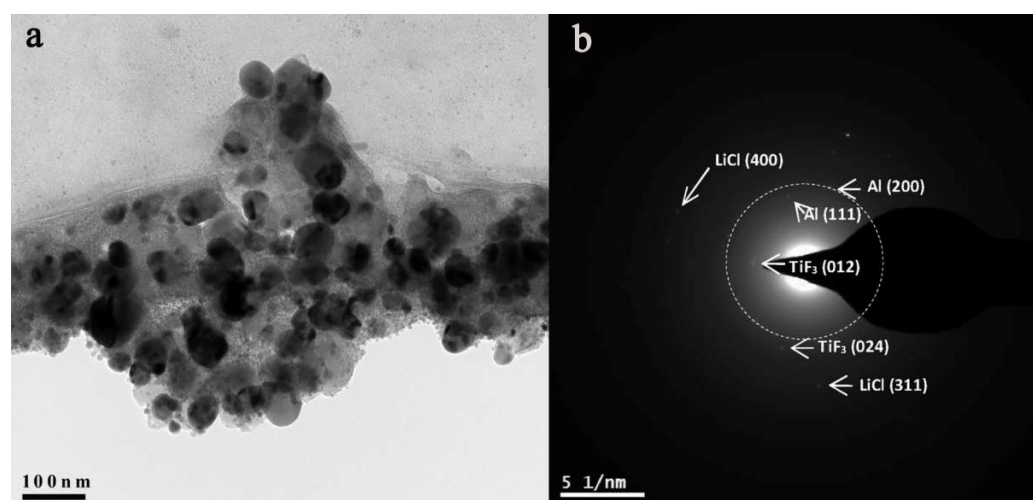
Figure 13. TEM image of α-AlH$_3$/LiCl-TiF$_3$ after dehydrogenation for 600 s at 160 °C (bright field TEM, (**a**); ED pattern, (**b**)). Reprinted/adapted with permission from Ref. [203]. 2019, Elsevier B.V.

The phase composition already shows formation of Al, consistent with the dehydrogenation reaction that had occurred. The report also highlighted the important role of the fluoride additive, as TiF$_3$ reduced E$_a$ of H-desorption to 52.1 kJ/mol [203].

Nanoconfinement of alane in a Cr-based MOF (MIL-101) with Al-doping has led to a nanocomposite able to store and recharge at 298 K (ambient) and 100 bar H$_2$, 17.4 mg

H_2/g (equivalent to 1.74 wt.% H_2) [40]. The introduction of alane inside the MIL-101 pores was made via solvent infiltration from a THF solution of AlH_3. In fact, the pristine MOF MIL-101 (3148 $m^2 g^{-1}$, 2.19 $cm^3 g^{-1}$ and 2.5–3 nm pores) was shown to store 0.55 wt.% H_2 under the same conditions. The hydrogen release profile from the investigated samples shows the improvement of nanoconfinement of AlH_3 in MOF pores over the hydrogen release performance (Figure 14) [40].
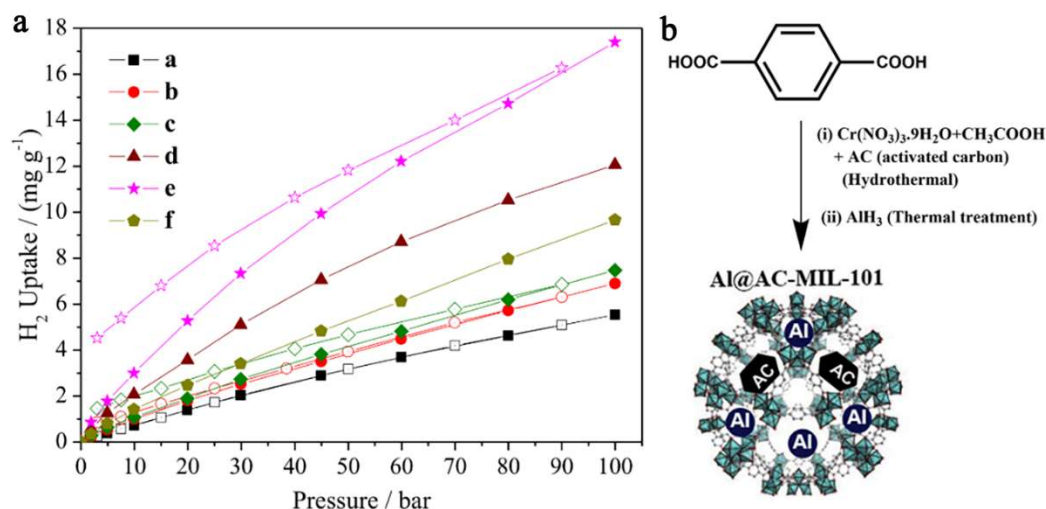
Figure 14. Hydrogen adsorption–desorption isotherms for (a) MIL-101; (b) AC-MIL-101; (c) AL@MIL-101; (d) Al@AC-MIL-101-A; (e) Al@AC-MIL-101-B; (f) Al@AC-MIL-101-C at 298K and pressures up to 100 bar H_2 (closed symbols-Adsorption; open symbols: Desorption) (**a**). AlH_3 introduction into MIL = 101 (**b**). Reprinted/adapted with permission from Ref. [40]. 2017, Elsevier Inc.

The gravimetric storage capacity (17.4 mg $H_2 g^{-1}$ composite) was rather low considering DOE's goals, due to the inability to increase Al-doping of the framework without crystallinity loss, and the role of AC additive became apparent in order to enhance hydrogen interaction with confined Al NPs [40].

In an attempt to improve upon previous results, Duan switched the nano-host to MWCNT (multi-walled carbon nanotubes) of high pore textural characteristics (550 $m^2 g^{-1}$, 6–8 nm diameter) and obtained by ball-milling $xMgH_2 + AlH_3$ (x = 1–4) nanocomposites MgH_2/AlH_3@CNT of crystal size 40–60 nm that released 8.2 wt.% H_2 at 200 °C (60 min), and recharged to 5.61 wt.% H_2 at 250 °C (10 min) (Figure 15) [109].
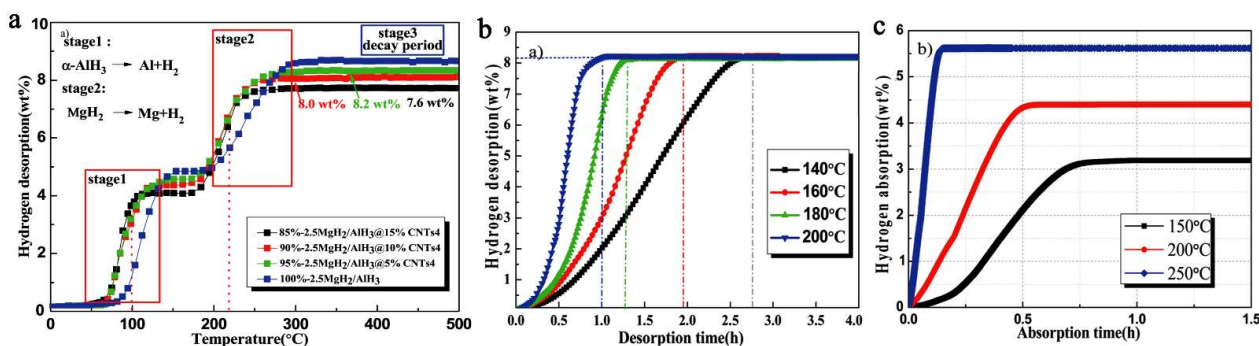
Figure 15. TPD (temperature programmed desorption) of 85%, 90% and 95%- $2.5MgH_2/AlH_3/CNTs4$ and 100%-$2.5MgH_2/AlH_3$ (ball milling, BPR 20:1, 200 rpm, 1 h) (**a**); dehydrogenation isotherm of 95%-$2.5MgH_2/AlH_3/CNTs4$ under 10^{-2} Pa pressure custom vacuum system (**b**); Isothermal rehydrogenation curves of 95%-$2.5MgH_2/AlH_3$@CNTs4 at different temperatures under 5 MPa H_2 pressure (**c**) [109]. Reprinted/adapted with permission from Ref. [109]. 2021, Royal Society of Chemistry.

The Al metal produced in the first dehydrogenation stage of the composite (Figure 16) will react with MgH_2 not yet dehydrogenated, to yield an intermetallic phase of $Al_{12}Mg_{17}$, which was confirmed by XRD data (Equation (15)).
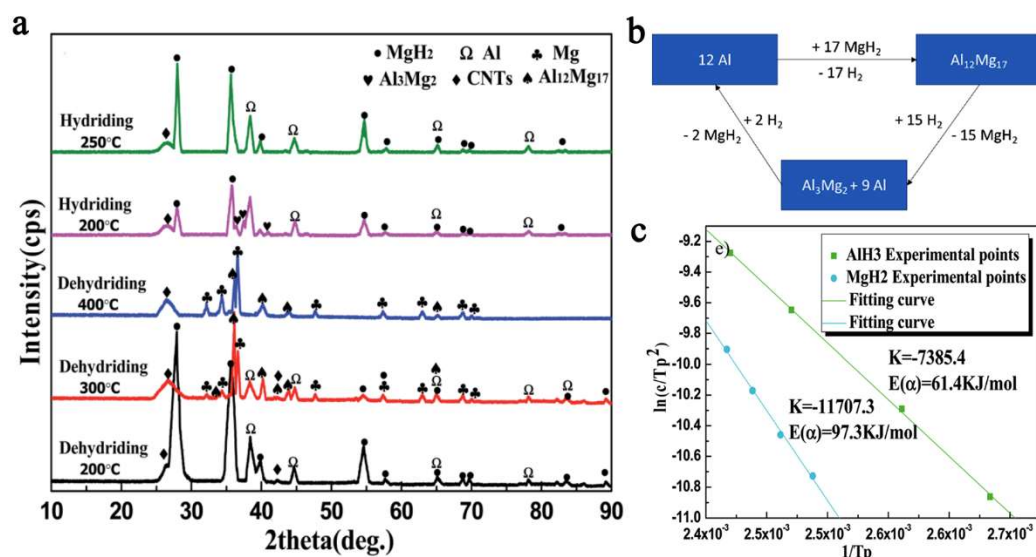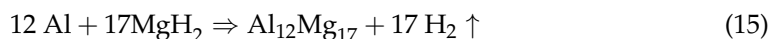
$$12\ Al + 17MgH_2 \Rightarrow Al_{12}Mg_{17} + 17\ H_2 \uparrow \tag{15}$$

Figure 16. XRD pattern for 95%- $2.5MgH_2/AlH_3/CNTs4$ after dehydrogenation at temperatures 200 . . . 400 °C (**a**); Al-tracking throughout the proposed mechanism, based on reaction data from ref. [109] (**b**) and Kissinger plot for deduction of E_a for hydrogenation of MgH_2 and AlH_3 (**c**) [109]. Reprinted/adapted with permission from Ref. [109]. 2021, Royal Society of Chemistry.

The reactions involved in the mechanistic proposal of the authors also allowed computation of the apparent activation energies (by Kissinger plot), which were of 97.3 kJ mol^{-1} for MgH_2 and 61.4 kJ mol^{-1} for AlH_3 (Figure 16c).

Wang et al., showed the potential of nanosizing by introducing (injection in HSAG of Et_2O solution of freshly-made AlH_3 from metathesis of $LiAlH_4$ and $AlCl_3$) [44]. Considering the 14 wt.% loading with AlH_3 in the composite AlH_3@HSAG (by ICP-OES), the expected hydrogen capacity was 1.4 wt.%. However, only 15% of the Al behaved reversibly and thus only an overall 0.25 wt.% storage could be attributed to the nanoconfined AlH_3 [44]. Interestingly, during sample preparation, the composite was heated at 65 °C under Ar to yield α-AlH_3 polymorph and minimize spontaneous decomposition of AlH_3 [44]. Either way, the reduction in dehydrogenation onset to ~60° (60 . . . 270 °C with a peak at 165 °C) shows the effect of nanosizing, effectively reducing hydrogen release by 50 °C [44].

Recently, using a triazine framework functionalized with bipyridine groups, CTF-bipy, a reversible behavior of alane in AlH_3@CTF-bipy nanocomposite was observed at 700 bar H_2 and 60 °C (although incomplete; Al signals still show in ^{27}Al MAS-NMR) (Figure 17) [51].

The EELS spectra of AlH_3@CTF-biph and AlH_3@CTF-bipy confirm that both contained aluminum, thus AlH_3 introduction in the CTF-based frame was achieved. However, inherent oxidation had also occurred so the Al_2O_3 presence was also recorded by EELS data [51]. Although alane introduction into CTF-biph and CTF-bipy porosity was confirmed by N_2 sorption isotherms (Figure 18), there was no reversibility in the case where CTF-biph was used as host [51].
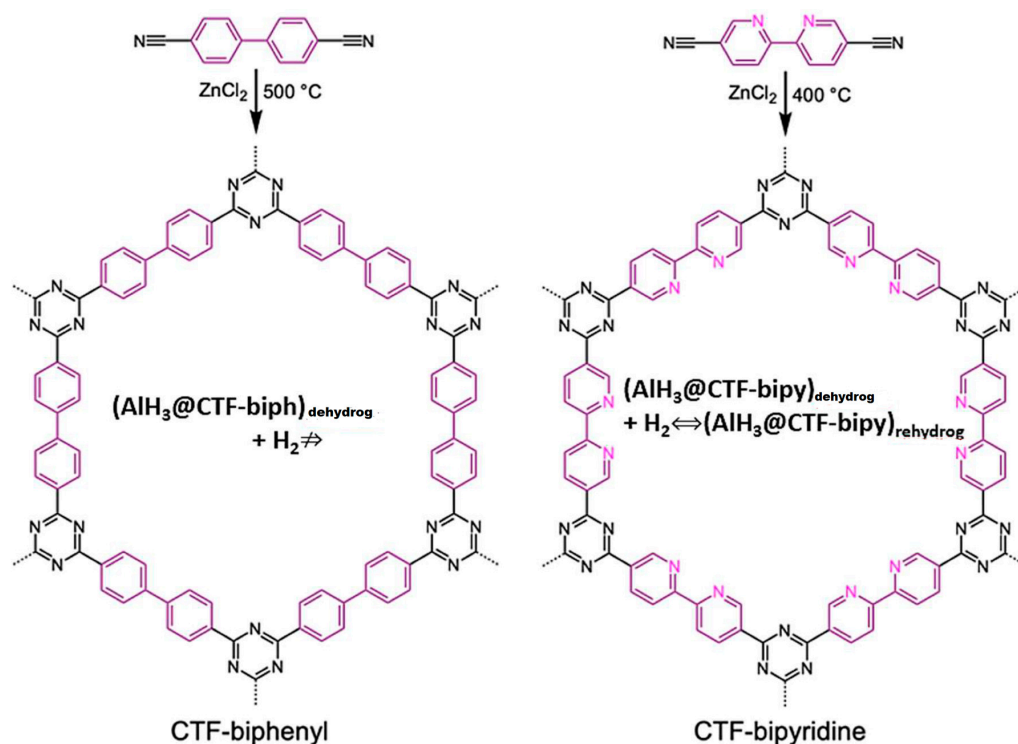
Figure 17. Construction of triazine-type CTF-biph and CTF-bipy used for alane nanoconfinement. Reversibility was only achieved for AlH_3@CTF-bipy, presumably due to Al-complexation to N-atoms of bipyridyl moieties (shown inside the CTF frame). Reprinted/adapted with permission from [51].
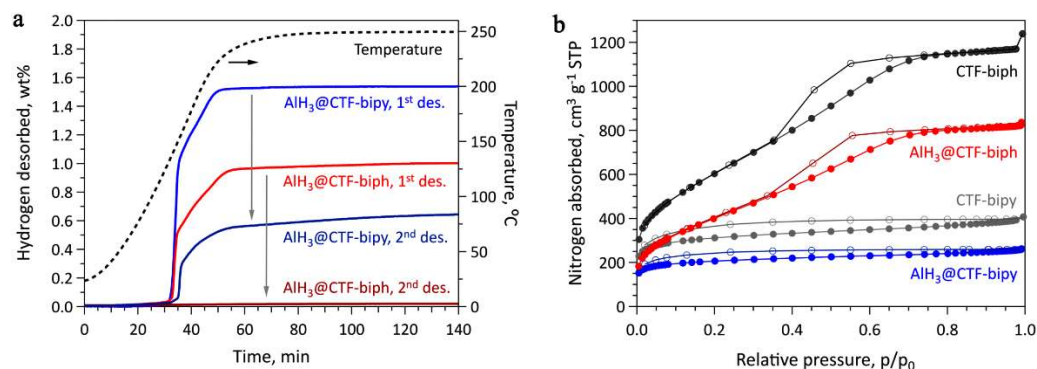

Figure 18. (**a**) Sievert data for CTF-based supported alane; (**b**) N_2 sorption isotherms at 77 K for CTF-biph, AlH_3@CTF-biph, CTF-bipy, and AlH_3@CTF-bipy. Reprinted/adapted with permission from Ref. [51]. 2021, Wiley-VCH GmbH.

Indeed, no reversibility was recorded in the absence of bipyridine groups (CTF-biph; biph = biphenyl), so the amino-functionality grafted on the covalent framework of the host was considered mandatory to achieve reversibility. This aspect was confirmed through DFT computations showing AlH_3 or higher clusters—$(AlH_3)_2$, $(AlH_3)_3$, or $(AlH_3)_4$—coordinating the 2 N-atoms of the bipyridine group. However, the reversible H_2 storage decreased from 1.44 wt.% (1st cycle) to 0.57 wt.% (4th cycle) [51].

Ball milling of a light metal nitride (Li_3N) with AlH_3 showed that a weakening of the Al-H bond is produced as a result of the milling process (a shift in XPS maximum), and that the hydrogen capacity decreases with the Li_3N fraction: 9.04 wt.% ($0.95AlH_3$-$0.05Li_3N$), 8.71 wt.% ($0.9AlH_3$-$0.1Li_3N$) and 7.85 wt.% ($0.85AlH_3$-$0.15Li_3N$), compared to the ball milled pure AlH_3 (9.86 wt.%) (Figure 19) [206].
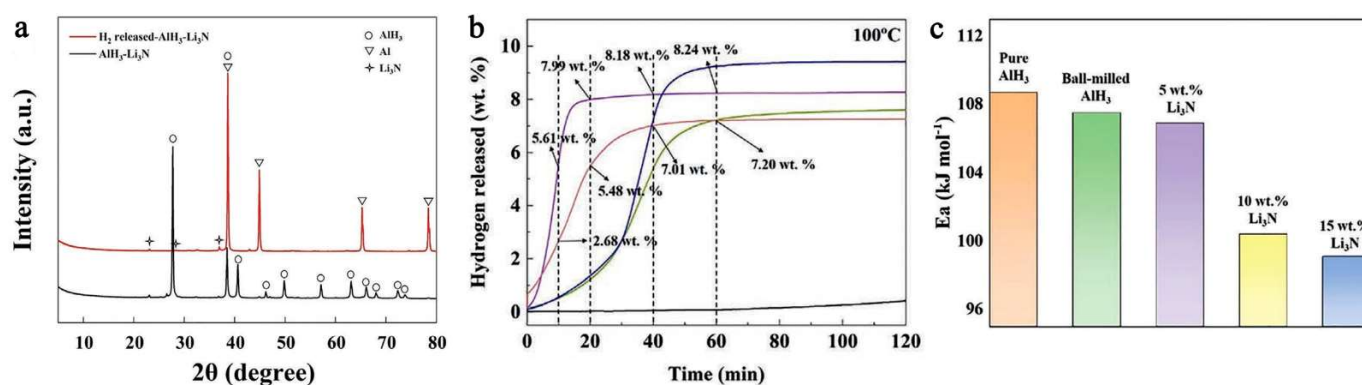
Figure 19. The XRD pattern $(0.9AlH_3\text{-}0.1Li_3N)_{dehydrog}$ (**a**), the hydrogen release profile under isothermal conditions (100 °C) of $(1 − x)AlH_3\text{-}xLi_3N$ (x = 0, 0.05, 0.1, 0.15) (**b**), and the calculated apparent activation energy (**c**). Reprinted/adapted with permission from Ref. [206]. 2022, Wiley-VCH GmbH.

Figure 19b shows the isothermal dehydrogenation of $(1 − x)AlH_3\text{-}xLi_3N$ (x = 0.05, 0.1, 0.15) at 100 °C, confirming a decrease in H_2 wt.% with the content of Li_3N. The XRD pattern confirms that the sole dehydrogenation product of the composite is metallic Al (Figure 19a). The onset of dehydrogenation was conveniently reduced to 66.8 °C ($0.95AlH_3\text{-}0.05Li_3N$), thus approaching an operating regime suitable for FCEs. The beneficial role of lithium amide was confirmed by the apparent E_a which is strongly reduced (Figure 19c) [206].

6.4. TM-Hydrides

While main group metal hydrides are attractive due to metal abundance and low atomic weight of the metal (so higher wt.% H_2 storage capacity), some TM (transition metals) have also been recently investigated by employing nanosizing effects (Table 13) [79,97,169,200,212,216,234]. The simplest and most classical model system to study TM-H interaction is the Pd-H system [200,234]. While the gravimetric storage capacity is too low for it to be considered for vehicular applications, the nature of Pd . . . H interaction has shed new light on thermodynamic predictions in Pd NPs forming PdH_x, estimating cluster expansion, phase boundaries Pd/Pd . . . H, phase transitions (>400 K) and interfacial free energies by using DFT method [200,234]. Pd is often thought of as being able to absorb H_2 like a sponge, reversibly absorbing more than 1000 times its own volume. In short, interaction of H_2 with palladium comprises of H-H dissociation in atomic [H], diffusion of [H] into Pd_{bulk}, where it occupies the free interstitial sites in *fcc* lattice of Pd, forming either an α-phase PdH_x (x < 0.03, rt) or the hydridic β-phase PdH_x (x > 0.03) [200]. The catalytic role of Ph-hydride has been recently harnessed in a complex Pd hydride $CaPdH_2$, for semi-hydrogenation of $C_nH_{2n−2}$ (alkynes) to C_nH_{2n} (alkenes) [79].

Rizo-Acosta et al., have addressed the issue of Mg/MgH_2 slow kinetics by the addition of ETM (early transition metals: ETM = Sc, Y, Ti, Zr, V, Nb) to nanostructured MgH_2 in a one-pot, mechanochemical reaction [169]. The influence of the milling time (0 . . . 120 min) over hydrogen wt.% storage capacity (Figure 20a) and absorption rate (Figure 20b) at 573 K has been studied and reveals that using 0.95 MgH_2 –0.05 VH_2, a 7.3 wt.% hydrogen uptake is registered, even higher than the experimental value for MgH_2 (7.6 wt.% theoretical, 7.1 wt.% experimental) [169]. Moreover, the absorption rate is the fastest for 0.95 MgH_2 –0.05 TiH_2, with a shoulder in the sigmoidal shape due to $(ETM)H_x$ formation, and varies in the order Y < V < Ti < Nb < Sc < Zr (Figure 20b). These hydrides (ScH_2, YH_3, TiH_2, ZrH_2, VH, NbH) are stable under experimental hydrogenation conditions and have a crystal size of ~10 nm, acting as effective catalysts for dehydrogenation (recombination of H atoms) and rehydrogenation (MgH_2 nucleation due to $MgH_2/(ETM)H_x$ interface energies).

Table 13. Hydrogen storage features of nanosized (TM) H_x materials.

Additive Used	Other H-Storing Souce	H-Storing Composite	wt.% H_2	Obs.	Ref.
porous carbon (HSAG)	Co	Mg_2CoH_5@HSAG $Co + MgH_2$@HSAG	N/A	bottom-up approach affords PSD 2–50 nm (max. at 15 nm); wt.% H_2 capacity decrease due to Mg oxidation. $2MgH_2 + Co + \frac{1}{2}H_2 \rightarrow Mg_2CoH_5$ MgH_2 NPs: 5nm. Co@Mg NPs: 7 nm. Desorption temperature increases with cycle number (1..7) in a 5 wt.% Mg_2CoH_5@HSAG nanocomposite from ~590 to ~610 K. Possible disproportionation: $Mg_2CoH_5 \rightarrow MgH_2 + Mg_6Co_2H_{11}$	[97]
ScH_2, YH_3, TiH_2, ZrH_2, VH and NbH	MgH_2	$0.95 MgH_2$–0.05 (TM)H_x	$\geq$5 wt.%	(TM)H_x crystallite size of ~10 nm, obtained by mechanochemistry (RMB, reactive ball milling) MgH_2 + TM (Sc, Y, Ti, Zr, V, Nb) under H_2 pressure. Early Transition Metals (ETM) chosen by the known stability of their respective hydrides under normal conditions.	[169]
MOF	Ir, Rh	TM-H@MOF (TM = Pd, Ir, Rh)	0.18H/Pd (cubes); 0.27H/Pd (octahedrons)	ΔH_{abs} of the TM NPs change from endothermic to exothermic with decreasing particle size. Pd@HKUST-1 [copper(II) 1,3,5-benzenetricarboxylate $(Cu_3(BTC)_2)$] abs. 0.87H/Pd compared to Pd(bulk, cubes, 0.5 H/Pd)	[200,234]
Mg nanofilm	Mg	Pd NPs@Mg film	N/A	$D_H^{film} \approx 8 \times 10^{-18}$ m^2 s^{-1}	[212]
-	-	TaH$_x$ (0 < x < 0.7)	<0.389 wt.%	higher H-sensing activity than Pd-alloy ($10^{-2} \ldots 10^{+4}$ Pa H_2)	[216]
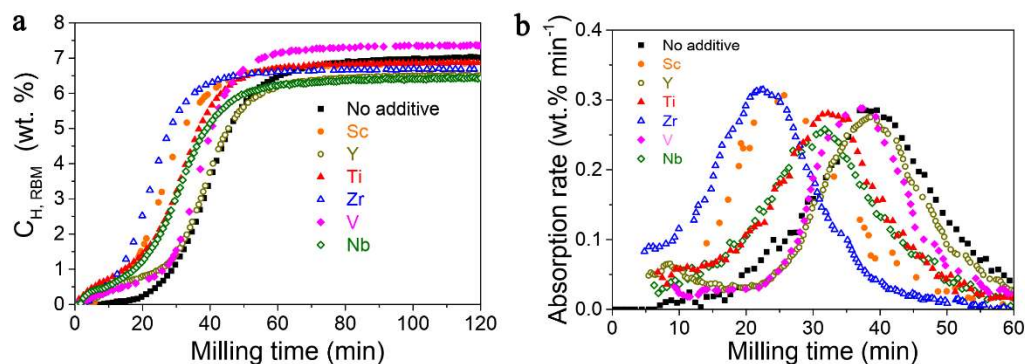
Figure 20. (**a**) Hydrogen uptake curves for $0.95 MgH_2$–0.05 (ETM)H_x during reactive ball milling; (**b**) absorption rate as derivative of hydrogen uptake curves. Reprinted/adapted with permission from Ref. [169]. 2019, Royal Society of Chemistry.

Notably, the reductive synthesis (300 °C, 7.89 atm H_2) yields stabilization of the lower oxidation states of ETM, and mostly (ETM)H_2 are produced, except for YH_3 which affords the slowest desorption rate (0.06 wt.% min^{-1}, 1 wt.% hydrogen release in 15 min under 0.296 atm H_2). The best result was obtained for $0.95 MgH_2$–0.05 VH, when 6.1 wt.% (90% of the maximum) hydrogen was desorbed in 15 min (Figure 21) [169].
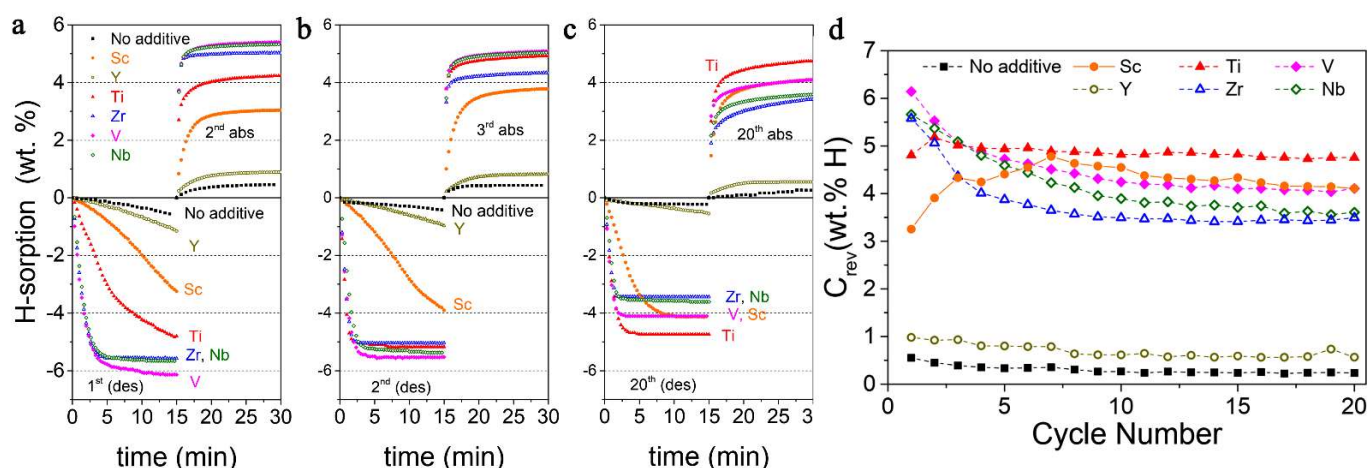
Figure 21. Hydrogen sorption curves recorded during the 2nd (**a**), 3rd (**b**) and 20th (**c**) absorption cycle for as-synthesized nanocomposites. Evolution of reversible hydrogen storing capacity with number of cycles (**d**). Reprinted/adapted with permission from Ref. [169]. 2019, Royal Society of Chemistry.

The most stable reversible capacity during cycling was achieved for 0.95 MgH$_2$−0.05 TiH$_2$ nanocomposite, which shows fast kinetics and does not fall below 4.8 wt.% even after 20 cycles (Figure 21). Additionally, no Mg-ETM-H ternary phases were observed [169].

A series of notable advances have been observed for complex hydrides as well, although their details are beyond the scope of this review. In short, metal tetrahydridoaluminates/alanates [14,51]: LiAlH$_4$ [54,81,96,99,101,111,113,135,166,178], NaAlH$_4$ [33,45,50,69, 74,82,127–129,167,214,234,235], tetrahydridoborates/borohydrides [3,12,14,42]: LiBH$_4$ [42, 45,47,54,56,70,78,81,87,89,91,93,99,100,104,106,108,120,123,130,134,135,161,216,230,231,236–240], NaBH$_4$ [49,74,216,236,241], Mg(BH$_4$)$_2$ [42,55,61,70,105,126,132,151,159,207,216,220,224,236, 242,243], Ca(BH$_4$)$_2$ [116,216,236,243] and (TM)(BH$_4$)$_x$ [150,216], ammonia-borane NH$_3$BH$_3$ [36, 38,63,64,75,85,86,88,90,139–144,153,154,156,162,171,175,197,213,244–249] and RCH reactive hydride composites [45,54,78,91,99,130,134,173,215,240,250] have been recently explored and improved thermodynamic and/or kinetic parameters have been reported [107,145,226,251–253].

7. Conclusions and Outlook

The urgency of a green, renewable and sustainable fuel to replace fossil fuels is more stringent today than ever. The metal hydrides constitute materials that possess intrinsically high gravimetric and volumetric hydrogen storage capacities, but their sluggish kinetics and poor thermodynamics still constitute an obstacle for the wide acceptance of their use in the fuel of the future. However, various strategies have been recently explored, and perhaps the most returns derive from basic shifts in thinking: oriented growth of MgH$_2$ on catalytically active substrates; size-reduction in metal hydrides to few nm when thermodynamic destabilization works best; or usage of new class of catalysts of 2D-structure (MXenes)—they have all showed unexpectedly good results. There is clearly room for improvement in the fascinating field of metal hydrides, and research efforts ought to concentrate on improving nanoparticle system design, careful consideration of the incorporating matrix and selected hydrogenation/dehydrogenation catalysts, from both an economic and a feasibility point of view. Given the raw material scarcity but also reactivity and particular characteristics of some complex hydrides (like volatility of Al(BH$_4$)$_3$, or extreme toxicity of Be(BH$_4$)$_2$ etc.), the optimal hydrogen storage material will likely be based on magnesium nanoconfined in a carbonaceous host and/or catalyzed by Ti-based catalysts (such as TiO$_2$, TiO, or MXenes). The realistic application of metal hydride systems is conditioned by a number of factors: (i) the discovery of a material that displays a reliably-reversible behavior in hydrogenation studies; (ii) consistent performance across hundreds of H$_2$-absorption/desorption cycles; (iii) lower activation energies and consequently faster

absorption/desorption kinetics and improved thermodynamics; (iv) consistently fast kinetics for fast refueling; (v) thermodynamic stability and material integrity to afford safe storage in a fuel tank; (vi) reasonable resistance to air and/or moisture; (vii) synthesis route moderately easy and preferably comprising of few steps; (viii) access to sufficient raw materials and limit amount of CRM (critical raw materials) used; (ix) reliable scaling-up of the lab demonstrator to a multi-KW tank capable to drive a vehicle for 500 km or more; (x) strong safety precautions and technological parameters implementation to afford a tank capable to store, release and withstand high H_2 pressures (of more than 100 atm). Within this framework, the EU directives to limit CRM usage is expected to drive the research towards more-abundant metal sources such as Mg or Al (Mg was also included in the list of CRM from 2020, although currently it can be obtained in enough quantities). Noble metal catalysis (like Pd) will probably not become a commercial way of speeding up hydrogen delivery or the recharging of hydride-based fuels due to the associated cost. Other catalysts like MXenes can be produced on a larger scale, but the Ti-based material could also face soon shortages.

Nanoconfinement still offers general improvements across the board for hydride-based materials, but the choice of host is limited—among the classes of hosts presented in the current review, the most promising are carbonaceous frameworks and MOFs. Carbon-based materials can be tailored morphologically for hydride inclusion, and their cost is modest; however, this must be considered with care since a zero-carbon policy might imply soon that carbon should not be used as a host any longer. Even though it releases no CO_2 in the atmosphere; there will be an associated cost with treatment of the end-of-life C-based fuel, and so the carbon footprint will not be negligible.

Considering these material, performance, safety and cost restrictions, the final choice for a viable, sustainable hydride-based material is a delicate one and only validation through a scaling-up proven in an operational environment could confirm whether it can be used on a large-scale tank for vehicular applications and afterwards adopted by industry. The ultimate goal is, without a doubt, to approach as much as possible the reversible, theoretical hydrogen capacity, and this is a joint venture of all the above considerations.

Institutional Review Board Statement: Not applicable.

Informed Consent Statement: Not applicable.

Data Availability Statement: Not applicable.

Conflicts of Interest: The authors declare no conflict of interest.

References

1. Agarwal, A.K.; Martínez, A.G.; Kalwar, A.; Valera, H. *Energy, Environment, and Sustainability—Advanced Combustion for Sustainable Transport*; Springer Nature: Singapore, 2022; pp. 299–330. [CrossRef]
2. Černý, R.; Brighi, F.M.M. Metal hydroborates: From hydrogen stores to solid electrolytes. *J. Alloys Compd.* **2022**, *895*, 162659. [CrossRef]
3. He, T.; Cao, H.; Chen, P. Complex Hydrides for Energy Storage, Conversion, and Utilization. *Adv. Mater.* **2019**, *31*, 1902757. [CrossRef] [PubMed]
4. Schneemann, A.; White, J.L.; Kang, S.Y.; Jeong, S.; Wan, L.F.; Cho, E.S.; Heo, T.W.; Prendergast, D.; Urban, J.J.; Wood, B.C.; et al. Nanostructured Metal Hydrides for Hydrogen Storage. *Chem. Rev.* **2018**, *118*, 10775–10839. [CrossRef] [PubMed]
5. US DOE Target Explanation Document: Onboard Hydrogen Storage for Light-Duty Fuel Cell Vehicles. Available online: https://www.energy.gov/eere/fuelcells/downloads/target-explanation-document-onboard-hydrogen-storage-light-duty-fuel-cell (accessed on 10 May 2022).

6.   US DOE Hydrogen & Fuel Cells Program. Available online: https://www.hydrogen.energy.gov/ (accessed on 10 May 2022).

7.   Shen, H.; Li, H.; Yang, Z.; Li, C. Magic of hydrogen spillover: Understanding and application. *Green Energy Environ.* **2022**. [CrossRef]

8.   Hirscher, M.; Yartys, V.A.; Baricco, M.; von Colbe, J.B.; Blanchard, D.; Bowman, R.C.; Broom, D.P.; Buckley, C.E.; Chang, F.; Chen, P.; et al. Materials for hydrogen-based energy storage—Past, recent progress and future outlook. *J. Alloys Compd.* **2020**, *827*, 153548. [CrossRef]

9.   Lai, Q.; Sun, Y.; Wang, T.; Modi, P.; Cazorla, C.; Demirci, U.B.; Fernandez, J.R.A.; Leardini, F.; Aguey-Zinsou, K.-F. How to Design Hydrogen Storage Materials? Fundamentals, Synthesis, and Storage Tanks. *Adv. Sustain. Syst.* **2019**, *3*, 1900043. [CrossRef]

10.   Abe, J.O.; Popoola, A.P.I.; Ajenifuja, E.; Popoola, O.M. Hydrogen energy, economy and storage: Review and recommendation. *Int. J. Hydrogen Energy* **2019**, *44*, 15072–15086. [CrossRef]

11.   Kumar, R.; Karkamkar, A.; Bowden, M.; Autrey, T. Solid-state hydrogen rich boron–nitrogen compounds for energy storage. *Chem. Soc. Rev.* **2019**, *48*, 5350–5380. [CrossRef]

12.   Hagemann, H. Boron Hydrogen Compounds: Hydrogen Storage and Battery Applications. *Molecules* **2021**, *26*, 7425. [CrossRef]

13.   Lee, S.-Y.; Lee, J.-H.; Kim, Y.-H.; Kim, J.-W.; Lee, K.-J.; Park, S.-J. Recent Progress Using Solid-State Materials for Hydrogen Storage: A Short Review. *Processes* **2022**, *10*, 304. [CrossRef]

14.   Hadjixenophontos, E.; Dematteis, E.M.; Berti, N.; Wołczyk, A.R.; Huen, P.; Brighi, M.; Le, T.T.; Santoru, A.; Payandeh, S.; Peru, F.; et al. A Review of the MSCA ITN ECOSTORE—Novel Complex Metal Hydrides for Efficient and Compact Storage of Renewable Energy as Hydrogen and Electricity. *Inorganics* **2020**, *8*, 17. [CrossRef]

15.   Broom, D.P.; Hirscher, M. Improving Reproducibility in Hydrogen Storage Material Research. *ChemPhysChem* **2021**, *22*, 2141–2157. [CrossRef] [PubMed]

16.   Comanescu, C. Complex Metal Borohydrides: From Laboratory Oddities to Prime Candidates in Energy Storage Applications. *Materials* **2022**, *15*, 2286. [CrossRef]

17.   Kharbachi, A.E.; Dematteis, E.M.; Shinzato, K.; Stevenson, S.C.; Bannenberg, L.J.; Heere, M.; Zlotea, C.; Szilágyi, P.Á.; Bonnet, J.-P.; Grochala, W.; et al. Metal Hydrides and Related Materials. Energy Carriers for Novel Hydrogen and Electrochemical Storage. *J. Phys. Chem. C* **2020**, *124*, 7599–7607. [CrossRef]

18.   Zheng, J.; Wang, C.-G.; Zhou, H.; Ye, E.; Xu, J.; Li, Z.; Loh, X.J. Current Research Trends and Perspectives on Solid-State Nanomaterials in Hydrogen Storage. *AAAS Res.* **2021**, *2021*, 3750689. [CrossRef] [PubMed]

19.   He, T.; Cao, H.; Chen, P. The Roles of Alkali/Alkaline Earth Metals in the Materials Design and Development for Hydrogen Storage. *Acc. Mater. Res.* **2021**, *2*, 726–738. [CrossRef]

20.   Huang, Y.; An, C.; Zhang, Q.; Zang, L.; Shao, H.; Liu, Y.; Zhang, Y.; Yuan, H.; Wang, C.; Wang, Y. Cost-effective Mechanochemical Synthesis of Highly Dispersed Supported Transition Metal Catalysts for Hydrogen Storage. *Nano Energy* **2021**, *80*, 105535. [CrossRef]

21.   Li, Z.; Wei, B. Topological materials and topologically engineered materials: Properties, synthesis, and applications for energy conversion and storage. *J. Mater. Chem. A* **2021**, *9*, 1297–1313. [CrossRef]

22.   Wood, B.C.; Heo, T.W.; Kang, S.Y.; Wan, L.F.; Li, S. Beyond Idealized Models of Nanoscale Metal Hydrides for Hydrogen Storage. *Ind. Eng. Chem. Res.* **2020**, *59*, 5786–5796. [CrossRef]

23.   Callini, E.; Atakli, Z.Ö.K.; Hauback, B.C.; Orimo, S.-i.; Jensen, C.; Dornheim, M.; Grant, D.; Cho, Y.W.; Chen, P.; Hjorvarsson, B.; et al. Complex and liquid hydrides for energy storage. *Appl. Phys. A* **2016**, *122*, 353. [CrossRef]

24.   Milanese, C.; Jensen, T.R.; Hauback, B.C.; Pistidda, C.; Dornheim, M.; Yang, H.; Lombardo, L.; Zuettel, A.; Filinchuk, Y.; Ngene, P.; et al. Complex hydrides for energy storage. *Int. J. Hydrogen Energy* **2019**, *44*, 7860–7874. [CrossRef]

25.   Ngene, P.; Longo, A.; Mooij, L.; Bras, W.; Dam, B. Metal-hydrogen systems with an exceptionally large and tunable thermodynamic destabilization. *Nat. Commun.* **2017**, *8*, 1846. [CrossRef] [PubMed]

26.   Huot, J.; Cuevas, F.; Deledda, S.; Edalati, K.; Filinchuk, Y.; Grosdidier, T.; Hauback, B.C.; Heere, M.; Jensen, T.R.; Latroche, M.; et al. Mechanochemistry of Metal Hydrides: Recent Advances. *Materials* **2019**, *12*, 2778. [CrossRef] [PubMed]

27.   Witman, M.; Ling, S.; Grant, D.M.; Walker, G.S.; Agarwal, S.; Stavila, V.; Allendorf, M.D. Extracting an Empirical Intermetallic Hydride Design Principle from Limited Data via Interpretable Machine Learning. *J. Phys. Chem. Lett.* **2020**, *11*, 40–47. [CrossRef]

28.   Liu, Y.; Li, H.W.; Huang, Z. Editorial: Metal Hydride-Based Energy Storage and Conversion Materials. *Front. Chem.* **2020**, *8*, 675. [CrossRef]

29.   Andersson, J.; Gronkvist, S. Large-scale storage of hydrogen. *Int. J. Hydrogen Energy* **2019**, *44*, 11901–11919. [CrossRef]

30.   Kweon, J.J.; Kim, H.-I.; Lee, S.-h.; Kim, J.; Lee, S.K. Quantitative probing of hydrogen environments in quasicrystals by high-resolution NMR spectroscopy. *Acta Mater.* **2022**, *226*, 117657. [CrossRef]

31.   Misaki, T.; Oikawa, I.; Takamura, H. Negative Knight Shift in Ba-Ti Oxyhydride: An Indication of the Multiple Hydrogen Occupation. *Chem. Mater.* **2019**, *31*, 18–7178. [CrossRef]

32.   Liu, Y.-S.; Jeong, S.; White, J.; Feng, X.; Cho, E.S.; Stavila, V.; Allendorf, M.; Urban, J.; Guo, J. In-situ/operando X-ray characterization of metal hydrides. *ChemPhysChem* **2019**, *20*, 1261–1271. [CrossRef]

33.   NaraseGowda, S.; Brown, C.M.; Tyagi, M.; Jenkins, T.; Dobbins, T.A. Quasi-Elastic Neutron Scattering Studies of Hydrogen Dynamics for Nanoconfined $NaAlH_4$. *J. Phys. Chem. C* **2016**, *120*, 14863–14873. [CrossRef]

34. Zhou, C.; Gao, Y.; Bowman, R.C., Jr.; Zhang, J.; Liu, H.; Sun, P.; Fang, Z.Z. A high throughput dynamic method for characterizing thermodynamic properties of catalyzed magnesium hydrides by thermogravimetric analysis. *Phys. Chem. Chem. Phys.* **2021**, *23*, 15374. [CrossRef] [PubMed]

35. Luong, H.M.; Pham, M.T.; Guin, T.; Madhogaria, R.P.; Phan, M.-H.; Larsen, G.K.; Nguyen, T.D. Sub-second and ppm-level optical sensing of hydrogen using templated control of nano-hydride geometry and composition. *Nat. Commun.* **2021**, *12*, 2414. [CrossRef] [PubMed]

36. Valero-Pedraza, M.J.; Gascón, V.; Carreón, M.A.; Leardini, F.; Ares, J.R.; Martín, Á.; Sánchez-Sánchez, M.; Bañares, M.A. *Operando* Raman-mass spectrometry investigation of hydrogen release by thermolysis of ammonia borane confined in mesoporous materials. *Microporous Mesoporous Mater.* **2016**, *226*, 454–465. [CrossRef]

37. Surrey, A.; Nielsch, K.; Rellinghaus, B. Comments on "Evidence of the hydrogen release mechanism in bulk MgH$_2$". *Sci. Rep.* **2017**, *7*, 44216. [CrossRef]

38. Petit, J.-F.; Demirci, U.B. Discrepancy in the thermal decomposition/dehydrogenation of ammonia borane screened by thermogravimetric analysis. *Int. J. Hydrogen Energy* **2019**, *44*, 14201–14206. [CrossRef]

39. Wu, Y.-J.; Wang, C.-Y. Insight into the Catalytic Effects of Open Metal Sites in Metal−Organic Frameworks on Hydride Dehydrogenation via Nanoconfinement. *ACS Sustain. Chem. Eng.* **2019**, *7*, 16013–16025. [CrossRef]

40. Prabhakaran, P.K.; Catoire, L.; Deschamps, J. Aluminium doping composite metal-organic framework by alane nanoconfinement: Impact on the room temperature hydrogen uptake. *Microporous Mesoporous Mater.* **2017**, *243*, 214–220. [CrossRef]

41. Pukazhselvan, D.; Sandhya, K.S.; Fagg, D.P. 5—Nanostructured advanced materials for hydrogen storage. In *Nanomaterials for Sustainable Energy and Environmental Remediation—Materials Today*; Elsevier: Amsterdam, The Netherlands, 2020; pp. 97–163. [CrossRef]

42. Lai, Q.; Yang, Y.; Aguey-Zinsou, K.-F. Nanoconfinement of borohydrides in hollow carbon spheres: Melt infiltration versus solvent impregnation for enhanced hydrogen storage. *Int. J. Hydrogen Energy* **2019**, *44*, 23225–23238. [CrossRef]

43. Zhang, J.; Yan, S.; Qu, H. Recent progress in magnesium hydride modified through catalysis and nanoconfinement. *Int. J. Hydrogen Energy* **2018**, *43*, 1545–1565. [CrossRef]

44. Wang, L.; Rawal, A.; Aguey-Zinsou, K.-F. Hydrogen storage properties of nanoconfined aluminium hydride (AlH$_3$). *Chem. Eng. Sci.* **2019**, *194*, 64–70. [CrossRef]

45. Javadian, P.; Sheppard, D.A.; Buckley, C.E.; Jensen, T.R. Hydrogen Desorption Properties of Bulk and Nanoconfined LiBH$_4$-NaAlH$_4$. *Crystals* **2016**, *6*, 70. [CrossRef]

46. Rueda, M.; Sanz-Moral, L.M.; Martín, Á. Innovative methods to enhance the properties of solid hydrogen storage materials based on hydrides through nanoconfinement: A review. *J. Supercrit. Fluids* **2018**, *141*, 198–217. [CrossRef]

47. Le, T.T.; Pistidda, C.; Nguyen, V.H.; Singh, P.; Raizada, P.; Klassen, T.; Dornheim, M. Nanoconfinement effects on hydrogen storage properties of MgH$_2$ and LiBH$_4$. *Int. J. Hydrogen Energy* **2021**, *46*, 23723–23736. [CrossRef]

48. Zhang, S.; Hedtke, T.; Zhou, X.; Elimelech, M.; Kim, J.-H. Environmental Applications of Engineered Materials with Nanoconfinement. *ACS EST Eng.* **2021**, *1*, 706–724. [CrossRef]

49. Salman, M.S.; Rawal, A.; Aguey-Zinsou, K.-F. Tunable NaBH$_4$ Nanostructures Revealing Structure-Dependent Hydrogen Release. *Adv. Energy Sustain. Res.* **2021**, *2*, 2100063. [CrossRef]

50. Chen, W.; You, L.; Xia, G.; Yu, X. A balance between catalysis and nanoconfinement towards enhanced hydrogen storage performance of NaAlH$_4$. *J. Mater. Sci. Technol.* **2021**, *79*, 205–211. [CrossRef]

51. Stavila, V.; Li, S.; Dun, C.; Marple, M.A.T.; Mason, H.E.; Snider, J.L.; Reynolds III, J.E.; Gabaly, F.E.; Sugar, J.D.; Spataru, C.D.; et al. Defying Thermodynamics: Stabilization of Alane Within Covalent Triazine Frameworks for Reversible Hydrogen Storage. *Angew. Chem. Int. Ed.* **2021**, *60*, 25815–25824. [CrossRef]

52. Goh, P.S.; Ismail, A.F. Nanocomposites for Environmental and Energy Applications. *Nanomaterials* **2021**, *11*, 345. [CrossRef]

53. Huen, P.; Paskevicius, M.; Richter, B.; Ravnsbæk, D.B.; Jensen, T.R. Hydrogen Storage Stability of Nanoconfined MgH$_2$ upon Cycling. *Inorganics* **2017**, *5*, 57. [CrossRef]

54. Wood, B.C.; Stavila, V.; Poonyayant, N.; Heo, T.W.; Ray, K.G.; Klebanoff, L.E.; Udovic, T.J.; Lee, J.R.I.; Angboonpong, N.; Sugar, J.D.; et al. Nanointerface-Driven Reversible Hydrogen Storage in the Nanoconfined Li–N–H System. *Adv. Mater. Interfaces* **2017**, *4*, 1600803. [CrossRef]

55. Liu, Y.-S.; Ray, K.G.; Jørgensen, M.; Mattox, T.M.; Cowgill, D.F.; Eshelman, H.V.; Sawvel, A.M.; Snider, J.L.; York, W.; Wijeratne, P.; et al. Nanoscale Mg–B via Surfactant Ball Milling of MgB$_2$: Morphology, Composition, and Improved Hydrogen Storage Properties. *J. Phys. Chem. C* **2020**, *124*, 21761–21771. [CrossRef]

56. Das, S.; Ngene, P.; Norby, P.; Vegge, T.; de Jongh, P.E.; Blanchard, D. All-Solid-State Lithium-Sulfur Battery Based on a Nanoconfined LiBH$_4$ Electrolyte. *J. Electrochem. Soc.* **2016**, *163*, A2029–A2034. [CrossRef]

57. Zhang, X.L.; Liu, Y.F.; Zhang, X.; Hu, J.J.; Gao, M.X.; Pan, H.G. Empowering hydrogen storage performance of MgH$_2$ by nanoengineering and nanocatalysis. *Mater. Today Nano* **2020**, *9*, 100064. [CrossRef]

58. Rabkin, E.; Skripnyuk, V.; Estrin, Y. Ultrafine-Grained Magnesium Alloys for Hydrogen Storage Obtained by Severe Plastic Deformation. *Front. Mater.* **2019**, *6*, 240. [CrossRef]

59. Stavila, V.; Klebanoff, L.E. Nanostructured Metal Amides and Nitrides for Hydrogen Storage. U.S. Patent No. US10000377B1, 19 June 2018. Available online: https://patents.google.com/patent/US10000377B1/en (accessed on 16 May 2022).

60. Li, L.; Huang, Y.; An, C.; Wang, Y. Lightweight hydrides nanocomposites for hydrogen storage: Challenges, progress and prospects. *Sci. China Mater.* **2019**, *62*, 1597–1625. [CrossRef]

61. Sun, Y.; Shen, C.; Lai, Q.; Liu, W.; Wang, D.-W.; Aguey-Zinsou, K.-F. Tailoring magnesium based materials for hydrogen storage through synthesis: Current state of the art. *Energy Storage Mater.* **2018**, *10*, 168–198. [CrossRef]

62. Callini, E.; Aguey-Zinsou, K.-F.; Ahuja, R.; Ares, J.R.; Bals, S.; Biliškov, N.; Chakraborty, S.; Charalambopoulou, G.; Chaudhary, A.-L.; Cuevas, F.; et al. Nanostructured materials for solid-state hydrogen storage: A review of the achievement of COST Action MP1103. *Int. J. Hydrogen Energy* **2016**, *41*, 14404–14428. [CrossRef]

63. Turani-Belloto, K.; Castilla-Martinez, C.A.; Cot, D.; Petit, E.; Benarib, S.; Demirci, U.B. Nanosized ammonia borane for solid-state hydrogen storage: Outcomes, limitations, challenges and opportunities. *Int. J. Hydrogen Energy* **2021**, *46*, 7351–7370. [CrossRef]

64. Valero-Pedraza, M.-J.; Cot, D.; Petit, E.; Aguey-Zinsou, K.-F.; Alauzun, J.G.; Demirci, U.B. Ammonia Borane Nanospheres for Hydrogen Storage. *ACS Appl. Nano Mater.* **2019**, *2*, 1129–1138. [CrossRef]

65. Zhao, Y.; Zhu, Y.; Liu, J.; Ma, Z.; Zhang, J.; Liu, Y.; Li, Y.; Li, L. Enhancing hydrogen storage properties of MgH_2 by core-shell CoNi@C. *J. Alloys Compd.* **2021**, *862*, 158004. [CrossRef]

66. de Kort, L.M.; Gulino, V.; de Jongh, P.E.; Ngene, P. Ionic conductivity in complex metal hydride-based nanocomposite materials: The impact of nanostructuring and nanocomposite formation. *J. Alloys Compd.* **2022**, *901*, 163474. [CrossRef]

67. Pasquini, L. Design of Nanomaterials for Hydrogen Storage. *Energies* **2020**, *13*, 3503. [CrossRef]

68. Malouche, A.; Zlotea, C.; Szilágyi, P.Á. Interactions of hydrogen with Pd@MOF composites. *ChemPhysChem* **2019**, *20*, 1282–1295. [CrossRef] [PubMed]

69. EHuang, Y.; Shao, H.; Zhang, Q.; Zang, L.; Guo, H.; Liu, Y.; Jiao, L.; Yuan, H.; Wang, Y. Layer-by-layer uniformly confined Graphene-$NaAlH_4$ composites and hydrogen storage performance. *Int. J. Hydrogen Energy* **2020**, *45*, 28116–28122. [CrossRef]

70. Zheng, J.; Yao, Z.; Xiao, X.; Wang, X.; He, J.; Chen, M.; Cheng, H.; Zhang, L.; Chen, L. Enhanced hydrogen storage properties of high-loading nanoconfined $LiBH_4$-$Mg(BH_4)_2$ composites with porous hollow carbon nanospheres. *Int. J. Hydrogen Energy* **2021**, *46*, 852–864. [CrossRef]

71. Boateng, E.; Chen, A. Recent advances in nanomaterial-based solid-state hydrogen storage. *Mater. Today Adv.* **2020**, *6*, 100022. [CrossRef]

72. Luo, Y.; Wang, Q.; Li, J.; Xu, F.; Sun, L.; Zou, Y.; Chu, H.; Li, B.; Zhang, K. Enhanced Hydrogen Storage/Sensing of Metal Hydrides by Nano-modification. *Mater. Today Nano* **2020**, *9*, 100071. [CrossRef]

73. Castilla-Martinez, C.A.; Moury, R.; Ould-Amara, S.; Demirci, U.B. Destabilization of Boron-Based Compounds for Hydrogen Storage in the Solid-State: Recent Advances. *Energies* **2021**, *14*, 7003. [CrossRef]

74. Luo, X.; Rawal, A.; Aguey-Zinsou, K.-F. Investigating the Factors Affecting the Ionic Conduction in Nanoconfined $NaBH_4$. *Inorganics* **2021**, *9*, 2. [CrossRef]

75. Biswas, P.; Ghildiyal, P.; Kwon, H.; Wang, H.; Alibay, Z.; Xu, F.; Wang, Y.; Wong, B.M.; Zachariah, M.R. Rerouting Pathways of Solid-State Ammonia Borane Energy Release. *J. Phys. Chem. C* **2022**, *126*, 48–57. [CrossRef]

76. Bannenberg, L.J.; Boshuizen, B.; Nugroho, F.A.A.; Schreuders, H. Hydrogenation Kinetics of Metal Hydride Catalytic Layers. *ACS Appl. Mater. Interfaces* **2021**, *13*, 52530–52541. [CrossRef] [PubMed]

77. El-Eskandarany, M.S.; Al-Ajmi, F.; Banyan, M.; Al-Duweesh, A. Synergetic effect of reactive ball milling and cold pressing on enhancing the hydrogen storage behavior of nanocomposite MgH_2/10 wt% $TiMn_2$ binary system. *Int. J. Hydrogen Energy* **2019**, *44*, 26428–26443. [CrossRef]

78. Huang, X.; Xiao, X.; He, Y.; Yao, Z.; Ye, X.; Kou, H.; Chen, C.; Huang, T.; Fan, X.; Chen, L. Probing an intermediate state by X-ray absorption near-edge structure in nickel-doped $2LiBH_4$-MgH_2 reactive hydride composite at moderate temperature. *Mater. Today Nano* **2020**, *12*, 100090. [CrossRef]

79. Guo, Q.; Chen, R.; Guo, J.; Qin, C.; Xiong, Z.; Yan, H.; Gao, W.; Pei, Q.; Wu, A.; Chen, P. Enabling Semihydrogenation of Alkynes to Alkenes by Using a Calcium Palladium Complex Hydride. *J. Am. Chem. Soc.* **2021**, *143*, 20891–20897. [CrossRef] [PubMed]

80. Ma, Z.; Panda, S.; Zhang, Q.; Sun, F.; Khan, D.; Ding, W.; Zou, J. Improving hydrogen sorption performances of MgH_2 through nanoconfinement in a mesoporous CoS nano-boxes scaffold. *J. Chem. Eng.* **2021**, *406*, 126790. [CrossRef]

81. Ngene, P.; Verkuijlen, M.H.W.; Barre, C.; Kentgens, A.P.M.; de Jongh, P.E. Reversible Li-insertion in nanoscaffolds: A promising strategy to alter the hydrogen sorption properties of Li-based complex hydrides. *Nano Energy* **2016**, *22*, 169–178. [CrossRef]

82. Paskevicius, M.; Filsø, U.; Karimi, F.; Puszkiel, J.; Pranzas, P.K.; Pistidda, C.; Hoell, A.; Welter, E.; Schreyer, A.; Klassen, T.; et al. Cyclic stability and structure of nanoconfined Ti-doped $NaAlH_4$. *Int. J. Hydrogen Energy* **2016**, *41*, 4159–4167. [CrossRef]

83. Sanz-Moral, L.M.; Navarrete, A.; Sturm, G.; Link, G.; Rueda, M.; Stefanidis, G.; Martín, A. Release of hydrogen from nanoconfined hydrides by application of microwaves. *J. Power Sources* **2017**, *353*, 131–137. [CrossRef]

84. Pasquini, L. The effects of nanostructure on the hydrogen sorption properties of magnesium-based metallic compounds: A review. *Crystals* **2018**, *8*, 106. [CrossRef]

85. Liu, W.; Stoddart, J.F. Emergent behavior in nanoconfined molecular containers. *Chem.* **2021**, *7*, 919–947. [CrossRef]

86. Li, X.; Yang, X.; Xue, H.; Pang, H.; Xu, Q. Metal–organic frameworks as a platform for clean energy applications. *EnergyChem* **2020**, *2*, 100027. [CrossRef]

87. Lambregts, S.F.H.; van Eck, E.R.H.; Suwarno; Ngene, P.; de Jongh, P.E.; Kentgens, A.P.M. Phase Behavior and Ion Dynamics of Nanoconfined $LiBH_4$ in Silica. *J. Phys. Chem. C* **2019**, *123*, 25559–25569. [CrossRef]

88. Mishra, S.; Kang, P.-C.; Guo, R.-F.; Wang, C.-Y.; Nebhani, L. Combined Effect of Functionality and Pore Size on Dehydrogenation of Ammonia Borane via Its Nanoconfinement in Polyacrylamide-Grafted Organically Modified Mesoporous Silica. *ACS Appl. Energy Mater.* **2021**, *4*, 6585–6598. [CrossRef]

89. Yang, Q.; Lu, F.; Liu, Y.; Zhang, Y.; Wang, X.; Pang, Y.; Zheng, S. $Li_2(BH_4)(NH_2)$ Nanoconfined in SBA-15 as Solid-State Electrolyte for Lithium Batteries. *Nanomaterials* **2021**, *11*, 946. [CrossRef]

90. Rueda, M.; Sanz-Moral, L.M.; Segovia, J.J.; Martín, Á. Improvement of the kinetics of hydrogen release from ammonia borane confined in silica aerogel. *Microporous Mesoporous Mater.* **2017**, *237*, 189–200. [CrossRef]

91. de Kort, L.M.; Harmel, J.; de Jongh, P.E.; Ngene, P. The effect of nanoscaffold porosity and surface chemistry on the Li-ion conductivity of $LiBH_4$-$LiNH_2$/metal oxide nanocomposites. *J. Mater. Chem. A* **2020**, *8*, 20687–20697. [CrossRef]

92. Jia, Y.; Yao, X. Carbon scaffold modified by metal (Ni) or non-metal (N) to enhance hydrogen storage of MgH_2 through nanoconfinement. *Int. J. Hydrogen Energy* **2017**, *42*, 22933–22941. [CrossRef]

93. Wu, R.; Zhang, X.; Liu, Y.; Zhang, L.; Hu, J.; Gao, M.; Pan, H. A Unique Double-Layered Carbon Nanobowl-Confined Lithium Borohydride for Highly Reversible Hydrogen Storage. *Small* **2020**, *16*, 2001963. [CrossRef]

94. Hu, M.; Xie, X.; Chen, M.; Zhu, C.; Liu, T. TiC_X-decorated Mg nanoparticles confined in carbon shell: Preparation and catalytic mechanism for hydrogen storage. *J. Alloys Compd.* **2020**, *817*, 152813. [CrossRef]

95. Zhang, M.; Xiao, X.; Mao, J.; Lan, Z.; Huang, X.; Lu, Y.; Luo, B.; Liu, M.; Chen, M.; Chen, L. Synergistic catalysis in monodispersed transition metal oxide nanoparticles anchored on amorphous carbon for excellent low-temperature dehydrogenation of magnesium hydride. *Mater. Today Energy* **2019**, *12*, 146–154. [CrossRef]

96. Wang, L.; Rawal, A.; Quadir, M.Z.; Aguey-Zinsou, K.-F. Nanoconfined lithium aluminium hydride ($LiAlH_4$) and hydrogen reversibility. *Int. J. Hydrogen Energy* **2017**, *42*, 14144–14153. [CrossRef]

97. Zlotea, C.; Oumellal, Y.; Berrú, J.J.S.; Aguey-Zinsou, K.-F. On the feasibility of the bottom-up synthesis of Mg_2CoH_5 nanoparticles supported on a porous carbon and their hydrogen desorption behaviour. *Nano-Struct. Nano-Objects* **2018**, *16*, 144–150. [CrossRef]

98. Huang, Y.; Xia, G.; Chen, J.; Zhang, B.; Li, Q.; Yu, X. One-step uniform growth of magnesium hydride nanoparticles on graphene. *Prog. Nat. Sci. Mater. Int.* **2017**, *27*, 81–87. [CrossRef]

99. Zhou, H.; Wang, X.; Liu, H.; Yan, M. Enhanced hydrogen storage properties of $2LiBH_4$-$LiAlH_4$ nanoconfined in resorcinol formaldehyde carbon aerogel. *J. Alloys Compd.* **2017**, *726*, 525–531. [CrossRef]

100. Zhou, H.; Liu, H.-z.; Gao, S.-c.; Wang, X.-h. Enhanced dehydrogenation kinetic properties and hydrogen storage reversibility of $LiBH_4$ confined in activated charcoal. *Trans. Nonferrous Met. Soc. China* **2018**, *28*, 1618–1625. [CrossRef]

101. Xia, Y.; Wei, S.; Huang, Q.; Li, J.; Cen, X.; Zhang, H.; Chu, H.; Sun, L.; Xu, F.; Huang, P. Facile synthesis of $NiCo_2O_4$-anchored reduced graphene oxide nanocomposites as efficient additives for improving the dehydrogenation behavior of lithium alanate. *Inorg. Chem. Front.* **2020**, *7*, 1257–1272. [CrossRef]

102. Wang, Y.; Ding, Z.; Li, X.; Ren, S.; Zhou, S.; Zhang, H.; Li, Y.; Han, S. Improved hydrogen storage properties of MgH_2 by nickel@nitrogen-doped carbon spheres. *Dalton Trans.* **2020**, *49*, 3495–3502. [CrossRef]

103. Zhang, B.; Xia, G.; Sun, D.; Fang, F.; Yu, X. Magnesium Hydride Nanoparticles Self-Assembled on Graphene as Anode Material for High-Performance Lithium-Ion Batteries. *ACS Nano* **2018**, *12*, 3816–3824. [CrossRef]

104. Wang, S.; Gao, M.; Xian, K.; Li, Z.; Shen, Y.; Yao, Z.; Liu, Y.; Pan, H. $LiBH_4$ Nanoconfined in Porous Hollow Carbon Nanospheres with High Loading, Low Dehydrogenation Temperature, Superior Kinetics, and Favorable Reversibility. *ACS Appl. Energy Mater.* **2020**, *3*, 3928–3938. [CrossRef]

105. Aditya, M.V.V.S.; Panda, S.; Tatiparti, S.S.V. Boron from net charge acceptor to donor and its effect on hydrogen uptake by novel Mg-B-electrochemically synthesized reduced graphene oxide. *Sci. Rep.* **2021**, *11*, 10995. [CrossRef]

106. Wang, S.; Gao, M.; Yao, Z.; Liu, Y.; Wu, M.; Li, Z.; Liu, Y.; Sun, W.; Pan, H. A nanoconfined-$LiBH_4$ system using a unique multifunctional porous scaffold of carbon wrapped ultrafine Fe_3O_4 skeleton for reversible hydrogen storage with high capacity. *Chem. Eng. J.* **2022**, *428*, 131056. [CrossRef]

107. Zhang, J.; Zhu, Y.; Lin, H.; Liu, Y.; Zhang, Y.; Li, S.; Ma, Z.; Li, L. Metal Hydride Nanoparticles with Ultrahigh Structural Stability and Hydrogen Storage Activity Derived from Microencapsulated Nanoconfinement. *Adv. Mater.* **2017**, *29*, 1700760. [CrossRef] [PubMed]

108. Sitthiwet, C.; Thiangviriya, S.; Thaweelap, N.; Meethom, S.; Kaewsuwan, D.; Chanlek, N.; Utke, R. Hydrogen sorption and permeability of compacted $LiBH_4$ nanoconfined into activated carbon nanofibers impregnated with TiO_2. *J. Phys. Chem. Solids* **2017**, *110*, 344–353. [CrossRef]

109. Duan, C.; Wu, M.; Cao, Y.; Fu, D.; Zhang, Y.; Su, Z.; Sun, Z.; Wu, Y. Novel core–shell structured MgH_2/AlH_3@CNT nanocomposites with extremely high dehydriding–rehydriding properties derived from nanoconfinement. *J. Mater. Chem. A* **2021**, *9*, 10921. [CrossRef]

110. Han, D.J.; Bang, K.R.; Cho, H.; Cho, E.S. Effect of carbon nanoscaffolds on hydrogen storage performance of magnesium hydride. *Korean J. Chem. Eng.* **2020**, *37*, 1306–1316. [CrossRef]

111. Cho, Y.J.; Li, S.; Snider, J.L.; Marple, M.A.T.; Strange, N.A.; Sugar, J.D.; Gabaly, F.E.; Schneemann, A.; Kang, S.; Kang, M.-h.; et al. Reversing the Irreversible: Thermodynamic Stabilization of $LiAlH_4$ Nanoconfined Within a Nitrogen-Doped Carbon Host. *ACS Nano* **2021**, *15*, 10163–10174. [CrossRef]

112. Gasnier, A.; Luguet, M.; Pereira, A.G.; Troiani, H.; Zampieri, G.; Gennari, F.C. Entanglement of N-doped graphene in resorcinol-formaldehyde: Effect over nanoconfined $LiBH_4$ for hydrogen storage. *Carbon* **2019**, *147*, 284–294. [CrossRef]

113. Gasnier, A.; Amica, G.; Juan, J.; Troiani, H.; Gennari, F.C. N-Doped Graphene-Rich Aerogels Decorated with Nickel and Cobalt Nanoparticles: Effect on Hydrogen Storage Properties of Nanoconfined LiBH$_4$. *J. Phys. Chem. C* **2020**, *124*, 115–125. [CrossRef]

114. Xia, G.; Tan, Y.; Chen, X.; Fang, F.; Sun, D.; Li, X.; Guo, Z.; Yu, X. Oxygen-free Layer-by-Layer Assembly of Lithiated Composites on Graphene for Advanced Hydrogen Storage. *Adv. Sci.* **2016**, *4*, 1600257. [CrossRef]

115. Zhang, Q.; Huang, Y.; Xu, L.; Zang, L.; Guo, H.; Jiao, L.; Yuan, H.; Wang, Y. Highly Dispersed MgH$_2$ Nanoparticle–Graphene Nanosheet Composites for Hydrogen Storage. *ACS Appl. Nano Mater.* **2019**, *2*, 3828–3835. [CrossRef]

116. Comanescu, C.; Capurso, G.; Maddalena, A. Nanoconfinement in activated mesoporous carbon of calcium borohydride for improved reversible hydrogen storage. *Nanotechnology* **2012**, *23*, 385401. [CrossRef] [PubMed]

117. Wan, L.F.; Cho, E.S.; Marangoni, T.; Shea, P.; Kang, S.Y.; Rogers, C.; Zaia, E.; Cloke, R.R.; Wood, B.C.; Fischer, F.R.; et al. Edge-Functionalized Graphene Nanoribbon Encapsulation to Enhance Stability and Control Kinetics of Hydrogen Storage Materials. *Chem. Mater.* **2019**, *31*, 2960–2970. [CrossRef]

118. Wang, S.; Gao, M.; Yao, Z.; Xian, K.; Wu, M.; Liu, Y.; Sun, W.; Pan, H. High-loading, ultrafine Ni nanoparticles dispersed on porous hollow carbon nanospheres for fast (de)hydrogenation kinetics of MgH$_2$. *J. Magnes. Alloys* **2021**. [CrossRef]

119. Morse, J.R.; Zugell, D.A.; Patterson, E.; Baldwin, J.W.; Willauer, H.D. Hydrogenated graphene: Important material properties regarding its application for hydrogen storage. *J. Power Sources* **2021**, *494*, 229734. [CrossRef]

120. Zhang, X.; Zhang, L.; Zhang, W.; Ren, Z.; Huang, Z.; Hu, J.; Gao, M.; Pan, H.; Liu, Y. Nano-synergy enables highly reversible storage of 9.2 wt% hydrogen at mild conditions with lithium borohydride. *Nano Energy* **2021**, *83*, 105839. [CrossRef]

121. Han, D.J.; Kim, S.; Cho, E.S. Revealing the role of defects in graphene oxide in the evolution of magnesium nanocrystals and the resulting effects on hydrogen storage. *J. Mater. Chem. A* **2021**, *9*, 9875. [CrossRef]

122. Dun, C.; Jeong, S.; Kwon, D.-H.; Kang, S.Y.; Stavila, V.; Zhang, Z.; Lee, J.-W.; Mattox, T.M.; Heo, T.W.; Wood, B.C.; et al. Hydrogen Storage Performance of Preferentially Oriented Mg/rGO Hybrids. *Chem. Mater.* **2022**, *34*, 2963–2971. [CrossRef]

123. Martínez, A.A.; Gasnier, A.; Gennari, F.C. Pore Filling of a Carbon Matrix by Melt-Impregnated LiBH$_4$. *J. Phys. Chem. C* **2022**, *126*, 66–78. [CrossRef]

124. Cho, H.; Hyeon, S.; Park, H.; Kim, J.; Cho, E.S. Ultrathin Magnesium Nanosheet for Improved Hydrogen Storage with Fishbone Shaped One-Dimensional Carbon Matrix. *ACS Appl. Energy Mater.* **2020**, *3*, 8143–8149. [CrossRef]

125. Ko, Y.; Lombardo, L.; Li, M.; Oveisi, E.; Yang, H.; Züttel, A. Interfacial Effect between Aluminum-Based Complex Hydrides and Nickel-Containing Porous Carbon Sheets. *ACS Appl. Energy Mater.* **2020**, *3*, 9685–9695. [CrossRef]

126. Jeong, S.; Heo, T.W.; Oktawiec, J.; Shi, R.; Kang, S.Y.; White, J.L.; Schneemann, A.; Zaia, E.W.; Wan, L.F.; Ray, K.G.; et al. A Mechanistic Analysis of Phase Evolution and Hydrogen Storage Behavior in Nanocrystalline Mg(BH$_4$)$_2$ within Reduced Graphene Oxide. *ACS Nano* **2020**, *14*, 1745–1756. [CrossRef] [PubMed]

127. Beatrice, C.A.G.; Moreira, B.R.; de Oliveira, A.D.; Passador, F.R.; de Almeida Neto, G.R.; Leiva, D.R.; Pessan, L.A. Development of polymer nanocomposites with sodium alanate for hydrogen storage. *Int. J. Hydrogen Energy* **2020**, *45*, 5337–5346. [CrossRef]

128. Carr, C.L.; Jayawardana, W.; Zou, H.; White, J.L.; Gabaly, F.E.; Conradi, M.S.; Stavila, V.; Allendorf, M.D.; Majzoub, E.H. Anomalous H$_2$ Desorption Rate of NaAlH$_4$ Confined in Nitrogen-Doped Nanoporous Carbon Frameworks. *Chem. Mater.* **2018**, *30*, 2930–2938. [CrossRef]

129. Do, H.W.; Kim, H.; Cho, E.S. Enhanced hydrogen storage kinetics and air stability of nanoconfined NaAlH$_4$ in graphene oxide framework. *RSC Adv.* **2021**, *11*, 32533. [CrossRef] [PubMed]

130. Dansirima, P.; Thiangviriya, S.; Plerdsranoy, P.; Utke, O.; Utke, R. Small hydrogen storage tank filled with 2LiBH$_4$-MgH$_2$ nanoconfined in activated carbon: Reaction mechanisms and performances. *Int. J. Hydrogen Energy* **2019**, *44*, 10752–10762. [CrossRef]

131. Magnin, Y.; Villermaux, E.; Amara, H.; Bichara, C.; Pellenq, R.J.M. Morphology control of metallic nanoparticles supported on carbon substrates in catalytic conditions. *Carbon* **2020**, *159*, 504–511. [CrossRef]

132. Wahab, M.A.; Young, D.J.; Karim, A.; Fawzia, S.; Beltramini, J.N. Low-temperature hydrogen desorption from Mg(BH$_4$)$_2$ catalysed by ultrafine Ni nanoparticles in a mesoporous carbon matrix. *Int. J. Hydrogen Energy* **2016**, *41*, 20573–20582. [CrossRef]

133. Wang, L.; Quadir, M.Z.; Aguey-Zinsou, K.-F. Direct and reversible hydrogen storage of lithium hydride (LiH) nanoconfined in high surface area graphite. *Int. J. Hydrogen Energy* **2016**, *41*, 18088–18094. [CrossRef]

134. Utke, R.; Thiangviriya, S.; Javadian, P.; Jensen, T.R.; Milanese, C.; Klassen, T.; Dornheim, M. 2LiBH$_4$–MgH$_2$ nanoconfined into carbon aerogel scaffold impregnated with ZrCl$_4$ for reversible hydrogen storage. *Mater. Chem. Phys.* **2016**, *169*, 136–141. [CrossRef]

135. Plerdsranoy, P.; Javadian, P.; Jensen, N.D.; Nielsen, U.G.; Jensen, T.R.; Utke, R. Compaction of LiBH$_4$-LiAlH$_4$ nanoconfined in activated carbon nanofibers: Dehydrogenation kinetics, reversibility, and mechanical stability during cycling. *Int. J. Hydrogen Energy* **2017**, *42*, 1036–1047. [CrossRef]

136. Pandey, A.P.; Bhatnagar, A.; Shukla, V.; Soni, P.K.; Singh, S.; Verma, S.K.; Shaneeth, M.; Sekkar, V.; Srivastava, O.N. Hydrogen storage properties of carbon aerogel synthesized by ambient pressure drying using new catalyst triethylamine. *Int. J. Hydrogen Energy* **2020**, *45*, 30818–30827. [CrossRef]

137. Shinde, S.S.; Kim, D.H.; Yu, J.Y.; Lee, J.H. Self-assembled air-stable magnesium hydride embedded in 3-D activated carbon for reversible hydrogen storage. *Nanoscale* **2017**, *9*, 7094–7103. [CrossRef]

138. Cho, E.S.; Ruminski, A.M.; Aloni, S.; Liu, Y.-S.; Guo, J.; Urban, J.J. Graphene oxide/metal nanocrystal multilaminates as the atomic limit for safe and selective hydrogen storage. *Nat. Commun.* **2016**, *7*, 10804. [CrossRef] [PubMed]

139. Fang, M.H.; Wu, S.Y.; Chang, Y.H.; Narwane, M.; Chen, B.H.; Liu, W.L.; Kurniawan, D.; Chiang, W.H.; Lin, C.H.; Chuang, Y.C.; et al. Mechanistic Insight into the Synergetic Interaction of Ammonia Borane and Water on ZIF-67-Derived Co@Porous Carbon for Controlled Generation of Dihydrogen. *ACS Appl. Mater. Interfaces* **2021**, *13*, 47465–47477. [CrossRef] [PubMed]

140. Cao, Z.; Ouyang, L.; Felderhoff, M.; Zhu, M. Low temperature dehydrogenation properties of ammonia borane within carbon nanotube arrays: A synergistic effect of nanoconfinement and alane. *RSC Adv.* **2020**, *10*, 19027–19033. [CrossRef] [PubMed]

141. So, S.H.; Jang, J.H.; Sung, S.J.; Yang, S.J.; Nam, K.T.; Park, C.R. Demonstration of the nanosize effect of carbon nanomaterials on the dehydrogenation temperature of ammonia borane. *Nanoscale Adv.* **2019**, *1*, 4697–4703. [CrossRef]

142. Champet, S.; van den Berg, J.; Szczesny, R.; Godula-Jopek, A.; Gregory, D.H. Nano-inclusion in one step: Spontaneous ice-templating of porous hierarchical nanocomposites for selective hydrogen release. *Sustain. Energy Fuels* **2019**, *3*, 396–400. [CrossRef]

143. Liu, H.; Chen, S.; Liu, M.; Cui, J.; Wang, Z.; Yu, P. Enhanced dehydrogenation performance of ammonia borane con-catalyzed by novel TiO$_2$(B) nanoparticles and bio-derived carbon with well-organized pores. *Int. J. Hydrogen Energy* **2020**, *45*, 28070–28077. [CrossRef]

144. Yang, Z.; Zhou, D.; Chen, B.; Liu, Z.; Xia, Q.; Zhu, Y.; Xia, Y. Improved hydrogen release from ammonia borane confined in microporous carbon with narrow pore size distribution. *J. Mater. Chem. A* **2017**, *5*, 15395–15400. [CrossRef]

145. Fang, L.; Feng, J.J.; Shi, X.; Si, T.; Song, Y.; Jia, H.; Li, Y.; Li, H.-W.; Zhang, Q. Turn Bulks into 0D, 1D and 2D Metallic Nanomaterials by Selective Aqueous Corrosion. *Chem. Commun.* **2019**, *55*, 10476–10479. [CrossRef]

146. Zhang, X.; Leng, Z.; Gao, M.; Hu, J.; Du, F.; Yao, J.; Pan, H.; Liu, Y. Enhanced hydrogen storage properties of MgH$_2$ catalyzed with carbon-supported nanocrystalline TiO$_2$. *J. Power Sources* **2018**, *398*, 183–192. [CrossRef]

147. Zhang, L.; Nyahuma, F.M.; Zhang, H.; Cheng, C.; Zheng, J.; Wu, F.; Chen, L. Metal organic framework supported niobium pentoxide nanoparticles with exceptional catalytic effect on hydrogen storage behavior of MgH$_2$. *Green Energy Environ.* **2022**. [CrossRef]

148. Wang, T.C.; White, J.L.; Bie, B.; Deng, H.; Edgington, J.; Sugar, J.D.; Stavila, V.; Allendorf, M.D. Design Rules for Metal-Organic Framework Stability in High-Pressure Hydrogen Environments. *ChemPhysChem* **2019**, *20*, 1305–1310. [CrossRef] [PubMed]

149. Ma, Z.; Zhang, Q.; Panda, S.; Zhu, W.; Sun, F.; Khan, D.; Dong, J.; Ding, W.; Zou, J. In-situ catalyzed and nanoconfined magnesium hydride nanocrystals in a Ni-MOF scaffold for hydrogen storage. *Sustain. Energy Fuels* **2020**, *4*, 4694–4703. [CrossRef]

150. Callini, E.; Szilagyi, P.A.; Paskevicius, M.; Stadie, N.P.; Rehault, J.; Buckley, C.E.; Borgschulte, A.; Zuttel, A. Stabilization of volatile Ti(BH$_4$)$_3$ by nanoconfinement in a metal–organic framework. *Chem. Sci.* **2016**, *7*, 666–672. [CrossRef] [PubMed]

151. Schneemann, A.; Wan, L.F.; Lipton, A.S.; Liu, Y.-S.; Snider, J.L.; Baker, A.A.; Sugar, J.D.; Spataru, C.D.; Guo, J.; Autrey, T.S.; et al. Nanoconfinement of Molecular Magnesium Borohydride Captured in a Bipyridine-Functionalized Metal−Organic Framework. *ACS Nano* **2020**, *14*, 10294–10304. [CrossRef]

152. Bobbitt, N.S.; Snurr, R.Q. Molecular modelling and machine learning for high-throughput screening of metal-organic frameworks for hydrogen storage. *Mol. Simul.* **2019**, *45*, 1069–1081. [CrossRef]

153. Chung, J.-Y.; Liao, C.-W.; Chang, Y.-W.; Chang, B.K.; Wang, H.; Li, J.; Wang, C.-Y. Influence of Metal−Organic Framework Porosity on Hydrogen Generation from Nanoconfined Ammonia Borane. *J. Phys. Chem. C* **2017**, *121*, 27369–27378. [CrossRef]

154. Peil, S.; Wisser, D.; Stähle, M.; Roßmann, P.K.; Avadhut, Y.S.; Hartmann, M. Hydrogen Release from Ammonia Borane Nanoconfined in Metal−Organic Frameworks with MIL-53 Topology. *J. Phys. Chem. C* **2021**, *125*, 9990–10000. [CrossRef]

155. Ullman, A.M.; Brown, J.W.; Foster, M.E.; Leonard, F.; Leong, K.; Stavila, V.; Allendorf, M.D. Transforming MOFs for Energy Applications Using the Guest@MOF Concept. *Inorg. Chem.* **2016**, *55*, 7233–7249. [CrossRef]

156. Zhou, Z.; Yu, F.; Ma, J. Nanoconfinement engineering for enhanced adsorption of carbon materials, metal–organic frameworks, mesoporous silica, MXenes and porous organic polymers: A review. *Environ. Chem. Lett.* **2022**, *20*, 563–595. [CrossRef]

157. Wang, Y.; Lan, Z.; Huang, X.; Liu, H.; Guo, J. Study on catalytic effect and mechanism of MOF (MOF = ZIF-8, ZIF-67, MOF-74) on hydrogen storage properties of magnesium. *Int. J. Hydrogen Energy* **2019**, *44*, 28863–28873. [CrossRef]

158. Huang, T.; Huang, X.; Hu, C.; Wang, J.; Liu, H.; Ma, Z.; Zou, J.; Ding, W. Enhancing hydrogen storage properties of MgH$_2$ through addition of Ni/CoMoO$_4$ nanorods. *Mater. Today Energy* **2021**, *19*, 100613. [CrossRef]

159. Leick, N.; Strange, N.A.; Schneemann, A.; Stavila, V.; Gross, K.; Washton, N.; Settle, A.; Martinez, M.B.; Gennett, T.; Christensen, S.T. Al$_2$O$_3$ Atomic Layer Deposition on Nanostructured γ-Mg(BH$_4$)$_2$ for H$_2$ Storage. *ACS Appl. Energy Mater.* **2021**, *4*, 1150–1162. [CrossRef]

160. Habibi, P.; Vlugt, T.J.H.; Dey, P.; Moultos, O.A. Reversible Hydrogen Storage in Metal-Decorated Honeycomb Borophene Oxide. *ACS Appl. Mater. Interfaces* **2021**, *13*, 43233–43240. [CrossRef]

161. Zettl, R.; Gombotz, M.; Clarkson, D.; Greenbaum, S.G.; Ngene, P.; de Jongh, P.E.; Wilkening, H.M.R. Li-Ion Diffusion in Nanoconfined LiBH$_4$-LiI/Al$_2$O$_3$: From 2D Bulk Transport to 3D Long-Range Interfacial Dynamics. *ACS Appl. Mater. Interfaces* **2020**, *12*, 38570–38583. [CrossRef]

162. Salameh, C.; Moussa, G.; Bruma, A.; Fantozzi, G.; Malo, S.; Miele, P.; Demirci, U.B.; Bernard, S. Robust 3D Boron Nitride Nanoscaffolds for Remarkable Hydrogen Storage Capacity from Ammonia Borane. *Energy Technol.* **2018**, *6*, 570–577. [CrossRef]

163. Cho, E.S.; Ruminski, A.M.; Liu, Y.-S.; Shea, P.T.; Kang, S.Y.; Zaia, E.W.; Park, J.Y.; Chuang, Y.-D.; Yuk, J.M.; Zhou, X.; et al. Hierarchically Controlled Inside-Out Doping of Mg Nanocomposites for Moderate Temperature Hydrogen Storage. *Adv. Funct. Mater.* **2017**, *27*, 1704316. [CrossRef]

164. Fan, J.; Cui, X.; Yu, S.; Gu, L.; Zhang, Q.; Meng, F.; Peng, Z.; Ma, L.; Ma, J.-Y.; Qi, K.; et al. Interstitial Hydrogen Atom Modulation to Boost Hydrogen Evolution in Pd-Based Alloy Nanoparticles. *ACS Nano* **2019**, *13*, 12987–12995. [CrossRef]

165. Abbas, A.; Rajagopal, V.; Huang, S.J. Magnesium metal matrix composites and their applications. In *Magnesium Alloys*; IntechOpen: London, UK, 2021. [CrossRef]

166. Li, Z.; Yu, J.Z.; Zhang, Y.; Liu, D.M.; Wang, C.Y.; Si, T.Z.; Li, Y.T.; Zhang, Q.A. Coupling of nanoconfinement with metallic catalysis in supported $NaAlH_4$ for low-temperature hydrogen storage. *J. Power Sources* **2021**, *491*, 229611. [CrossRef]

167. Ianni, E.; Sofianos, M.V.; Rowles, M.R.; Sheppard, D.A.; Humphries, T.D.; Buckley, C.E. Synthesis of $NaAlH_4$/Al composites and their applications in hydrogen storage. *Int. J. Hydrogen Energy* **2018**, *43*, 17309–17317. [CrossRef]

168. Khan, D.; Zou, J.; Pan, M.; Ma, Z.; Zhu, W.; Huang, T.; Zeng, X.; Ding, W. Hydrogen storage properties of nanostructured $2MgH_2$-Co powders: The effect of high-pressure compression. *Int. J. Hydrogen Energy* **2019**, *44*, 15146–15158. [CrossRef]

169. Rizo-Acosta, P.; Cuevas, F.; Latroche, M. Hydrides of early transition metals as catalysts and grain growth inhibitors for enhanced reversible hydrogen storage in nanostructured magnesium. *J. Mater. Chem. A* **2019**, *7*, 23064–23075. [CrossRef]

170. Patelli, N.; Migliori, A.; Morandi, V.; Pasquini, L. Interfaces within biphasic nanoparticles give a boost to magnesium-based hydrogen storage. *Nano Energy* **2020**, *72*, 104654. [CrossRef]

171. Lai, Q.; Rawal, A.; Quadir, M.Z.; Cazorla, C.; Demirci, U.B.; Aguey-Zinsou, K.-F. Nanosizing Ammonia Borane with Nickel: A Path toward the Direct Hydrogen Release and Uptake of B-N-H Systems. *Adv. Sustain. Syst.* **2018**, *2*, 1700122. [CrossRef]

172. Ma, Z.; Liu, J.; Zhu, Y.; Zhao, Y.; Lin, H.; Zhang, Y.; Li, H.; Zhang, J.; Liu, Y.; Gao, W.; et al. Crystal-facet-dependent catalysis of anatase TiO_2 on hydrogen storage of MgH_2. *J. Alloys Compd.* **2020**, *822*, 153553. [CrossRef]

173. Le, T.T.; Pistidda, C.; Abetz, C.; Georgopanos, P.; Garroni, S.; Capurso, G.; Milanese, C.; Puszkiel, J.; Dornheim, M.; Abetz, V.; et al. Enhanced Stability of Li-RHC Embedded in an Adaptive TPX™ Polymer Scaffold. *Materials* **2020**, *13*, 991. [CrossRef]

174. Nugroho, F.A.A.; Darmadi, I.; Cusinato, L.; Susarrey-Arce, A.; Schreuders, H.; Bannenberg, L.J.; da Silva Fanta, A.B.; Kadkhodazadeh, S.; Wagner, J.B.; Antosiewicz, T.J.; et al. Metal–polymer hybrid nanomaterials for plasmonic ultrafast hydrogen detection. *Nat. Mater.* **2019**, *18*, 489–495. [CrossRef]

175. Ploszajski, A.R.; Billing, M.; Cockcroft, J.K.; Skipper, N.T. Crystalline structure of an ammonia borane–polyethylene oxide cocrystal: A material investigated for its hydrogen storage potential. *CrystEngComm* **2018**, *20*, 4436–4440. [CrossRef]

176. Kumar, J.A.; Prakash, P.; Krithiga, T.; Amarnath, D.J.; Premkumar, J.; Rajamohan, N.; Vasseghian, Y.; Saravanan, P.; Rajasimman, M. Methods of synthesis, characteristics, and environmental applications of MXene: A comprehensive review. *Chemosphere* **2022**, *286*, 131607. [CrossRef]

177. Wu, Z.; Fang, J.; Liu, N.; Wu, J.; Kong, L. The Improvement in Hydrogen Storage Performance of MgH_2 Enabled by Multilayer Ti_3C_2. *Micromachines* **2021**, *12*, 1190. [CrossRef] [PubMed]

178. Xia, Y.; Zhang, H.; Sun, Y.; Sun, L.; Xu, F.; Sun, S.; Zhang, G.; Huang, P.; Du, Y.; Wang, J.; et al. Dehybridization effect in improved dehydrogenation of $LiAlH_4$ by doping with two-dimensional Ti_3C_2. *Mater. Today Nano* **2019**, *8*, 100054. [CrossRef]

179. Chen, G.; Zhang, Y.; Cheng, H.; Zhu, Y.; Li, L.; Lin, H. Effects of two-dimension MXene Ti_3C_2 on hydrogen storage performances of MgH_2-$LiAlH_4$ composite. *Chem. Phys.* **2019**, *522*, 178–187. [CrossRef]

180. Ronchi, R.M.; Arantes, J.T.; Santos, S.F. Synthesis, structure, properties and applications of MXenes: Current status and perspectives. *Ceram. Int.* **2019**, *45*, 18167–18188. [CrossRef]

181. Liu, Y.; Gao, H.; Zhu, Y.; Li, S.; Zhang, J.; Li, L. Excellent catalytic activity of a two-dimensional $Nb_4C_3T_x$ (MXene) on hydrogen storage of MgH_2. *Appl. Surf. Sci.* **2019**, *493*, 431440. [CrossRef]

182. Yadav, A.; Dashora, A.; Patel, N.; Miotello, A.; Press, M.; Kothari, D.C. Study of 2D MXene Cr_2C material for hydrogen storage using density functional theory. *Appl. Surf. Sci.* **2016**, *389*, 88–95. [CrossRef]

183. Wu, R.; Du, H.; Wang, Z.; Gao, M.; Pan, H.; Liu, Y. Remarkably improved hydrogen storage properties of $NaAlH_4$ doped with 2D titanium carbide. *J. Power Sources* **2016**, *327*, 519–525. [CrossRef]

184. Shen, Z.; Wang, Z.; Zhang, M.; Gao, M.; Hu, J.; Du, F.; Liu, Y.; Pan, H. A novel solid-solution MXene $(Ti_{0.5}V_{0.5})_3C_2$ with high catalytic activity for hydrogen storage in MgH_2. *Materialia* **2018**, *1*, 114–120. [CrossRef]

185. Fan, Y.; Chen, D.; Liu, X.; Fan, G.; Liu, B. Improving the hydrogen storage performance of lithium borohydride by Ti_3C_2 MXene. *Int. J. Hydrogen Energy* **2019**, *44*, 29297–29303. [CrossRef]

186. Jiang, R.; Xiao, X.; Zheng, J.; Chen, M.; Chen, L. Remarkable hydrogen absorption/desorption behaviors and mechanism of sodium alanates in-situ doped with Ti-based 2D MXene. *Mater. Chem. Phys.* **2020**, *242*, 122529. [CrossRef]

187. Feng, X.; Yuan, J.; Lv, Y.; Liu, B.; Huang, H.; Zhang, B.; Yan, Y.; Han, S.; Wu, Y. Improvement of desorption performance of $Mg(BH_4)_2$ by two-dimensional Ti_3C_2 MXene addition. *Int. J. Hydrogen Energy* **2020**, *45*, 16654–16662. [CrossRef]

188. Yuan, Z.; Fan, Y.; Chen, Y.; Liu, X.; Liu, B.; Han, S. Two-dimensional $C@TiO_2/Ti_3C_2$ composite with superior catalytic performance for $NaAlH_4$. *Int. J. Hydrogen Energy* **2020**, *45*, 21666–21675. [CrossRef]

189. Zheng, J.; Cheng, H.; Xiao, X.; Chen, M.; Chen, L. Enhanced low temperature hydrogen desorption properties and mechanism of $Mg(BH_4)_2$ composited with 2D MXene. *Int. J. Hydrogen Energy* **2019**, *44*, 24292–24300. [CrossRef]

190. Wang, Z.; Zhang, X.; Ren, Z.; Liu, Y.; Hu, J.; Li, H.; Gao, M.; Pan, H.; Liu, Y. In situ formed ultrafine NbTi nanocrystals from a NbTiC solid-solution MXene for hydrogen storage in MgH_2. *J. Mater. Chem. A* **2019**, *7*, 14244–14252. [CrossRef]

191. Xian, K.X.; Gao, M.; Li, Z.; Gu, J.; Shen, Y.; Wang, S.; Yao, Z.; Liu, Y.; Pan, H. Superior Kinetic and Cyclic Performance of a 2D Titanium Carbide Incorporated $2LiH + MgB_2$ Composite toward Highly Reversible Hydrogen Storage. *ACS Appl. Energy Mater.* **2019**, *2*, 4853–4864. [CrossRef]

192. Gao, H.; Liu, Y.; Zhu, Y.; Zhang, J.; Li, L. Catalytic effect of sandwich-like Ti3C2/TiO2(A)-C on hydrogen storage performance of MgH2, Nanotechnology 2020, 31, 115404. *Nanotechnology* **2020**, *31*, 115404. [CrossRef]

193. Liu, Y.; Du, H.; Zhang, X.; Yang, Y.; Gao, M.; Pan, H. Superior catalytic activity derived from a two-dimensional Ti$_3$C$_2$ precursor towards the hydrogen storage reaction of magnesium hydride. *Chem. Commun.* **2016**, *52*, 705–708. [CrossRef]

194. Li, Y.; Guo, Y.; Chen, W.; Jiao, Z.; Ma, S. Reversible hydrogen storage behaviors of Ti$_2$N MXenes predicted by first-principles calculations. *J. Mater. Sci.* **2019**, *54*, 493–505. [CrossRef]

195. Veit, R.D.; Farber, R.G.; Sitaraman, N.S.; Arias, T.A.; Sibener, S.J. Suppression of nano-hydride growth on Nb(100) due to nitrogen doping. *J. Chem. Phys.* **2020**, *152*, 214703. [CrossRef]

196. Liu, Y.; Zhu, J.; Liu, Z.; Zhu, Y.; Zhang, J.; Li, L. Magnesium Nanoparticles with Pd Decoration for Hydrogen Storage. *Front. Chem.* **2020**, *7*, 949. [CrossRef]

197. Feng, Y.F.; Zhou, X.; Yang, J.-h.; Gao, X.; Yin, L.; Zhao, Y.; Zhang, B. Encapsulation of Ammonia Borane in Pd/Halloysite Nanotubes for Efficient Thermal Dehydrogenation. *ACS Sustain. Chem. Eng.* **2020**, *8*, 2122–2129. [CrossRef]

198. Snider, J.L.; Mattox, T.M.; Liu, Y.-S.; Wan, L.F.; Wijeratne, P.; Allendorf, M.D.; Stavila, V.; Wood, B.C.; Klebanoff, L.E. The influence of LiH and TiH$_2$ on hydrogen storage in MgB$_2$ II. XPS study of surface and near-surface phenomena. *Int. J. Hydrogen Energy* **2022**, *47*, 403–419. [CrossRef]

199. Wang, Y.; Chen, X.; Zhang, H.; Xia, G.; Sun, D.; Yu, X. Heterostructures Built in Metal Hydrides for Advanced Hydrogen Storage Reversibility. *Adv. Mater.* **2020**, *32*, 2002647. [CrossRef] [PubMed]

200. Dekura, S.; Kobayashi, H.; Kusada, K.; Kitagawa, H. Hydrogen and Storage Properties of Palladium and Related Nanomaterials: Size, Shape, Alloying, and Metal–Organic Framework Coating Effects. *ChemPhysChem* **2019**, *20*, 1158–1176. [CrossRef] [PubMed]

201. Yang, X.; Ji, L.; Yan, N.; Sun, Z.; Lu, X.; Zhang, L.; Zhu, X.; Chen, L. Superior catalytic effect of FeCo nanosheets on MgH$_2$ for hydrogen storage. *Dalton Trans.* **2019**, *48*, 12699–12706. [CrossRef]

202. Yang, X.; Hou, Q.; Yua, L.; Zhang, J. Improvement of the hydrogen storage characteristics of MgH$_2$ with a flake Ni nano-catalyst composite. *Dalton Trans.* **2021**, *50*, 1797. [CrossRef]

203. Duan, C.; Cao, Y.; Hu, L.; Fu, D.; Ma, J.; Youngblood, J. An efficient mechanochemical synthesis of alpha-aluminum hydride: Synergistic effect of TiF$_3$ on the crystallization rate and selective formation of alpha-aluminum hydride polymorph. *J. Hazard. Mater.* **2019**, *373*, 141–151. [CrossRef]

204. Huang, X.; Xiao, X.; Zhang, W.; Fan, X.; Zhang, L.; Cheng, C.; Li, S.; Ge, H.; Wang, Q.; Chen, L. Transition metal (Co, Ni) nanoparticles wrapped with carbon and their superior catalytic activities for the reversible hydrogen storage of magnesium hydride. *Phys. Chem. Chem. Phys.* **2017**, *19*, 4019–4029. [CrossRef]

205. Chen, Y.; Dai, J.; Song, Y. Catalytic mechanisms of TiH$_2$ thin layer on dehydrogenation behavior of fluorite-type MgH$_2$: A first principles study. *Int. J. Hydrogen Energy* **2020**, *45*, 21600–21610. [CrossRef]

206. Zhao, S.; Liang, L.; Liu, B.; Wang, L.; Liang, F. Superior Dehydrogenation Performance of α-AlH$_3$ Catalyzed by Li$_3$N: Realizing 8.0 wt.% Capacity at 100 °C. *Small* **2022**, *18*, 2107983. [CrossRef]

207. Dun, C.; Jeong, S.; Liu, Y.-S.; Leick, N.; Mattox, T.M.; Guo, J.; Lee, J.-W.; Gennett, T.; Stavila, V.; Urban, J.J. Additive Destabilization of Porous Magnesium Borohydride Framework with Core-Shell Structure. *Small* **2021**, *17*, 2101989. [CrossRef] [PubMed]

208. Ding, Z.; Zhang, L.; Fu, Y.; Wang, W.; Wang, Y.; Bi, J.; Li, Y.; Han, S. Enhanced kinetics of MgH$_2$ via in situ formed catalysts derived from MgCCo$_{1.5}$Ni$_{1.5}$. *J. Alloys Compd.* **2020**, *822*, 153621. [CrossRef]

209. Ding, Z.; Fu, Y.; Wang, Y.; Bi, J.; Zhang, L.; Peng, D.; Li, Y.; Han, S. MgCNi$_3$ prepared by powder metallurgy for improved hydrogen storage properties of MgH$_2$. *Int. J. Hydrogen Energy* **2019**, *44*, 8347–8356. [CrossRef]

210. Ding, X.; Ding, H.; Song, Y.; Xiang, C.; Li, Y.; Zhang, Q. Activity-Tuning of Supported Co–Ni Nanocatalysts via Composition and Morphology for Hydrogen Storage in MgH$_2$. *Front. Chem.* **2020**, *7*, 937. [CrossRef]

211. Patelli, N.; Migliori, A.; Pasquini, L. Reversible metal-hydride transformation in Mg-Ti-H nanoparticles at remarkably low temperatures. *Chem. Phys. Chem.* **2019**, *20*, 1325–1333. [CrossRef]

212. Kumar, S.; Pavloudis, T.; Singh, V.; Nguyen, H.; Steinhauer, S.; Pursell, C.; Clemens, B.; Kioseoglou, J.; Grammatikopoulos, P.; Sowwan, M. Hydrogen Flux through Size Selected Pd Nanoparticles into Underlying Mg Nanofilms. *Adv. Energy Mater.* **2018**, *8*, 1701326. [CrossRef]

213. Rossin, A.; Tuci, G.; Luconi, L.; Giambastiani, G. Metal–Organic Frameworks as Heterogeneous Catalysts in Hydrogen Production from Lightweight Inorganic Hydrides. *ACS Catal.* **2017**, *7*, 5035–5045. [CrossRef]

214. Sun, Y.; Aguey-Zinsou, K.-F. Light-activated hydrogen storage in Mg, LiH and NaAlH$_4$. *ChemPlusChem* **2018**, *83*, 904–908. [CrossRef]

215. White, J.L.; Baker, A.A.; Marcus, M.A.; Snider, J.L.; Wang, T.C.; Lee, J.R.I.; Kilcoyne, D.A.L.; Allendorf, M.D.; Stavila, V.; Gabaly, F.E. The Inside-Outs of Metal Hydride Dehydrogenation: Imaging the Phase Evolution of the Li-N-H Hydrogen Storage System. *Adv. Mater. Interfaces* **2020**, *7*, 1901905. [CrossRef]

216. Bannenberg, L.J.; Heere, M.; Benzidi, H.; Montero, J.; Dematteis, E.M.; Suwarno, S.; Jaron, T.; Winny, M.; Orłowski, P.A.; Wegner, W.; et al. Metal (boro-) hydrides for high energy density storage and relevant emerging technologies. *Int. J. Hydrogen Energy* **2020**, *45*, 33687–33730. [CrossRef]

217. Kim, H.; Choi, W.I.; Jang, Y.; Balasubramanian, M.; Lee, W.; Park, G.O.; Park, S.B.; Yoo, J.; Hong, J.S.; Choi, Y.-S.; et al. Exceptional Lithium Storage in a Co(OH)$_2$ Anode: Hydride Formation. *ACS Nano* **2018**, *12*, 2909–2921. [CrossRef] [PubMed]

218. Yartys, V.A.; Lototskyy, M.V.; Akiba, E.; Albert, R.; Antonov, V.E.; Ares, J.R.; Baricco, M.; Bourgeois, N.; Buckley, C.E.; Bellosta von Colbe, J.M.; et al. Magnesium based materials for hydrogen based energy storage: Past, present and future. *Int. J. Hydrogen Energy* **2019**, *44*, 7809–7859. [CrossRef]

219. Zhang, B.; Wu, Y. Recent advances in improving performances of the lightweight complex hydrides Li-Mg-N-H system. *Prog. Nat. Sci.* **2017**, *27*, 21–33. [CrossRef]

220. Zhang, J.; Zhu, Y.; Yao, L.; Xu, C.; Liu, Y.; Li, L. State of the art multi-strategy improvement of Mg-based hydrides for hydrogen storage. *J. Alloys Compd.* **2019**, *782*, 796–823. [CrossRef]

221. El-Eskandarany, M.S. Recent developments in the fabrication, characterization and implementation of MgH$_2$-based solid-hydrogen materials in the Kuwait Institute for Scientific Research. *RSC Adv.* **2019**, *9*, 9907. [CrossRef] [PubMed]

222. Zhang, X.; Liu, Y.; Ren, Z.; Zhang, X.; Hu, J.; Huang, Z.; Lu, Y.; Gao, M.; Pan, H. Realizing 6.7 wt% reversible storage of hydrogen at ambient temperature with non-confined ultrafine magnesium hydride. *Energy Environ. Sci.* **2021**, *14*, 2302–2313. [CrossRef]

223. Wang, N.; Huang, S. Molecular dynamics study on magnesium hydride nanoclusters with machine-learning interatomic potential. *Phys. Rev. B* **2020**, *102*, 094111. [CrossRef]

224. Gigante, A.; Leick, N.; Lipton, A.S.; Tran, B.; Strange, N.A.; Bowden, M.; Martinez, M.B.; Moury, R.; Gennett, T.; Hagemann, H.; et al. Thermal Conversion of Unsolvated Mg(B$_3$H$_8$)$_2$ to BH$_4^-$ in the Presence of MgH$_2$. *ACS Appl. Energy Mater.* **2021**, *4*, 3737–3747. [CrossRef]

225. Crivello, J.-C.; Dam, B.; Denys, R.V.; Dornheim, M.; Grant, D.M.; Huot, J.; Jensen, T.R.; de Jongh, P.; Latroche, M.; Milanese, C.; et al. Review of magnesium hydride-based materials: Development and optimisation. *Appl. Phys. A Mater. Sci. Process.* **2016**, *122*, 97. [CrossRef]

226. Yu, X.; Tang, Z.; Sun, D.; Ouyang, L.; Zhu, M. Recent advances and remaining challenges of nanostructured materials for hydrogen storage applications. *Prog. Mater. Sci.* **2017**, *88*, 1–48. [CrossRef]

227. Duan, C.; Su, Z.; Cao, Y.; Hu, L.; Fu, D.; Ma, J.; Zhang, Y. Synthesis of core-shell α-AlH$_3$@Al(OH)$_3$ nanocomposite with improved low-temperature dehydriding properties by mechanochemical mixing and ionic liquid treatment. *J. Clean. Prod.* **2021**, *283*, 124635. [CrossRef]

228. Zhao, Y.; Mei, Z.; Zhao, F.-Q.; Xu, S.-Y.; Ju, X.-H. Thermal Decomposition Mechanism of 1,3,5,7-Tetranitro-1,3,5,7-tetrazocane Accelerated by Nano-Aluminum Hydride (AlH$_3$): ReaxFF-Lg Molecular Dynamics Simulation. *ACS Omega* **2020**, *5*, 23193–23200. [CrossRef]

229. Jiang, W.; Wang, H.; Zhu, M. AlH$_3$ as a hydrogen storage material: Recent advances, prospects and challenges. *Rare Met.* **2021**, *40*, 3337–3356. [CrossRef]

230. Zhang, X.; Zhang, W.; Zhang, L.; Huang, Z.; Hu, J.; Gao, M.; Pan, H.; Liu, Y. Single-pot solvothermal strategy toward support-free nanostructured LiBH$_4$ featuring 12 wt% reversible hydrogen storage at 400 °C. *Chem. Eng. J.* **2022**, *428*, 132566. [CrossRef]

231. Xian, K.; Nie, B.; Li, Z.; Gao, M.; Li, Z.; Shang, C.; Liu, Y.; Guo, Z.; Pan, H. TiO$_2$ decorated porous carbonaceous network structures offer confinement, catalysis and thermal conductivity for effective hydrogen storage of LiBH$_4$. *Chem. Eng. J.* **2021**, *407*, 127156. [CrossRef]

232. Wang, X.-K.; Zhao, Y.; Zhao, F.-Q.; Xu, S.-Y.; Ju, X.-H. Atomic perspective revealing for combustion evolution of nitromethane/nano-aluminum hydride composite. *J. Mol. Graph. Model.* **2021**, *108*, 107987. [CrossRef]

233. Liu, H.; Zhang, L.; Ma, H.; Lu, C.; Luo, H.; Wang, X.; Huang, X.; Lan, Z.; Guo, J. Aluminum hydride for solid-state hydrogen storage: Structure, synthesis, thermodynamics, kinetics, and regeneration. *J. Energy Chem.* **2021**, *52*, 428–440. [CrossRef]

234. Rahm, J.M.; Löfgren, J.; Erhart, P. Quantitative predictions of thermodynamic hysteresis: Temperature-dependent character of the phase transition in Pd–H. *Acta Mater.* **2022**, *227*, 117697. [CrossRef]

235. Huen, P.; Peru, F.; Charalambopoulou, G.; Steriotis, T.A.; Jensen, T.R.; Ravnsbæk, D.B. Nanoconfined NaAlH$_4$ Conversion Electrodes for Li Batteries. *ACS Omega* **2017**, *2*, 1956–1967. [CrossRef]

236. Dematteis, E.M.; Pistidda, C.; Dornheim, M.; Baricco, M. Exploring Ternary and Quaternary Mixtures in the LiBH$_4$-NaBH$_4$-KBH$_4$-Mg(BH$_4$)$_2$-Ca(BH$_4$)$_2$ System. *ChemPhysChem* **2019**, *20*, 1348–1359. [CrossRef]

237. Zhang, W.; Zhang, X.; Huang, Z.; Li, H.-W.; Gao, M.; Pan, H.; Liu, Y. Recent Development of Lithium Borohydride-Based Materials for Hydrogen Storage. *Adv. Energy Sustain. Res.* **2021**, *2*, 2100073. [CrossRef]

238. Wu, R.; Ren, Z.; Zhang, X.; Lu, Y.; Li, H.; Gao, M.; Pan, H.; Liu, Y. Nanosheet-like Lithium Borohydride Hydrate with 10 wt % Hydrogen Release at 70 °C as a Chemical Hydrogen Storage Candidate. *J. Phys. Chem. Lett.* **2019**, *10*, 1872–1877. [CrossRef] [PubMed]

239. Puszkiel, J.; Gasnier, A.; Amica, G.; Gennari, F. Tuning LiBH$_4$ for Hydrogen Storage: Destabilization, Additive, and Nanoconfinement Approaches. *Molecules* **2020**, *25*, 163. [CrossRef]

240. Bergemann, N.; Pistidda, C.; Uptmoor, M.; Milanese, C.; Santoru, A.; Emmler, T.; Puszkiel, J.; Dornheim, M.; Klassen, T. A new mutually destabilized reactive hydride system: LiBH$_4$–Mg$_2$NiH$_4$. *J. Energy Chem.* **2019**, *34*, 240–254. [CrossRef]

241. Wang, T.; Aguey-Zinsou, K.-F. Controlling the growth of NaBH$_4$ nanoparticles for hydrogen storage. *Int. J. Hydrogen Energy* **2020**, *45*, 2054–2067. [CrossRef]

242. White, J.L.; Strange, N.A.; Sugar, J.D.; Snider, J.L.; Schneemann, A.; Lipton, A.S.; Toney, M.F.; Allendorf, M.D.; Stavila, V. Melting of Magnesium Borohydride under High Hydrogen Pressure: Thermodynamic Stability and Effects of Nanoconfinement. *Chem. Mater.* **2020**, *32*, 5604–5615. [CrossRef]

243. Albanese, E.; Corno, M.; Baricco, M.; Civalleri, B. Simulation of nanosizing effects in the decomposition of Ca(BH$_4$)$_2$ through atomistic thin film models. *Res. Chem. Intermed.* **2021**, *47*, 345–356. [CrossRef]

244. Demirci, U.B. Ammonia borane, a material with exceptional properties for chemical hydrogen storage. *Int. J. Hydrogen Energy* **2017**, *42*, 9978–10013. [CrossRef]

245. Demirci, U.B. Mechanistic insights into the thermal decomposition of ammonia borane, a material studied for chemical hydrogen storage. *Inorg. Chem. Front.* **2021**, *8*, 1900–1930. [CrossRef]

246. Demirci, U.B. Ammonia Borane: An Extensively Studied, Though Not Yet Implemented, Hydrogen Carrier. *Energies* **2020**, *13*, 3071. [CrossRef]

247. Diaz, L.B.; Hanlon, J.M.; Bielewski, M.; Milewska, A.; Gregory, D.H. Ammonia Borane Based Nanocomposites as Solid-State Hydrogen Stores for Portable Power Applications. *Energy Technol.* **2018**, *6*, 583–594. [CrossRef]

248. Liu, S.; Zhang, X.; Jiang, L. 1D Nanoconfined Ordered-Assembly Reaction. *Adv. Mater. Interfaces* **2019**, *6*, 1900104. [CrossRef]

249. Chen, Z.; Kirlikovali, K.O.; Idrees, K.B.; Wasson, M.C.; Farha, O.K. Porous materials for hydrogen storage. *Chem* **2022**, *8*, 693–716. [CrossRef]

250. Ali, N.A.; Sazelee, N.A.; Ismail, M. An overview of reactive hydride composite (RHC) for solid-state hydrogen storage materials. *Int. J. Hydrogen Energy* **2021**, *46*, 31674–31698. [CrossRef]

251. Broom, D.P.; Webb, C.J. Pitfalls in the characterisation of the hydrogen sorption properties of materials. *Int. J. Hydrogen Energy* **2017**, *42*, 29320–29343. [CrossRef]

252. Wang, X.; Song, S.; Zhang, H. A redox interaction-engaged strategy for multicomponent nanomaterials. *Chem. Soc. Rev.* **2020**, *49*, 736–764. [CrossRef]

253. Wu, P.; Tan, S.; Moon, J.; Yan, Z.; Fung, V.; Li, N.; Yang, S.-Z.; Cheng, Y.; Abney, C.W.; Wu, Z.; et al. Harnessing strong metal–support interactions via a reverse route. *Nat. Commun.* **2020**, *11*, 3042. [CrossRef]